Formation, Structure, and Properties of InAs/GaAs Quantum Dots

by

Simon Huang

A dissertation submitted in partial fulfillment
of the requirements for the degree of
Doctor of Philosophy
(Materials Science and Engineering)
in the University of Michigan
2015

Doctoral Committee:

Professor Rachel S. Goldman, Chair
Professor Roy Clarke
Assistant Professor Emmanouil Kioupakis
Professor Jamie D. Phillips

Acknowledgments

First, I would like to thank my thesis advisor, Prof. Rachel S. Goldman, for her guidance and support throughout my studies at the University of Michigan. I would also like to thank my thesis committee members, Prof. Roy Clarke, Prof. Jamie D. Phillips, and Prof. Emmanouil Kioupakis, for their valuable discussions and suggestions.

This dissertation would not have been possible without the help of my collaborators. Especially, I would like to acknowledge Sung Joo Kim in Prof. Xiaoqing Pan's group at University of Michigan, Dr. Andrey Semichaevsky in Prof. Harley T. Johnson's group at University of Illinois, and Dr. Larry Aagesen in Prof. Thornton's group at University of Michigan.

Special thanks go to my fellow group members, past and present. In particular, I would like to thank Myungkoo Kang, Jia-Hung Wu, Michael V. Warren, Sunyeol Jeon, and Davide Del Gaudio for useful discussions, suggestions, and encouragement.

Support from the U.S. Department of Energy through the Center for Solar and Thermal Energy Conversion, an Energy Frontier Research Center, under Award Number DE-SC0000957 is gratefully acknowledged.

Finally, I would like to thank my fiancée Grace Tsai, my parents, my grandparents, my sister, and my friends. I would not have been able to complete my thesis study without their love and support.

Table of Contents

List of Figures

List of Tables

List of Appendices

Abstract

Formation, Structure, and Properties of InAs/GaAs Quantum Dots

By

Simon Huang

Chair: Rachel S. Goldman

Semiconductor quantum dots (QDs) have shown significant promise for a wide range of optoelectronic devices, including solar cells, photodetectors, and lasers. Typically, QDs are fabricated by the misfit-driven Stranski-Krastanov (SK) mode, which results in elliptical-shaped QDs with sizes and densities limited by the lattice misfit. Recently, the nucleation of metal droplets and their conversion to QDs, often termed droplet epitaxy (DE), has attracted much attention because it allows QD fabrication without lattice misfit. However, the mechanisms for the conversion of In islands to InAs QDs and the origins of misfit dislocation (MD) displacement are still unclear. Thus, further examination on the formation mechanism and microstructures of DE QDs is essential. Here, we report on the structure and properties of InAs/GaAs QDs formed by DE and SK approaches. These results suggest that DE is promising for tuning QD sizes and densities, as well as tailoring carrier confinement in the vicinity of QDs.

Using a finite-element Schrödinger-Poisson model that considers experimentally measured QD and wetting layer (WL) shapes, sizes, and spacings, we examined the

influence of InAs/GaAs SK QDs on the solar cell external quantum efficiency (EQE). A comparison between the computed and measured EQEs reveals a broadening of sub-bandgap EQE induced by QD size distribution, and a weak EQE contribution from the WLs.

To further enhance the control of QD size, density, and microstructure, we investigate alternative QD fabrication approaches via annealing In islands under an As flux. We revealed the influence of As surface coverage on the QD formation mechanisms. On c(4x4) GaAs surfaces, QD formation follows DE. For the As capped surfaces, QDs nucleate by solid phase epitaxy during annealing of an amorphous film. Furthermore, we revealed the origin of interlayer formation and MD displacement in the vicinity of InAs/GaAs QDs. For SK QDs, MDs nucleate at the QD/buffer interface. For DE QDs with low In exposure, an InGaAs interlayer at the QD/buffer interface results in MD vertical displacement. For DE QDs with high In exposure, the formation of an InAs interlayer at the island/buffer interface leads to MDs at the QD/buffer interface.

Chapter 1

Introduction

1.1 Overview

Recently, nanometer-sized molecular clusters, or nanostructures, have been proposed for a wide variety of solid state devices, including solar cells,[1,2] lasers,[3] and light emitting diodes (LEDs).[4,5] An example is a semiconductor quantum dot (QD), or “artificial atom”, which is a cluster of atoms that spans only one-billionth of a meter. With charge carriers confined in all three dimensions, the energy levels of QDs can be altered by varying QD size and composition, allowing tunable operation wavelength for QD-based devices. In particular, a wide range of emission wavelengths have been demonstrated for both QD lasers and LEDs.[4,5,6] Due to their ability to provide additional absorption bands, semiconductor QDs have also been proposed for use in the next generation high efficiency solar cells.[7] By absorbing a greater portion of the solar spectrum, QD solar cells have been predicted to have a maximum efficiency that greatly exceeds the efficiency of a typical homeowner’s solar panels.

To date, the fabrication of epitaxial QDs typically involves the misfit-driven Stranski-Krastanov (SK) growth,[8] in which case the QD size, density, and shape are limited by the lattice misfit. For the past few years, there has been significant interest in an alternative QD fabrication approach, termed droplet epitaxy (DE),[9] which is driven by surface tension rather than by lattice misfit. For DE, metal droplets are first deposited on a substrate surface, followed by exposure to a vapor to convert the metal droplets to semiconductor QDs. The multi-step DE growth enables more flexibility for tuning QD sizes, densities, and materials combinations.[10,11,12,13]

For highly lattice-mismatched thin film systems, strain relaxation typically occurs by a combination of elastic relaxation via island formation and plastic relaxation via misfit dislocation (MD) nucleation.[14,15] For semiconductor devices based on lattice-mismatched materials, high densities of dislocations are often observed, which can significantly reduce carrier lifetimes and, thus, degrade the device performance. The presence of interfacial MDs allows effective strain relieving at the interface of epitaxial layers, resulting in significantly reduced dislocation density within the device structures.[16,17] In addition, vertical displacement of interfacial MDs is promising for tailoring carrier confinement in the vicinity of QDs, enabling the fabrication of electronically ultra-small QDs.

This chapter opens with the motivation for studies of semiconductor QDs for various optoelectronic device applications. Next, we review the epitaxial growth methods for fabricating semiconductor QDs. We then discuss the microstructure and dislocations in the vicinity of QDs. Finally, the chapter concludes with objectives and outline of the dissertation.

1.2 Device Applications of Semiconductor Quantum Dots

Semiconductor quantum dots (QDs) are nanostructures with charge carrier confinement in three dimensions. In the past few years, semiconductor QDs have attracted considerable scientific attention and have been utilized for a wide range of optoelectronic applications, including solar cells,[1,2] lasers,[3] photodetectors,[18] and light emitting diodes.[4,5] In particular, semiconductor QDs have been proposed for achieving the next generation high efficiency solar cells. In the late 1990s, Antonio Luque and Antonio Marti proposed the concept of the intermediate band solar cell (IBSC),[7] which has been considered a promising technology to overcome the Shockley-Quiesser single-junction solar cell theoretical efficiency limit of 30%.[19] Similar to multi-junction solar cells, which have attained efficiencies well above 40% in the past several years, IBSCs are designed to minimize intrinsic losses due to thermalization and transparency by absorbing a broader spectrum of solar radiation. In principle, this is achieved by absorbing photons with sub-bandgap energies, which excite charge carriers from the valence band (VB) to partially filled intermediate band (IB), and then up to the conduction band (CB), followed by extraction of the photocurrent from the CB.

Several groups have proposed embedding QDs in the intrinsic region of a standard *p-i-n* solar cell as a means to introduce the IBs needed for the IBSC concept, as illustrated in Figure 1.1.[20,21,22] Although many efforts have been aimed at optimizing the IBSC band structure to achieve the maximum possible photocurrent density under solar illumination, device efficiencies have been consistently lower than theoretical predictions. To date, typical QD-based devices have involved the use of a misfit-driven

Stranski-Krastanov approach for QD fabrication, which results in elliptical-shaped QDs with lateral dimensions > 20 nm, and densities limited to ~10^{10} cm^{-2}. These undesirable QD characteristics, such as large and non-uniform QD sizes and anisotropic QD shapes, lead to additional energy levels between the IB and CB that facilitate the carrier thermal escapes. Figure 1.2 shows an example of an elliptically-shaped QD, where the QD diameter is much larger than the height, leading to multiple energy levels in the CB offset. As a result, the effective bandgap is reduced, which lowers the open-circuit voltages (V_{OC}). In essence, QD-induced photo-current enhancements are typically negated by reduced device V_{OC}.

To maximize photon absorption and ensure the preservation of device V_{OC}, an ultra-high QD density (> 10^{12} cm^{-2}) with ultra- small size (< 10 nm), and spherical shape is desired.[23,24] Therefore, one of the main goals of this thesis study is to explore various QD fabrication approaches to enhance the control over the size, density, shape, and microstructure of the QDs, towards achieving high efficiency optoelectronic devices, such as solar cells, lasers, and LEDs.

1.3 Fabrication of Semiconductor Quantum Dots

Several approaches have been explored for the fabrication of semiconductor QDs, including chemical synthesis, [25] pre-growth lithographic patterning, [26] ion-beam synthesis,[27,28] and self-assembled epitaxial growth.[29,30] In this section, we review the self-assembled Stranski-Krastanov and droplet epitaxy approaches used in this thesis study and their ability to control QD size, density, shape, and microstructure.

1.3.1 Stranski-Krastanov Approach

One of the most commonly used QD growth methods is the misfit-driven Stranski-Krastanov (SK) growth mode.[8] Although this mechanism was proposed by Ivan Stranski and Lyubomir Krastanov in 1938, it was not until 1985 that the formation of self-assembled semiconductor QDs based on strained heterostructures was experimentally observed in the InAs/GaAs system.[29] The SK growth generally initiates with deposition of thin film on a lattice-mismatched substrate, leading to the formation of strained monolayers. The pseudomorphic layer-by-layer growth continues until the film reaches a critical thickness, h_C, which is inversely proportional to the misfit strain between the film and the substrate.[31,32] Here, the lattice misfit is defined as follows: $f = (a_f - a_s)/a_s$, where a_f and a_s is the lattice constant of the film and the substrate, respectively. Above h_C, 3D islands form to elastically relax the film/substrate misfit strain, as shown in Figure 1.3(a). Although SK growth mode is convenient and commonly used for the fabrication of semiconductor QDs, the size and density of the SK-grown QDs are limited by the misfit between the film and the substrate, as mentioned in Section 1.2. In addition, the SK QDs typically have an elliptical shape, leading to a reduced open-circuit voltage for QD-based solar cells.[33]

1.3.2 Droplet Epitaxy Approach

Semiconductor QDs can also be grown epitaxially by an alternative approach termed “droplet epitaxy (DE)”. Proposed by Nobuyuki Koguchi in 1991,[9] the DE technique typically involves deposition of metal droplets or islands on a substrate surface, followed by annealing under a group V flux to convert the metal droplets/islands to semiconductor QDs, as shown in Figure 1.3(b). For DE, the QD size and density are not limited by the misfit strain since the formation of metal droplets is driven by surface tension rather than misfit strain. By varying the substrate temperature and growth rate, a broad range of QD densities (~1×10^{8} to 5×10^{10} cm^{-2}) have been achieved via DE.[34] In addition, without the requirement of lattice mismatch, DE enables QD growth even in lattice-matched systems, such as GaAs/AlGaAs and GaAs/GaAs.[12,13] On the other hand, the multi-step process of DE growth allows the fabrication of a wide range of nanostructures. By varying the As flux used for annealing the metal droplets, quantum rings or even concentric double-ring structures are achievable via DE.[35,36] Recently, Somaschini *et al*. have demonstrated GaAs nanostructures with tunable aspect ratios on Si (ranging from low aspect ratio QDs to high aspect ratio nanowires), where the GaAs QDs formed by DE are used as seeds for NW growth.[37] The high tunability of QD density and size by DE is exploited to tailor the NW density and size without using metal catalysts, which opens up opportunities for integrating III-V semiconductors on Si.

1.4 Misfit Dislocation and Interlayer Formation in the Vicinity of Quantum Dots

In addition to QD size, density, and shape, the microstructure of QDs also has a significant influence on the electronic states and transport properties of QD-based devices. For lattice-mismatched materials systems, strain relaxation often occurs by a combination of QD formation (elastic relaxation) and MD nucleation (plastic relaxation).[14,15] Therefore, the presence of MDs is commonly observed in the vicinity of QDs, typically at the interface between the QD and the substrate.[38,39,40] Recently, vertical MD displacement has been reported in various material systems, such as GaSb/GaAs QDs and InAs/GaAs QDs.[41,42] To date, the origin of the vertical MD displacement has been attributed to the formation of an intermediate layer and an oxidation-induced downward shift of the crystalline substrate surface. However, in many cases, interfacial MDs have been observed following air exposure.[38,39,40] Therefore, further investigation is necessary to identity the origins of vertical MD displacement and the interlayer formation in the vicinity of QDs. In addition, controlling the vertical displacement of interfacial MDs is promising for tailoring carrier confinement in the vicinity of QDs. In particular, the upward displacement of MDs is likely to reduce the QD size electronically, enabling the fabrication of ultra-small QDs in highly lattice-mismatched systems.

1.5 Dissertation Objectives

The first part of this thesis focuses on the photovoltaic properties of solar cells based on InAs/GaAs QDs formed by the conventional SK growth mode. The influence of wetting layers (WLs) and size distribution of the SK QDs on the sub-bandgap external quantum efficiency (EQE) of InAs/GaAs QD solar cells is examined. We compute the device EQE considering realistic QD and WL shapes, sizes, and spacings measured by scanning tunneling microscopy (STM) and atomic force microscopy (AFM). We compare the computed EQE to the measured EQE of QD solar cells and discuss the key contributions of QD size variations and WLs to the sub-bandgap EQE. This work reveals the significant influence of QD size on the electronic structure and photovoltaic properties of QD-based devices, which motivates further investigation of alternative QD fabrication approaches to enhance the control of QD size, density, and microstructure.

The second part of this thesis focuses on the investigation of the formation mechanism of InAs QDs via annealing In islands under an As flux. The influence of As surface coverage on the formation mechanism of InAs QDs is examined. With various GaAs buffer surface reconstructions, we report two distinct QD formation mechanisms: DE and solid phase epitaxy (SPE). We also discuss the conversion of In islands to InAs QDs in terms of In surface diffusion length and InAs/GaAs interface energy.

The third part of this thesis is devoted to the formation of interlayer and displacement of MDs in the vicinity of InAs QDs. The origins of vertical MD displacement and InGaAs interlayer formation in the vicinity of InAs/GaAs QDs are examined. We investigate the microstructures and composition of both SK and DE QDs using high resolution transmission electron microscopy (HRTEM) and X-ray energy dispersive spectroscopy (XEDS). We propose a QD formation mechanism which describes the key roles of nano-drilling and intermixing effects in MD displacement and interlayer formation during DE of InAs/GaAs QDs.

1.6 Outline of the Dissertation

This dissertation is organized as follows. Chapter 2 describes the experimental procedures used for this thesis work, including molecular beam epitaxy, reflection high-energy electron diffraction, atomic force microscopy, transmission electron microscopy, X-ray Energy dispersive spectroscopy, and external quantum efficiency measurement.

In Chapter 3, we present the influence of QD size variation and WLs on the InAs/GaAs QD solar cell EQE. We compute the sub-bandgap EQEs using a finite-element Schrödinger-Poisson model. A comparison between the computed and measured EQEs reveals a broadening of sub-bandgap EQE induced by QD size vertical distribution and a weak EQE contribution from the WLs. The unique combination of experiment and computation may be used as a guide for designing QD SLs for various optoelectronic device applications.

In Chapter 4, we present the formation mechanisms of In islands and their conversion to InAs QDs via annealing under As flux. The QD formation mechanism is attributed to either DE or SPE, depending on buffer surface As coverage. On c(4x4) GaAs surfaces, QD formation follows DE, in which case one-to-one conversion from In islands to InAs QDs occurs on c(4x4)α surfaces. For c(4x4)β surfaces, enhanced In surface diffusion leads to lower densities of larger QDs. For the As capped surfaces, QDs nucleate by SPE during As annealing of an amorphous film. These mechanisms are likely to be applicable to the formation of a wide variety of compound semiconductor nanostructures.

In Chapter 5, we present our investigations of the influence of growth mode on MD displacement and interlayer formation in the vicinity of InAs/GaAs QDs. For the SK growth mode, arrays of regularly-spaced MDs nucleate at the interface between the InAs QD and the GaAs layer. For the DE growth mode, both In island formation and In-induced "nano-drilling" of the GaAs buffer layer are observed during In deposition. For low In exposure, the In islands are converted to InAs QDs upon annealing under As flux, with an InGaAs interlayer at the QD/buffer interface. Meanwhile, MDs nucleate at the QD/interlayer interface. For high In exposure, an InAs interlayer forms at the island/buffer interface during the In deposition step. Annealing in an As flux leads to the conversion of In islands to InAs QDs, resulting in MDs at the QD/buffer interface. The DE approach enables the control of MD vertical displacement during QD formation, which is promising for tailoring carrier confinement in the vicinity of QDs. Finally, in Chapter 6, we present a summary and an outline for future work.

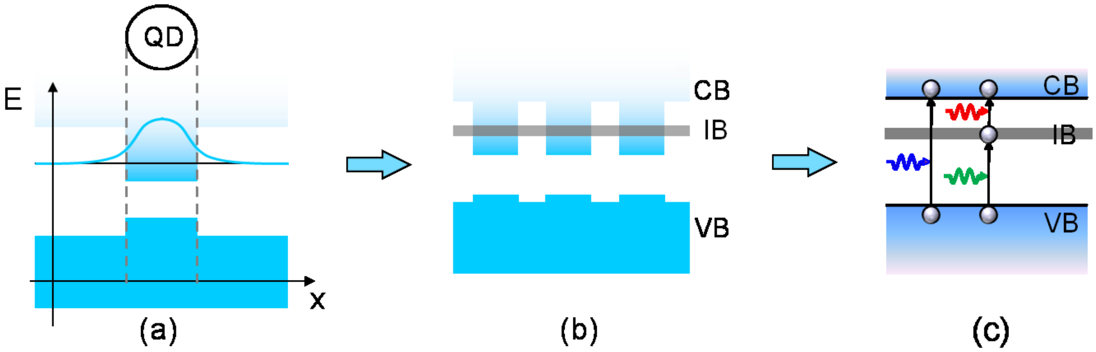

Figure 1.1 Schematic diagram showing (a) a discrete energy state from a QD, (b) formation of an intermediate band (IB) from a QD array, and (c) the band structure of an IB semiconductor absorbing sub-bandgap energy photons.

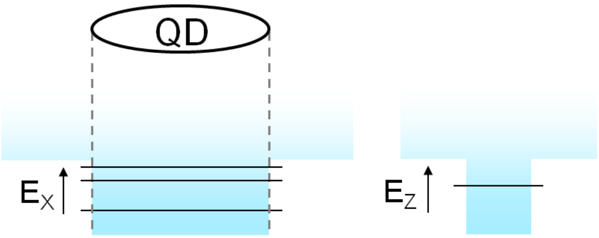

Figure 1.2 Schematic illustration showing additional energy levels in the conduction band offset induced by QD shape anisotropy.

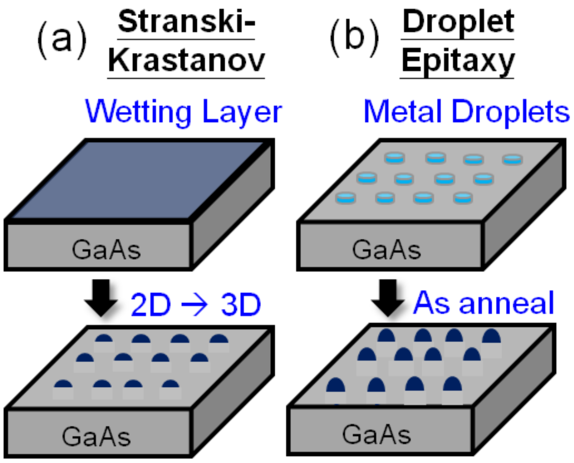

Figure 1.3 Schematic of QD growth via the (a) Stranski-Krastanov growth mode where 3D islands form as the wetting layer reaches the critical thickness; (b) droplet epitaxy growth mode where metal droplets are crystallized into semiconductor QDs via exposure to an arsenic flux.

1.7 Reference

---

[1] A. Marti, L. Cuadra, and A. Luque, in *Conference Record of the Twenty-Eighth Ieee Photovoltaic Specialists Conference - 2000* (IEEE, New York, 2000), pp. 940-943.

[2] A. Marti, E. Antolin, C. R. Stanley, C. D. Farmer, N. Lopez, P. Diaz, E. Canovas, P. G. Linares, and A. Luque, Phys. Rev. Lett. **97**, 247701 (2006).

[3] D. L. Huffaker, G. Park, Z. Zou, O. B. Shchekin, and D. G. Deppe, Appl. Phys. Lett. **73**, 2564 (1998).

[4] N. M. Park, T. S. Kim, and S. J. Park, Appl. Phys. Lett. **78**, 2575 (2001).

[5] J. X. Chen, A. Markus, A. Fiore, U. Oesterle, R. P. Stanley, J. F. Carlin, R. Houdre, M. Ilegems, L. Lazzarini, L. Nasi, M. T. Todaro, E. Piscopiello, R. Cingolani, M. Catalano, J. Katcki, and J. Ratajczak, J. Appl. Phys. **91**, 6710 (2002).

[6] J. P. Reithmaier and A. Forchel, Comptes Rendus Physique **4**, 611 (2003).

[7] A. Luque and A. Martí, Phys. Rev. Lett. **78**, 5014 (1997).

[8] I. N. Stranski and L. Krastanow, Akademie der Wissenschaften Wien **146** 797 (1938).

[9] N. Koguchi, S. Takahashi, and T. Chikyow, J. Cryst. Growth **111**, 688 (1991).

[10] J. S. Kim and N. Koguchi, Appl. Phys. Lett. **85**, 5893 (2004).

[11] E. Cohen, S. Yochelis, O. Westreich, S. Shusterman, D. P. Kumah, R. Clarke, Y. Yacoby, and Y. Paltiel, Appl. Phys. Lett. **98**, 243115 (2011).

[12] N. Koguchi and K. Ishige, Jpn. J. Appl. Phys., Part 1 **32**, 2052 (1993).

[13] K. Watanabe, N. Koguchi, and Y. Gotoh, Jpn. J. Appl. Phys., Part 2 **39**, L79 (2000).

[14] F. K. LeGoues, M. C. Reuter, J. Tersoff, M. Hammar, and R. M. Tromp, Phys. Rev. Lett. **73**, 300 (1994).

---

[15] K. Tillmann, D. Gerthsen, P. Pfundstein, A. F€orster, and K. Urban, J. Appl. Phys. **78**, 3824 (1995).

[16] S. H. Huang, G. Balakrishnan, A. Khoshakhlagh, A. Jallipalli, L. R. Dawson, and D. L. Huffaker, Appl. Phys. Lett. **88**, 131911 (2006).

[17] A. Jallipalli, G. Balakrishnan, S. H. Huang, T. J. Rotter, K. Nunna, B. L. Liang, L. R. Dawson and D. L. Huffaker, Nanoscale Res. Lett. **4**, 1458 (2009).

[18] J. Phillips, K. Kamath, and P. Bhattacharya, Appl. Phys. Lett. 72, 2020 (1998).

[19] W. Shockley and H. J. Queisser, J. Appl. Phys. **32**, 510 (1961).

[20] R. P. Raffaelle, S. L. Castro, A. F. Hepp, and S. G. Bailey, Progress in Photovoltaics: Research and Applications **10**, 433 (2002).

[21] M. A. Green, Materials Science and Engineering: B **74**, 118 (2000).

[22] A. Marti, L. Cuadra, and A. Luque, Electron Devices, IEEE Transactions on **48**, 2394 (2001).

[23] A. Luque, A. Martí, E. Antolín, and C. Tablero, Physica B: Condensed Matter **382**, 320 (2006).

[24] Alexander Mellor, Antonio Luque, Ignacio Tobías, and Antonio Martí, Appl. Phys. Lett. **101**, 133909 (2012).

[25] M. L. Steigerwald, A. P. Alivisators, J. M. Gibson, T. D. Harris, R. Kortan, A. J. Muller, A. M. Thayer, T. M. Duncan, D. C. Douglass, and L. E. Brus, J. Am. Chem. Soc. **110**, 3046 (1988).

[26] S. Birudavolu, N. Nuntawong, G. Balakrishnan, Y. C. Xin, S. Huang, S. C. Lee, S. R. J. Brueck, C. P. Hains, and D. L. Huffaker, Appl. Phys. Lett. **85**, 2337 (2004).

---

[27] X. Weng, S. J. Clarke, W. Ye, S. Kumar, A. Daniel, R. Clake, J. Holt, J. Sipowska, A. Francis, V. Rotberg, and R. S. Goldman, J. Appl. Phys. **92**, 4012 (2002).

[28] A. W. Wood, X. Weng, Y. Q. Wang, and R. S. Goldman, Appl. Phys. Lett. **99**, 093108 (2011).

[29] L. Goldstein, F. Glas, J. Y. Marzin, M. N. Charasse, and G. Le Roux, Appl. Phys. Lett. **47**, 1099 (1985).

[30] N. Koguchi, S. Takahashi, and T. Chikyow, J. Cryst. Growth **111**, 688 (1991).

[31] Y. Tu and J. Tersoff, Phys. Rev. Lett. **93**, 216101 (2004).

[32] H. R. Eisenberg and D. Kandel, Phys. Rev. Lett. **85**, 1286 (2000).

[33] Alexander Mellor, Antonio Luque, Ignacio Tobías, and Antonio Martí, Appl. Phys. Lett. **101**, 133909 (2012).

[34] C. Heyn, A. Stemmann, A. Schramm, H. Welsch, W. Hansen, and A. Nemcsics, Phys. Rev. B **76**, 075317 (2007).

[35] T. Mano and N. Koguchi, J. Cryst. Growth **278**, 108 (2005).

[36] T. Mano, T. Kuroda, S. Sanguinetti, T. Ochiai, T. Tateno, J. Kim, T. Noda, M. Kawabe, K. Sakoda, G. Kido, and N. Koguchi, Nano Lett. **5**, 425 (2005).

[37] C. Somaschini, S. Bietti, A. Trampert, U. Jahn, C. Hauswald, H. Riechert, S. Sanguinetti, and L. Geelhaar, Nano Lett. **13**, 3607 (2013).

[38] A. Trampert, E. Tournie, and K. H. Ploog, Appl. Phys. Lett. **66**, 2265 (1995).

[39] Y. Chen, X. W. Lin, Z. Liliental-Weber, J. Washburn, J. F. Klem, and J. Y. Tsao, Appl. Phys. Lett. **68**, 111 (1996).

[40] K. Tillmann and A. Forster, Thin Solid Films **368**, 93–104 (2000).

---

[41] Y. H. Kim, J. Y. Lee, Y. G. Noh, M. D. Kim, and J. E. Oh, Appl. Phys. Lett. **90**, 241915 (2007).

[42] Z. B. Chen, W. Lei, B. Chen, Y. B. Wang, X. Z. Liao, H. Tan, J. Zou, S. Ringer, and C. Jagadish, Nanoscale Res. Lett. **7**, 486 (2012).

Chapter 2

Experimental Procedures

2.1 Overview

This chapter describes the experimental procedures used to synthesize and characterize the nanostructures studied in this dissertation work. All QDs and films were grown on semi-insulating GaAs (001) substrates by molecular-beam epitaxy (MBE). During MBE growth, the surface reconstruction was monitored by reflection high-energy electron diffraction (RHEED). Following growth, surface morphologies were examined using atomic force microscopy (AFM). The microstructure and composition of QDs were investigated using high resolution transmission electron microscopy (HRTEM), scanning TEM (STEM), and X-ray energy dispersive spectroscopy (XEDS) with the assistance of Sung Joo Kim in Pan group. To study the influence of QDs on the photovoltaic properties of *p-i-n* heterostructures, solar cell device fabrication and external quantum efficiency measurements were carried out with the assistance of Leon Webster, Kuen-Ting Shiu, and Kyusang Lee.

2.2 Molecular Beam Epitaxy

The QD samples discussed in the bulk of this dissertation were grown in a Modified Varian Gen II MBE system. Additional preliminary experiments, discussed in Chapter 6, were performed in a Riber Compact 21 MBE system. Molecular beam epitaxy (MBE) is a vacuum evaporation technique for epitaxial growth of high quality films one atomic layer at a time.[1,2] The process is performed in an ultra-high vacuum chamber, where an epitaxial film is formed via chemical interaction of molecular beams on a heated crystalline substrate surface.[3] The molecular beams are produced by sublimation or evaporation of heated solids or liquids, and the incoming molecules are so reactive that epitaxial growth can occur at conditions far from equilibrium.

The Modified Varian Gen II MBE system, as illustrated in Figure 2.1, consists of separately pumped load-lock, buffer, and growth chambers connected by magnetic transfer rods and trolleys. The growth chamber source flange houses seven solid sources (Ga, In, Al, Si, Be, Bi, and As cracker), and the source materials are contained in pyrolytic boron nitride (PBN) crucibles located in Knudsen effusion cells. The molecular beam flux is exponentially dependent on the temperature of the effusion cell controlled by heating the filaments surrounding the PBN crucible. The effusion cell temperature is monitored by a thermocouple in contact with the crucible, and the beam flux is measured by an ionization gauge sitting at the growth position. The exposure of each molecular beam is controlled by computer controlled pneumatic shutters. The flux of the As source is controlled by a needle valve, adjustable between 0 to 300 mil, sitting in front of the As bulk zone. The As cracking zone temperature determines the As species (As_2 or As_4)

produced by the cracker. Details regarding the determination of As species is described in Appendix C. Samples are held in the growth chamber at either growth or transfer position by a manipulator referred to as the CAR (Continuous Azimuthal Rotation). During epitaxial growth, the CAR is typically rotated at 10 rpm to ensure the film uniformity. In addition, the growth chamber contains facilities for *in-situ* reflection high-energy electron diffraction (RHEED), which will be described in Section 2.3. The growth chamber is pumped by a CTI Cryo-Torr 8 cryopump and a Varian sputter-ion pump, and the growth chamber pressure is monitored by an ionization gauge located on the chamber wall. During growth, the growth chamber is cooled down with liquid nitrogen (LN2), which helps achieve a base pressure of $< 3\times10^{-10}$ Torr.

All samples were grown on "epi-ready" GaAs substrates, which were delivered in a dry N_2 sealed container, ready for immediate loading into the load-lock chamber. All substrates were mounted on heated molybdenum blocks using indium, baked in the load-lock chamber for 8 hours at 150 ºC, and then outgassed in the buffer chamber for at least 30 minutes at 180 ºC. Subsequently, the substrate was transferred into the growth chamber with the transfer rod. As the substrate temperature was raised to 300 ºC in the growth chamber, the needle valve and shutter for As source were opened, providing an As overpressure to prevent GaAs decomposition. The substrate temperature was then increased to the point where a streaky RHEED pattern is observed, indicating that the surface oxide has been desorbed. Desorption of oxide on a GaAs surface typically occurs at 580 to 610 ºC.[4,5] However, the temperature measured from the backside of the molybdenum block can be considerably different from the temperature at the substrate surface. The thermocouple usually measures ~ 750 to 830 °C for GaAs oxide desorption.

Therefore, the oxide desorption temperature was used as an internal block calibration for each growth. Finally, the substrate temperature was raised for an additional 30 °C for 10 minutes to ensure complete desorption of surface oxide.

2.3 Reflection High-Energy Electron Diffraction

The growth rates and surface reconstructions during growth was monitored *in-situ* with a STAIB RH 30 RHEED source, operating at 18 keV. The electron beam from the RHEED gun is accelerated and directed onto the sample surface at a grazing angle of ~1º. The electrons that are diffracted by the sample surface then impinge on a phosphor screen on the other side of the growth chamber, as shown in Figure 2.1. A charge coupled device (CCD) camera is used to collect the luminescence from the phosphor screen. As the epitaxial film grows, the intensity of the RHEED streaks oscillates. The growth rate of the film is extracted from the frequency of the RHEED oscillations, assuming that one oscillation corresponds to one complete monolayer growth.[6,7,8] In addition, the RHEED pattern was used to monitor the surface reconstruction during the epitaxial growth. The standard notation, (M×N), is used to report the reconstructions, where (×M) is the reconstruction along [110], while (×N) is the reconstruction along $[1\bar{1}0]$.

2.4 Atomic Force Microscopy

The surface morphology of the InAs QDs was investigated using tapping mode atomic force microscopy (AFM) with Veeco Dimension Icon AFM in the Electron

Microbeam Analysis Laboratory (EMAL) at the University of Michigan. We used etched silicon Nanoscience AFM probes with tip radius < 10 nm, length = 125 μm, resonance frequency = 300 kHz, and spring constant = 40 N/m for imaging. The AFM scanning head consists of a piezoelectric tube scanner with the x-, y-, and z- electrodes oriented as shown in Figure 2.2. The z-motion is achieved by expanding or contracting the piezoelectric tube with an applied voltage to the z-electrode. Similarly, the x- and y-motion of the AFM tip is achieved by applying a voltage to the x- and y- electrodes to enable the bending of the piezoelectric tube in the x- and y- directions, respectively. Figure 2.3 shows a schematic of (a) straight and (b) bended piezoelectric tube during AFM tip scanning on a flat surface. The bending of the piezoelectric tube results in an offset of the laser reflection on the photodiode, as shown in Figure 2.3. The offset of the laser reflection usually leads to a curvature distortion in the output morphology (a.k.a. "bowing") from the scanning surface, which is more significant for larger area scanning.[9] To correct the bowing in the AFM images, all as-collected AFM images were flattened by subtracting a quadratic background in the lateral directions using Scanning Probe Image Processor (SPIP).

2.5 Transmission Electron Microscopy/X-ray Energy Dispersive Spectroscopy

To study the microstructures and compositional profiles of the In islands and InAs QDs, we used high resolution transmission electron microscopy (HRTEM), scanning TEM (STEM), and X-ray energy dispersive spectroscopy (XEDS) facilities in the

Electron Microbeam Analysis Laboratory (EMAL) at the University of Michigan. The TEM measurements were performed by Mr. Sung Joo Kim in Prof. X.Q. Pan's group at University of Michigan.

Cross-sectional TEM specimens were prepared using conventional mechanical polishing, followed by argon ion milling at 77 K. HRTEM imaging was carried out in a JEOL JEM3100F operating at 300 kV. To obtain HRTEM images, the sample was tilted such that the incident beam was aligned along the <110> zone axis, and the images were captured via a CCD camera with Gatan Digital Micrograph.

The chemical composition of the InAs QDs formed by DE was examined by X-Ray Energy Dispersive Spectroscopy (XEDS), in a spherical aberration-corrected JEOL JEM2100F operating at 200 kV. As electrons irradiate on the sample, inner-shell electrons from the sample may be ejected by the incident electrons, which may lead to subsequent relaxation of an outer-shell electron to a lower-energy state. Then, a characteristic X-ray emission from the sample can be detected, which corresponds to the energy difference between the energy states. Therefore, the emitted X-ray directly corresponds to the atomic structure of the excited atom, and the X-ray intensity is proportional to the concentration of the specific element within the sample.

To determine the chemical composition in the vicinity of the QD, XEDS data was collected for In, Ga, and As at several locations along the growth direction. The atomic percentages of each element can be related to the measured intensities from XEDS by the Cliff-Lorimer equation.[10] The Cliff-Lorimer factor can be calculated using the XEDS collected within the GaAs buffer layer. Then, the atomic percentage of each element can be calculated from the ratio of the measured intensities.[10]

2.6 I-V and External Quantum Efficiency Measurements

To study the photovoltaic properties of the *p-i-n* heterostructures containing QD superlattices, samples were processed using standard photolithography into 2×2 mm^2 cells with n-type front contact of Ge/Ni/Au and p-type back contact of Au/Zn deposited using e-beam evaporation. The front contact shadowing was ~6% of the surface area. The solar cell fabrications were performed by Dr. Leon Webster in the Lurie Nanofabrication Laboratory (LNF) at University of Michigan.

The current-voltage (I-V) characteristic of the QD and control cells were measured under Air Mass 1.5 Global (AM 1.5G) illumination of 0-1 sun intensity (0-100 mW/cm^2) using a Xenon lamp calibrated with a National Institute of Standards and Technology (NIST) traceable silicon photodetector. In particular, the illumination from the Xenon lamp was filtered by an AM 1.5G filter and directed to the sample through a collimator, as shown in Figure 2.4. The I-V characteristic was then measured at room temperature using a parameter analyzer. The measured I-V characteristic of the QD and control cells is presented in Appendix D. The external quantum efficiency (EQE) of a solar cell is defined as the ratio of the number of collected charge carriers to the number of incident photons. The EQE of our solar cells were measured as a function of incident light wavelength (λ) with a setup consisting of a halogen lamp, a light chopper, a monochromator, an optical fiber, and a lock-in amplifier, as shown in Figure 2.5. Specifically, low-intensity illumination ($<<100$ mW/cm^2) from the halogen lamp was modulated by the chopper, spectrally-filtered with the monochromator, and guided via the optical fiber to the sample. The photocurrent was then measured at room temperature using the lock-in amplifier referenced to the chopper frequency. The measured EQEs and the influence of QDs size distributions are discussed in Chapter 3. The I-V and EQE measurements were performed by Mr. Kyusang Lee and Dr. K.T. Shiu in Prof. S. R. Forrest's laboratory at University of Michigan.

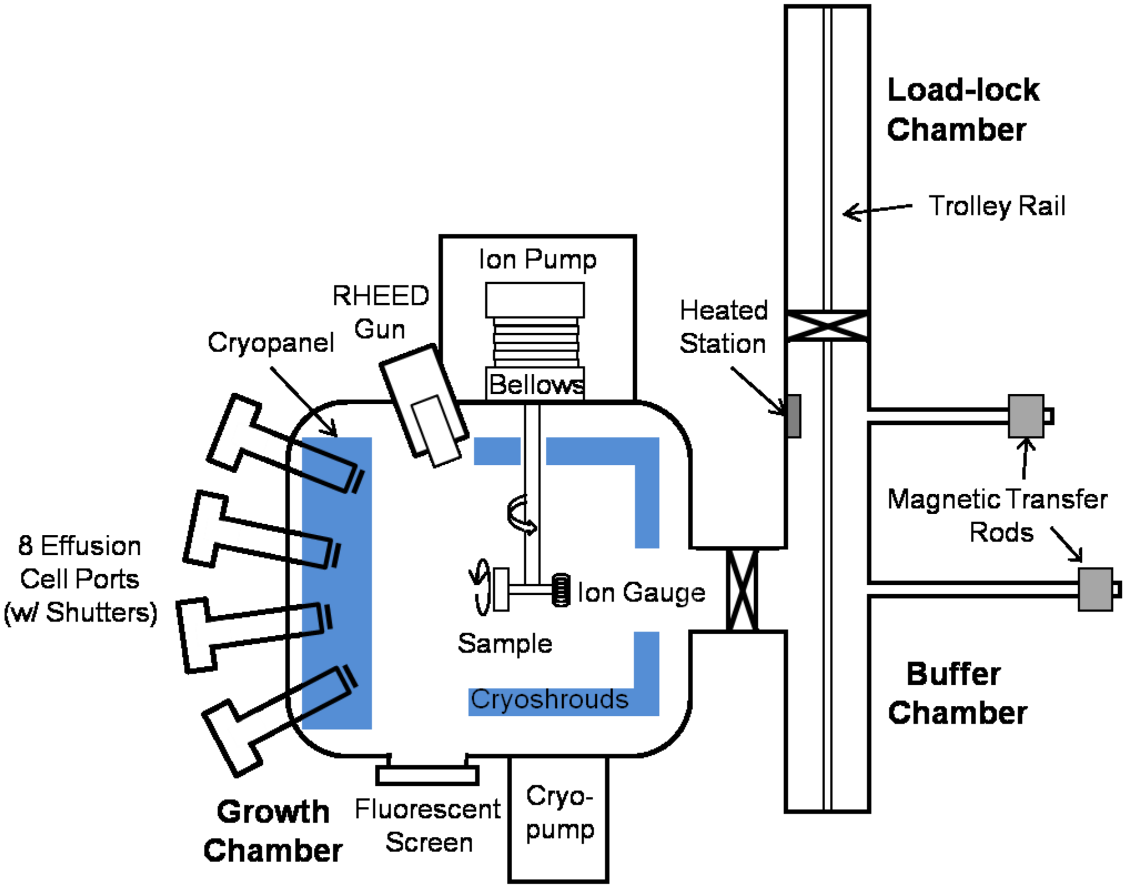

Figure 2.1 Schematic (top-down view) of the Modified Varian Gen II molecular beam epitaxy system used in this thesis study. Ga, Al, In, Si, Be, Bi, and As solid sources are located in the effusion cell ports.

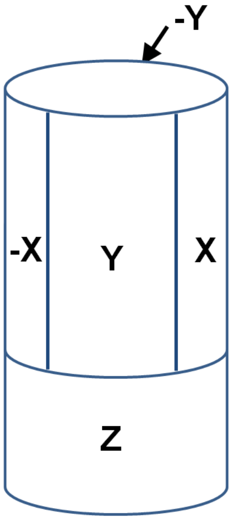

Figure 2.2 Schematic of AFM piezoelectric tube scanner.

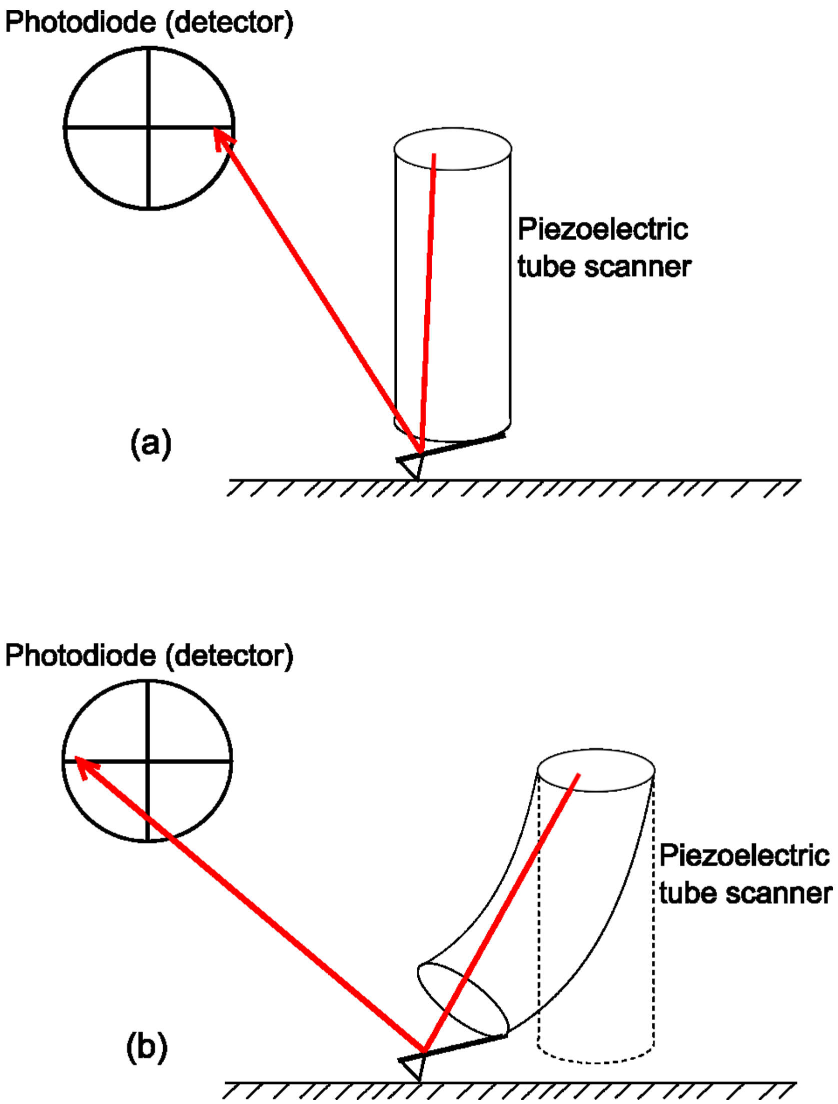

Figure 2.3 Schematic of (a) straight and (b) bended piezoelectric tube during AFM tip scanning on a flat surface. The laser reflection from the tip to the photodiode is indicated by the red line with an arrow.

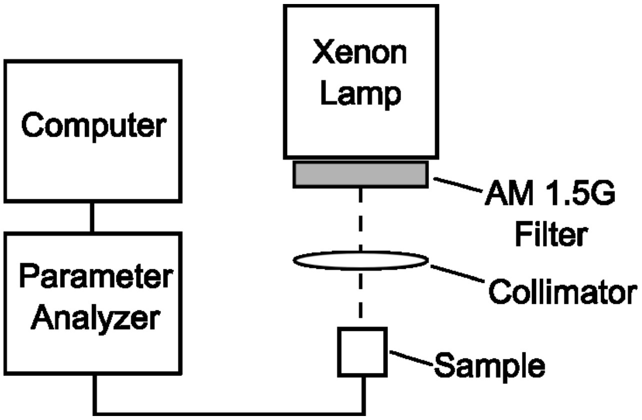

Figure 2.4 Schematic of the I-V measurement setup.

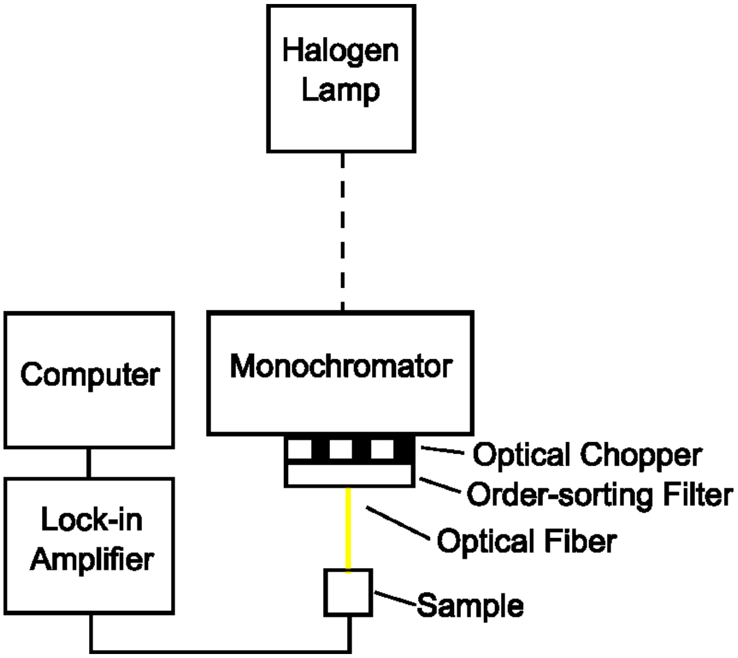

Figure 2.5 Schematic of the EQE measurement setup.

2.7 References

---

[1] A.Y. Cho and J.R. Arthur, Progr. Solid State Ch. **10**, 157 (1975).

[2] A.Y. Cho, J. Crys. Growth **202**, 1 (1999).

[3] C.T. Foxon and B.A. Joyce, *Growth and Characterisation of Semiconductors* (Adam Hilger, 1991) pp. 35.

[4] T. Vanbuuren, M.K. Weilmeier, I. Athwal, K.M. Colbow, J.A. Mackenzie, T. Tiedje, P.C. Wong and K.A.R. Mitchell, Appl. Phys. Lett. **59**, 464 (1991).

[5] A.J. Springthorpe, S.J. Ingrey, B. Emmerstorfer, P. Mandeville and W.T. Moore, Appl. Phys. Lett. **50**, 77 (1987).

[6] J. H. Neave, B. A. Joyce, and P. J. Dobson, Appl. Phys. a-Mater **34**, 179-184 (1984).

[7] J. M. Van Hove, C. S. Lent, P. R. Pukite, and P. I. Cohen, J. Vac. Sci. Technol. B **1**, 741 (1983).

[8] R. Farrow, *Molecular Beam Epitaxy* (Noyes, Park Ridge, NJ, 1995), pp. 84-87.

[9] R. Howland and L. Benatar, *A Practical Guide: To Scanning Probe Microscopy*. (Park scientific instruments, 1996).

[10] The atomic percentages of each element, C_A and C_B, and the XEDS intensities, I_A and I_B, can be related as follows: $C_A/C_B = k_{AB}(I_A/I_B)$, where k_{AB} is the Cliff-Lorimer factor.

Chapter 3

Influence of Wetting Layers and Quantum Dot Size Distribution on Intermediate Band Formation in InAs/GaAs Superlattices

3.1 Overview

We examine the influence of the wetting layers (WLs) and the quantum dot (QD) size distribution on the sub-bandgap external quantum efficiency (EQE) of QD solar cells. We use a finite-element Schrödinger-Poisson model that considers QD and wetting layer shapes, sizes, and spacings from cross-sectional scanning tunneling and atomic force micrographs. A comparison between experiments and computations reveals an insignificant contribution of the WL to the sub-bandgap EQE and a broadening of sub-bandgap EQE associated with a variation in QD sizes in the growth direction.

This chapter opens with background information on earlier studies regarding QD-based solar cells and the influence of WL and the QD size variation on *p-i-n* structures containing QDs. Next, the experimental and computational details of these investigations are described. We then discuss the influence of QD sizes and WLs on sub-bandgap EQE of QD solar cells. The chapter concludes with a summary.

3.2 Background

Quantum dot (QD) superlattices (SLs) have been proposed for improving solar cell efficiency by providing intermediate energy bands to allow sub-bandgap photon absorption,[1,2] and for enhancing the photocurrent in tandem solar cells.[3] Although photocurrent enhancement from QD-based solar cells has been demonstrated,[4,5,6,7,8,9,10,11,12,13,14] QD cells have consistently exhibited lower open-circuit voltages (V_{OC}) and conversion efficiencies than the GaAs reference cells. The QD cells to date have involved "zero-dimensional" structures produced using the Stranski-Krastanov (SK) growth process. SK QD structures have been reported to contain two-dimensional wetting layers (WLs) and a distribution of QD sizes,[1516] which are expected to influence the energies and broadening of the intermediate bands (IBs). A comparison of the properties of *p-i-n* heterostuctures containing either SK InAs QDs or thin InAs layers reveals insignificant external quantum efficiency (EQE) sub-bandgap absorption due to the WL in comparison with cells containing only QDs.[17] A comparison of calculated energy level splittings for a vertically aligned pair of InAs QDs in a GaAs matrix with identical or variable sizes in adjacent layers reveals a more significant level splitting for the QD pair with size variation.[18] However, the influence of the WL and the QD size variation on the EQE of *p-i-n* heterostructures containing multilayer QD arrays has not yet been reported.

Here, we examine the relative influence of the WL and the QD size distribution on the sub-bandgap EQE of molecular beam epitaxially (MBE) grown QD solar cells. Realistic QD shapes, sizes, and SL vertical period from cross-sectional scanning tunneling microscopy (XSTM) and areal densities from atomic force microscopy (AFM) are used as input into finite-element Schrödinger-Poisson calculations of the EQE. A comparison between experiments and simulations reveals a broadening of sub-bandgap EQE associated with a variation in QD sizes in the growth direction and an insignificant contribution of the WL to the sub-bandgap EQE. This unique combination of experiment and theory provides new insight for designing QD SLs for a wide variety of applications.

3.3 Experiments

The heterostructures were grown on Zn-doped *p*-GaAs (001) substrates by molecular beam epitaxy (MBE), using solid Ga, Be, Si, Al, In, and As_2 sources. The target doping concentrations were ~$1x10^{18}$ cm^{-3} for both *p*- and *n*-type layers. An initial 250-nm-thick Be-doped *p*-GaAs and a 500-nm-thick undoped GaAs buffer layer were grown at 580°C, followed by a 20-nm-thick undoped GaAs layer grown at 500°C, both with a V:III ratio of 12:1. Subsequently, three-period InAs/GaAs QD SLs consisting of 2.6 monolayers (ML) of InAs and a 5 nm GaAs spacer were grown at 500°C.[19] This approach is expected to lead to the formation of QDs via a Stranski-Krastanov (SK) growth mode transition. For the *p-i-n* structure, the final QD layer was capped with a 500-nm-thick layer of undoped GaAs. Next, layers of 200-nm-thick *n*-GaAs, 50-nm-thick $Al_{0.3}Ga_{0.7}As$, and 20-nm-thick heavily doped *n*-GaAs were then grown in succession. For the control *p-i-n* heterostructures, 15-nm-thick GaAs layer was grown instead of the QD layers. To reduce the quasi-Fermi level discontinuities within the QD SL, a total *i*-layer thickness of >1 μm was utilized. 2×2 mm^2 cells without anti-reflection coatings were fabricated using standard photolithography with front Ge/Ni/Au n-type and back Au/Zn p-type contacts deposited by e-beam evaporation. The front contact shadowing was ~6% of the surface area.

The EQE as a function of wavelength (λ) was measured with a halogen lamp calibrated with a National Institute of Standards and Technology traceable silicon photodetector. Low-intensity illumination ($<<100$ mW/cm^2) from the halogen lamp was modulated by a chopper, spectrally-filtered with a monochromator, and guided via an optical fiber to the sample. The photocurrent was then measured at room temperature using a lock-in amplifier referenced to the chopper frequency. The EQE was also calculated using a finite-element solution of the Poisson and Schrödinger equations. Strain fields in QDs were calculated using a finite-element continuum elasticity model with QD dimensions and WL indium concentration gradients determined by XSTM.[15] Additional details of the finite-element Schrödinger-Poisson calculations are provided in Appendix F.

AFM was performed on samples grown with similar conditions except that the final QD layer was left uncapped. XSTM measurements were obtained on samples grown in a similar manner but with five-period InAs/GaAs QD SLs on *n*-GaAs and capped with *n*-GaAs.[16] To differentiate the GaAs and QDs within the XSTM images, we estimated the tip height criterion as follows. Bright regions protruding at least 4.2 Å above the GaAs background were assessed as possible QDs. Within the bright regions, pixels with tip heights of at least 1.8 Å above the GaAs background were considered to be part of the

QD.[20] We examined several high resolution XSTM images and obtained QD height and lateral size distributions from more than 100 QDs.

3.4 Influence of QD Sizes on EQE

Figure 3.1(a) shows an AFM image of an InAs/GaAs QD SL, with QD density of $\sim 1.0\times 10^{10}$ cm^{-2}. Figure 3.1(b) shows a representative XSTM image of the QD SLs. In Figure 3.1(b), fringes with a spacing of 5.65 and 6.06 Å, corresponding to the (001) planes of GaAs and InAs, respectively, are observed in the darker and brighter regions of the image. The distribution of QD sizes, estimated from several high resolution XSTM images, is presented in Figure 3.2 for each period of QDs. We fit the size distributions with a Gaussian distribution for QD frequency as a function of diameter (or height) and used the maximum likelihood estimation method[21] to obtain the most probable QD diameter (or height). For the 1st, 2nd, and 3rd period of QDs, the maximum likelihood diameters (heights), d_{ML} (h_{ML}), are 12.0±0.5, 15.9±0.5, and 19.4±0.5 nm (3.5±0.3, 3.8±0.3, and 4.1±0.3 nm), respectively.

To compute the optical absorption and EQE of the 3-period QD SLs, we assume axially-symmetric ellipsoids with d_{ML} and h_{ML} as defined in Figure 3.2, and 100 nm (5.8 nm) lateral (vertical) SL periods. We then compare the experimental and computed EQEs for the following configurations: three SLs containing identically sized QDs with diameter (height) of 12.0 (3.5) nm, 15.9 (3.8) nm, and 19.4 (4.1) nm without WLs; SLs with increasing QD sizes in the subsequent layers, as listed in Table 1, embedded in either GaAs or $In_xGa_{1-x}As$ WLs; and SL with three period of WLs only.

To consider the effect of QD size variations, we compare the calculated EQEs for SLs containing identically sized QDs without WLs. The calculated EQEs are plotted in Figure 3.3(a), where the additional spectral response at wavelengths longer than the GaAs absorption edge (at λ=870 nm) is apparent for all SLs.

To quantify the position of sub-bandgap EQE peak, we consider the weighted mean of the calculated sub-bandgap EQE, which can be defined as the integral of the sub-bandgap EQE weighted by the wavelength and then divided by the integral of the sub-bandgap EQE, as shown below:

$$m = \int_{\lambda_1}^{\lambda_2} EQE(\lambda)\lambda d\lambda \,/ \int_{\lambda_1}^{\lambda_2} EQE(\lambda) d\lambda \,,$$

where λ_1 =870 nm and λ_2 =1100 nm. Here, m=910, 916, and 932 nm for a SL with QD diameters of 19.4, 15.9, and 12.0 nm, respectively. Due to the reduction in QD volumetric fraction and average transition matrix element, the calculated EQE is reduced from 1.44 % to 0.6 % as QD diameter decreases from 19.4 to 12 nm. For a fixed QD aspect ratio, the sub-bandgap EQE is expected to blue-shift with the decreasing QD size due to stronger quantum confinement. However, we do not observe a clear trend in the sub-bandgap EQE as QD size decreases, presumably due to the effect of aspect ratio of the ellipsoidal QDs on quantum confinement and the attendant variation in inter-dot spacing. In particular, it has been suggested that decreasing QD spacing can result in a blueshift in QD emission energy.[22] In our case, the vertical spacing between the QDs decreases with increasing QD sizes, which can lead to a blue-shift in the sub-bandgap EQE that counterplays the influence of QD size on the sub-bandgap EQE.

3.5 Influence of QD Size Distribution and Wetting Layers

We have also examined the influence of vertical variations in QD sizes by comparing the calculated EQE for QD SL with variations in QD sizes between layers along the vertical growth direction with the experimental EQEs of the control and QD cells, as shown in Figure 3.3(b). The calculated EQEs in Figure 3.3(b) exhibit a broad sub-bandgap EQE extension similar to that of the measured EQE of the QD cell. The weighted mean of the calculated EQE for the QD SL with varying diameters, m = 927 nm, also agrees well with the experimental value of 922 nm.

To account for the WL contributions to the sub-bandgap EQE, we compare the calculated EQEs of (1) SL with WLs only and SLs with vertical QD size variation (2) without and (3) with WLs, with the experimental EQE of the QD cell, as shown in Figure 3.3(c). When WLs are included in the SL, the calculated EQE = 1.02% at λ=920 nm (the wavelength corresponding to the weighted mean of the sub-bandgap EQE), which leads to improved agreement with the experimental value of 1.04%. The small discrepancy might be due to additional spectral broadening of photocurrent response resulting from in-plane QD size distributions. In addition, the WL contribution to the sub-bandgap EQE is much smaller and narrower than that of the QDs. At λ=920 nm, the calculated WL EQE = 0.17%, while the QD EQE = 0.82%. This is consistent with experimental observations, for which a peak associated with the WL is not apparent. The WL contribution is small due to its low strain-induced confinement potentials (~41 meV for the maximum CB potential; ~8mV for the VB), small average matrix element, and low interband absorption strength.

3.6 Conclusions

In summary, we have studied the influence of WL and QD size variation on sub-bandgap EQE of QD solar cells using a finite-element Schrödinger-Poisson model that considers realistic QD sizes and shapes obtained from MBE-grown InAs QD on GaAs structures. A comparison between experiment and simulation reveals a broadening of sub-bandgap EQE associated with a variation in QD sizes in the growth direction. Furthermore, the inhomogeneous WL contribution to the sub-bandgap EQE is predicted to be much weaker than that of the QD SLs. A recent study further suggests that the limited photocurrent enhancement in QD solar cells with increasing layers of QD SLs can be attributed to an increased non-radiative recombination from carrier scattering.[23] In addition, Mellor *et al.* predict an substantial enhancement in sub-bandgap photocurrent with improved voltage preservation by reducing QD diameters to <10 nm while conserving QD surface coverage.[24,25]

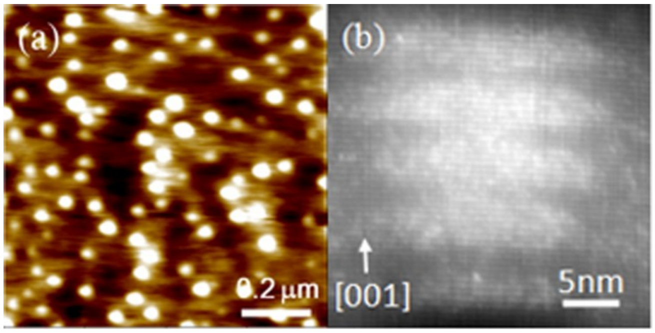

Figure 3.1 (a) AFM image of InAs/GaAs QD SLs grown on GaAs buffer layers. (b) High-resolution XSTM topographic image of InAs/GaAs QD SLs.

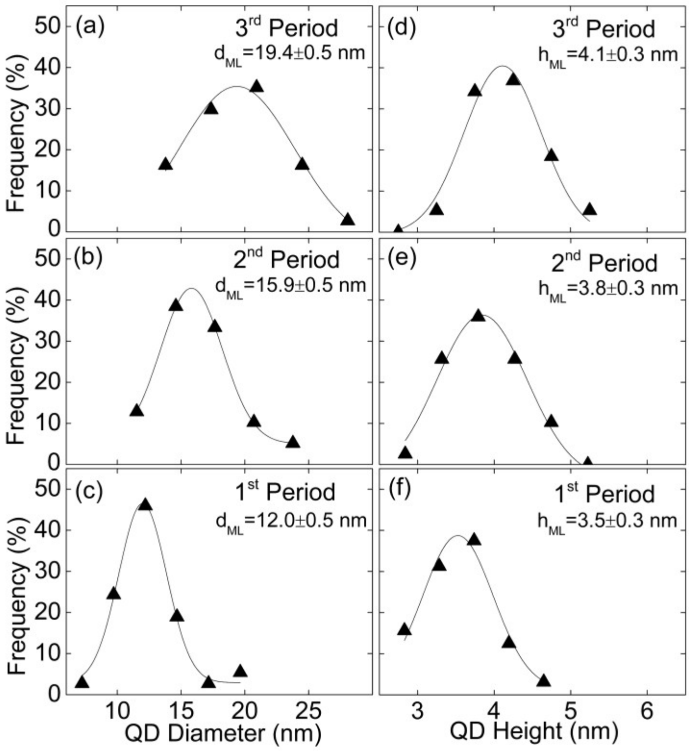

Figure 3.2 (a)-(f) The in-plane diameter and height distributions for each period of QDs determined from an analysis of XSTM images. The Frequency is the percentage of QDs with diameters or heights within a specified range. Fits to a Gaussian distribution are shown as solid lines, with χ values (a) 0.93, (b) 0.99, (c) 0.98, (d) 0.93, (e) 0.95, and (f) 0.88. For the 1st, 2nd, and 3rd period of QDs, a maximum likelihood estimate of QD diameters (heights) gives d_{ML} (h_{ML}) values of 12.0±0.5, 15.9±0.5, and 19.4±0.5 nm (3.5±0.3, 3.8±0.3, and 4.1±0.3 nm), respectively.

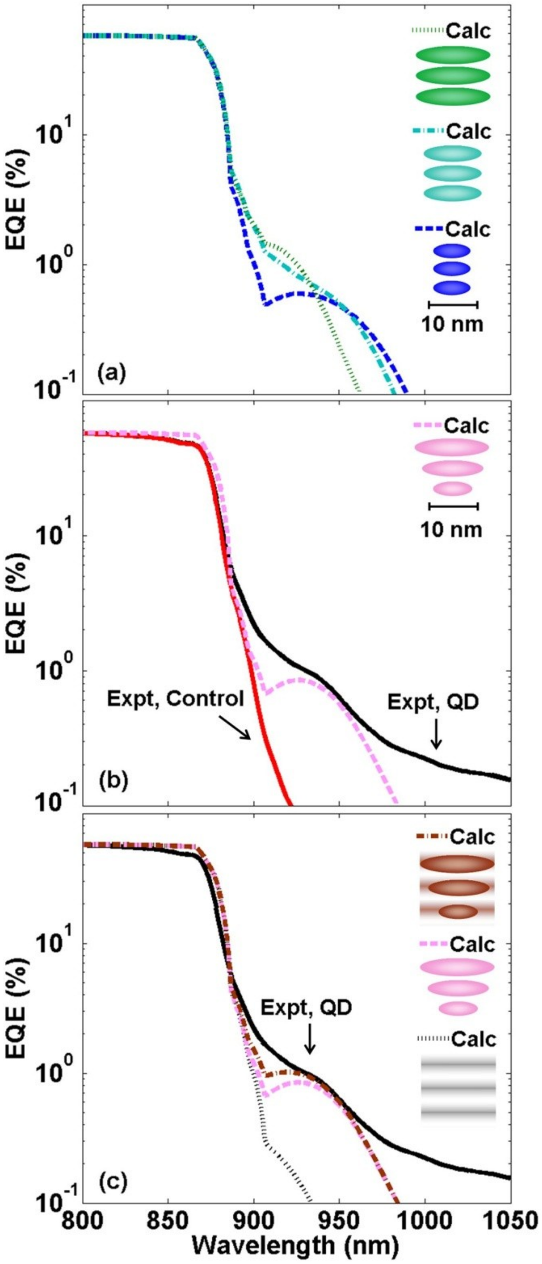

Figure 3.3 Plots of (a) computed EQEs vs. wavelength (λ) for three SLs containing identically-sized QDs without WLs. The input values of the QD diameters (heights), determined from an analysis of XSTM images, are 12.0 (3.5) nm, 15.9 (3.8) nm, and 19.4 (4.1) nm; (b) measured EQE vs. λ for the QD and control cells, along with the calculated EQE vs. λ values for QD SL with vertical size variations; and (c) measured EQE vs. λ for the QD cell, along with the computed EQE vs. λ values for the QD SLs with vertical size variations and WLs, and QD SLs with vertical size variation, but without WLs, and the WLs without QDs.

Table 1 Dimensions of the InAs QDs determined from an analysis of XSTM images.

Period	Height (nm)	Diameter (nm)
3rd	4.1 ± 0.3	19.4 ± 0.5
2nd	3.8 ± 0.3	15.9 ± 0.5
1st	3.5 ± 0.3	12.0 ± 0.5

3.7 References

---

[1] A. Luque and A. Marti, Phys. Rev. Lett. **78**, 5014 (1997).

[2] A.S. Brown, M.A. Green, J. Appl. Phys. **94**, 6150 (2003).

[3] S.M. Hubbard, C. Bailey, S. Polly, C. Cress, J. Andersen, D. Forbes, R. Raffaelle, J. Nanophotonics **3**, 031880 (2009).

[4] A.J. Grenko, I. Kimukin, J. Walker, and E. Towe, *Solar Energy: New Materials and Nanostructured Devices for High Efficiency (Solar)* (Stanford University, California, 2008), p. SWA4.

[5] A. Luque, A. Martí, N. López, E. Antolín, E. Cánovas, C. Stanley and C. Farmer, L. J. Caballero, L. Cuadra, J. L. Balenzategui, Appl. Phys. Lett. **87**, 083505 (2005).

[6] S.A. Blokhin, A.V. Sakharov, A.M. Nadtochy, A S. Pauysov, M.V. Maximov, N.N. Ledentsov, A.R. Kovsh, S.S. Mikhrin, V.M. Lantratov, S.A. Mintairov, N.A. Kaluzhniy, and M.Z. Shvarts, Semiconductors **43**, 514 (2009).

[7] A.G. Norman, M.C. Hanna, P. Dippo, D.H. Levi, R.C. Reedy, J.S. Ward, and M.M. Al-Jassim, *Proceedings of the 31st IEEE Photovoltaic Specialists Conference*, Lake Buena Vista, Florida, 2005, pp.43-48.

[8] C.O. McPheeters, C.J. Hill, S.H. Lim, D. Derkacs, D.Z. Ting, and E.T. Yu, J. Appl. Phys. **106**, 056101 (2009).

[9] D. Alonso-Álvarez, B. Alén, J. M. García, and J. M. Ripalda, Appl. Phys. Lett. **91**, 263103 (2007).

[10] D. Zhou, G. Sharma, S. F. Thomassen, T. W. Reenaas, B. O. Fimland, Appl. Phys. Lett. **96**, 061913 (2010).

---

[11] R B. Laghumavarapu, A. Moscho, A. Khoshakhlagh, M. El-Emawy, L.F. Lester, D.L. Huffaker, Appl. Phys. Lett. **90**, 173125 (2007).

[12] S.M. Hubbard, C .P. Cress, C. G. Bailey, R. P. Rafaelle, S. G. Bailey, and D. M. Witt, Appl. Phys. Lett. **92**, 123512 (2008).

[13] J. Wu, D. Shao, Z. Li, M. O. Manasreh,V. P. Kunets, Z. M. Wang, G. J. Salamo, Appl. Phys. Lett. **95**, 071908 (2009).

[14] Y. Okada, T. Morioka, K. Yoshida, R. Oshima, Y. Shoji, T. Inoue, T. Kita, J. Appl. Phys. **109** (2), 024301 (2011).

[15] B. Lita and R. S. Goldman, J. D. Phillips and P. K. Bhattacharya, Appl. Phys, Lett. **75**, 2797 (1999).

[16] B. Lita, R. S. Goldman, J. Phillips, P. K. Bhattacharya, Appl. Phys. Lett. **74**, 2824 (1999).

[17] D. Guimard, R. Morihara, D. Bordel, K. Tanabe, Y. Wekayama, M. Nishioka, and Y. Arakawa, Appl. Phys. Lett. **96**, 203507 (2010).

[18] L. R. C. Fonseca, J. L. Jimenez, J. P. Leburton, Phys. Rev. B **58**, 9955 (1998).

[19] W. Ye, S. Hanson, X. Weng, and R.S. Goldman, J. Vac. Sci. Technol. B **23**, 1736 (2005).

[20] V. D. Dasika, R.S. Goldman, J.D. Song, W.J. Choi, I.K. Han, J.I. Lee, J. Appl. Phys. **106**, 014315 (2009).

[21] P. R. Bevington, in *Data Reduction and Error Analysis for the Physical Sciences*, (McGraw-Hill, New York, 1969), p.110.

[22] H. Shin, E. Yoon, K.-S. Hong, W. Lee, Y.-H. Yoo, Appl. Phys. A **81**, 715 (2005).

---

[23] A. V. Semichaevsky and H. T. Johnson, Solar Energy Materials & Solar Cells **108**, 189 (2013).

[24] Alexander Mellor, Antonio Luque, Ignacio Tobías, and Antonio Martí, Appl. Phys. Lett. **101**, 133909 (2012).

[25] Alexander Mellor, Antonio Luque, Ignacio Tobías, and Antonio Martí, AIP Advances **3**, 022116 (2013).

Chapter 4

Mechanisms of InAs/GaAs Quantum Dot Formation during Annealing of In Islands

4.1 Overview

We have examined the formation mechanisms of InAs quantum dots (QDs) via annealing In islands in an As flux. We report two distinct mechanisms, droplet epitaxy (DE) and solid phase epitaxy (SPE), which depend on the As surface coverage. On c(4x4) GaAs surfaces, QDs form by DE. For c(4x4)α, one-to-one conversion from In islands to InAs QDs is observed. For c(4x4)β, lower densities of larger QDs are observed, presumably due to enhanced In surface diffusion in the absence of metastable Ga-As dimers. For the As capped surface, In deposition leads to an amorphous film, from which QDs nucleate by SPE during annealing.

This chapter opens with background information on earlier studies regarding the formation of metal droplets or islands and their conversion to QDs via annealing under an As flux. Next, the experimental details of these investigations are described. We then discuss the conversion of In islands to InAs QDs on the c(4x4)α and c(4x4)β GaAs surfaces. Finally, we consider the mechanism of QD formation on the As capped surface. The chapter concludes with a summary.

4.2 Background

Self-assembled semiconductor quantum dots (QDs) have been proposed for a wide variety of solid state devices, including solar cells,[1,2,3,4] lasers,[5] photodetectors,[6] and light emitting diodes.[7,8] Recently, the nucleation of metal droplets or islands and their conversion to QDs, often termed droplet epitaxy (DE),[9,10] has attracted much attention due to its flexibility for tuning QD sizes, densities, and materials combinations. Although DE has been reported in various materials such as GaAs/AlGaAs and InAs/GaAs,[10,11,12,13] conflicting results have been reported regarding the mechanisms for conversion of In islands to InAs QDs via As annealing. For example, Urbanczyk *et. al.*[14] showed a one-to-one conversion from In islands to InAs QDs. On the other hand, Kim *et al.*[10] reported additional nucleation of QDs following As exposure. In addition, Zhao *et al.*[15] reported QD nucleation during As annealing of droplet-free surfaces, presumed to be due to Stranski–Krastanov (SK) growth. Here, we investigate the formation mechanisms of In islands and their conversion to InAs QDs via As annealing. We report two distinct mechanisms, DE and solid phase epitaxy (SPE), which depend on As surface coverage. On c(4x4) GaAs surfaces, QDs form by DE, in which case one-to-one conversion from In islands to InAs QDs occurs on c(4x4)α. For c(4x4)β, enhanced In surface diffusion leads to lower densities of larger QDs. For the As capped surface, QDs nucleate by SPE during As annealing of an amorphous film. These mechanisms are likely to be applicable to a wide range of compound semiconductors.

4.3 Experiments

The InAs QDs were grown on epiready GaAs (001) substrates by molecular beam epitaxy (MBE), using solid Ga, As_2 or As_4, and In sources. The surface reconstruction was monitored *in situ* with a STAIB RH 30 RHEED source, operating at 18 keV. Each sample contained an initial 500 nm thick GaAs buffer layer grown at 500 °C with a growth rate of 1 μm/hr and a V/III beam-equivalent pressure (BEP) ratio of ~12 or ~20 for As_2 or As_4 sources, respectively. Next, various annealing steps were used to achieve a variety of buffer surface reconstructions. The c(4x4)α [c(4x4)β] buffer surfaces were prepared by annealing at 500 °C for 10 minutes with As_4 (As_2), followed by 10 minutes annealing at 450 °C with half the original As_4 (As_2) flux.[16] The "As capped" buffer surface was prepared by annealing with As_2 at 500 °C for 5 minutes. Next, the substrate temperature (T_S) was decreased to 300 °C, at which point the As shutter was closed, and the growth chamber background pressure gradually dropped to $< 1.5\times 10^{-9}$ Torr. Finally, the T_S was decreased to 100 °C, and 1.7 to 9.1 ML In was deposited with a rate of 0.1 ML/s. Some of the samples were subsequently exposed to the As_4 or As_2 flux for 2 minutes at 100 °C, followed by an additional 5 minutes of As annealing at 320°C. The surface morphology of the In islands and InAs films before and after As annealing was examined *ex situ* with tapping mode atomic force microscopy (AFM), using etched Si probes. The formation of QDs consisting primarily of crystalline InAs, is revealed by high resolution transmission electron microscopy (HRTEM), which is discussed in detail in Chapter 5.

4.4 Conversion of In Island to InAs QDs on c(4x4) GaAs Surfaces

For the lowest As coverage [c(4x4)α surface], we describe the nucleation of In islands and their conversion to InAs QDs. Figure 4.1 shows RHEED patterns collected along the [110] axis for In islands (a) before and (b) after As annealing. Prior to As annealing, the RHEED pattern, presented in Figure 4.1(a), shows a hazy spotty pattern with extra diffraction features, presumably due to the nucleation of crystalline In islands on GaAs.[17] Following As annealing, the RHEED pattern, shown in Figure 4.1(b), transforms to a spotty pattern without extra features, which suggests InAs QD formation.[10,17] Figure 4.2(a) and (b) [(d) and (e)] show AFM images of 3 and 5 ML (3.2 and 5.5 ML) In islands (InAs QDs), with corresponding island size distributions presented in Figure 4.1(c) [(f)]. We fit the size distributions with a Gaussian distribution for island frequency as a function of diameter and used the maximum likelihood estimation method to obtain the most probable island diameter, which is equivalent to the mean diameter, d_m. For 3 and 5 ML In islands (3.2 and 5.5 ML InAs QDs) on the c(4x4)α surface, d_m values are 17 ± 4 and 29 ± 6 nm (31 ± 6 and 32 ± 6 nm) with densities of 2.6×10^{10} and 2.0×10^{10} cm^{-2} (1.6×10^{10} and 2.9×10^{10} cm^{-2}), respectively. A comparison between the In islands and InAs QDs shows a slight increase in QD sizes (with similar

QD densities) upon As annealing, suggesting a nearly one-to-one conversion from In islands to InAs QDs, with limited QD coarsening during As annealing step.

For the medium As coverage [c(4x4)β surface], following As annealing, the In islands again convert to InAs QDs, with corresponding RHEED patterns shown in Figure 4.1(a) and (b), respectively. Figure 4.3(a) and (b) [(d) and (e)] show AFM images of 2.7 and 4.5 ML (2.7 and 4 ML) In islands (InAs QDs), with corresponding island size distributions presented in Figure 4.3(c) [(f)]. For 2.7 and 4.5 ML In islands (2.7 and 4 ML InAs QDs) on the c(4x4)β surface, the d_m are 34 ± 6 and 42 ± 9 nm (50 ± 5 and 120 ± 10 nm) with densities of 6.6×10^9 and 9.5×10^9 cm^{-2} (7.7×10^9 and 9.0×10^8 cm^{-2}), respectively. Apparently, the d_m values for QDs grown on the c(4x4)β surface increase significantly following As annealing. In particular, for 4ML In exposure, the d_m (density) increases (decreases) by ~3 times (one order of magnitude) following As annealing. The considerable increase (decrease) in QD diameter (density) suggests significant QD coarsening during As annealing step in this case.

4.5 Influence of In Exposure on QD Formation

To directly compare the In exposure dependence of both the In islands and the InAs QDs, we plot the diameters and densities as a function of In exposure, as shown in Figure 4.5(a) - (d), where symbols connected by dashed (solid) lines denote In islands (InAs QDs). For the c(4x4)α surface, as the In exposure is increased from 2 to 8 ML, the diameters of the In islands remain relatively small (~17-36 nm) with density in excess of

10^{10} cm^{-2}, as shown in Figure 4.5(a) and (c). Similarly, for up to ~9 ML In exposure, the diameters (densities) of QDs remain relatively small (high), as shown in Figure 4.5(b) and (d). On the c(4x4)β surface, as the In exposure is increased from 2.7 to 4.5 ML, the In island diameter increases from 34 to 42 nm, as shown in Figure 4.5(a); meanwhile, as the In exposure increases from 1.7 to 4 ML, the QD diameter (density) increases (decreases) from 43 to 120 nm (7.3×10^9 to 9.0×10^8 cm^{-2}). Apparently, for QDs grown on the c(4x4)α surface, the sizes (densities) are significantly smaller (higher), with a much weaker In exposure dependence compared to that of the QDs grown on the c(4x4)β surface. It has been reported that the c(4x4)α [c(4x4)β] surface contains Ga-As (As-As) dimers, which are energetically metastable (stable).[16] Hence, on the c(4x4)α surface, the surface diffusion of In atoms is likely to be inhibited by the metastable Ga atoms in the Ga-As dimers, leading to a lower surface diffusion length than that on the c(4x4)β surface. A similar trend has been reported for InAs QDs grown by the SK approach on the c(4x4)α and c(4x4)β GaAs surfaces.[18,19]

4.6 Conversion of In Island to InAs QDs on As Capped Surface

We now describe island nucleation and conversion to QDs for the highest As coverage (As capped surface). In this case, In deposition leads to the formation of both InAs film and In islands, which are subsequently converted to crystalline QDs during As annealing. Figure 4.4 shows AFM images of 3 ML In deposited on the As capped surface (a) before and (d) after As annealing, with the corresponding QD size distributions presented in Figure 4.4(f). For the As capped surface, island nucleation is limited by the excess As on the buffer surface. In particular, for 3 ML In exposure, a featureless surface, as shown in Figure 4.4(a), with a diffuse RHEED pattern, as shown in Figure 4.1(c), is observed, presumably consisting of amorphous InAs. During the As annealing step, the diffuse RHEED pattern transforms to a spotty pattern, as shown in Figure 4.1(d), suggesting crystallization of the amorphous film and conversion to small QDs, as shown in Figure 4.4(d). On the other hand, for In exposure ~4.5ML, the nucleation of large In islands (d_m > 48 nm) with low density (~2.0×10^9 cm^{-2}), as shown in Figure 4.4(b), suggests that the excess As is fully consumed by the In deposition. Following As annealing, a high density of small QDs (d_m ~20 nm) was observed along with a low density of large QD clusters (d_m ~100 nm), as shown in Figure 4.4(e). The QD clusters most likely result from the conversion and coalescence of the pre-existing In islands. The nucleation of small QDs during As annealing is again attributed to the crystallization of the amorphous film, as discussed above.

Apparently, for In exposure in the range of 1.9 to 4.8 ML, As annealing leads to the formation of small QDs with densities in excess of 10^{10} cm^{-2}, with a weak dependence on the In exposure, as shown in Figure 4.5(b) and (d). QD formation during As annealing of droplet-free surfaces has also been reported following the deposition of In on a Ga-rich surface.[15] However, since In is deposited on an As capped surface in our case, we propose a QD formation mechanism based upon SPE. Specifically, we propose that In deposition leads to the formation of an amorphous film, as shown in Figure 4.6(a). During As annealing, the thickness of crystalline InAs increases as the amorphous film crystallizes. The thickness dependence of the InAs/GaAs interface energy then drives the formation of QDs by SK growth during SPE, as shown in Figure 4.6(b). A similar mechanism has been reported for SPE-induced QD formation in the Ge/Si system.[20,21,22]

4.7 Conclusions

In summary, we have studied the formation mechanisms of In islands and their conversion to InAs QDs via annealing in an As flux. We report two distinct QD formation mechanisms, DE and SPE, which depend on As surface coverage. For low to medium As coverage, QD formation follows the DE mechanism. For the c(4x4)α surface, a one-to-one conversion from In islands to InAs QDs is observed. On the other hand, lower densities of larger QDs are observed on the c(4x4)β surface, presumably due to an enhanced In surface diffusion length in the absence of metastable Ga-As dimers. For the highest As coverage, In deposition leads to the formation of an amorphous film on the As capped surface. During As annealing, the interface energy increases as the amorphous film crystallizes, driving the formation of QDs by SPE. These mechanisms are likely to be applicable to a wide range of compound semiconductors.

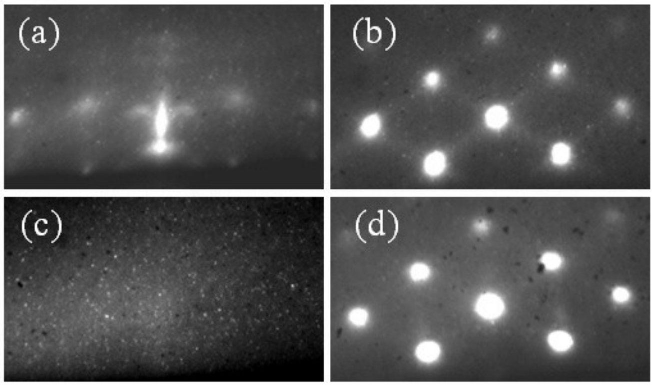

Figure 4.1 RHEED patterns collected along the [110] axis for In islands (a) before and (b) after As annealing on the c(4x4)α surface, and for amorphous InAs film (c) before and (d) after As annealing on the As capped surface. For In islands grown on the c(4x4)β surface, the RHEED patterns are essentially identical to (a) and (b).

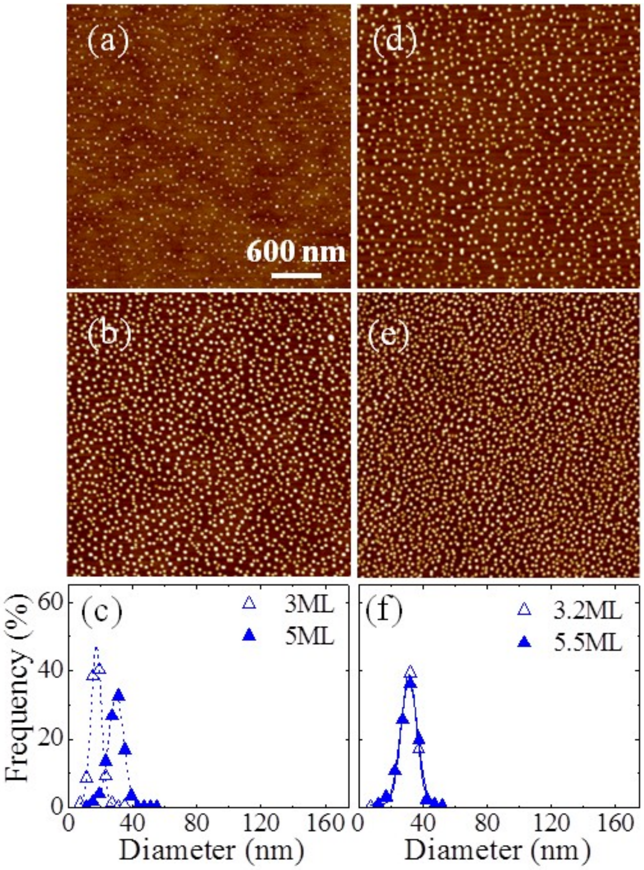

Figure 4.2 AFM images of (a) 3 and (b) 5 ML In islands and (d) 3.2 and (e) 5.5 ML InAs QDs grown on the c(4x4)α surface. The corresponding size distributions from images (a) and (b) [(d) and (e)] are shown in (c) [(f)]. The Frequency is the percentage of islands with diameters within a specified range.

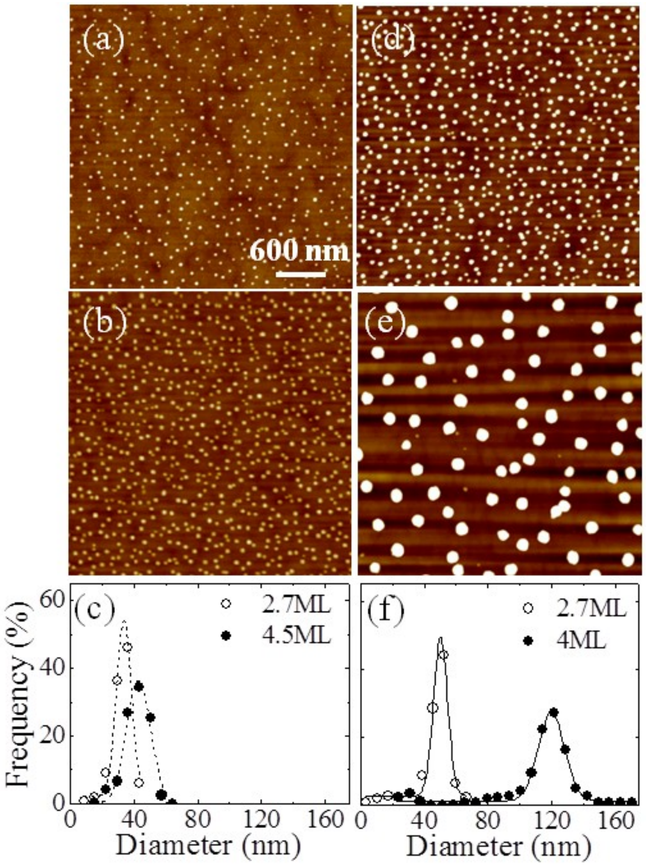

Figure 4.3 AFM images of (a) 2.7 and (b) 4.5 ML In islands and (d) 2.7 and (e) 4 ML InAs QDs grown on the c(4x4)β surface. The corresponding size distributions from images (a) and (b) [(d) and (e)] are shown in (c) [(f)].

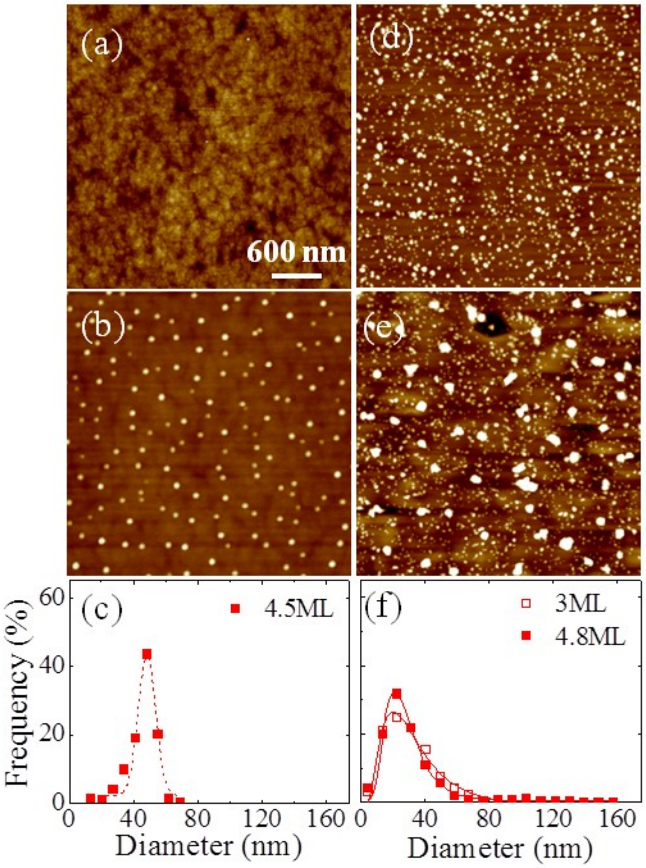

Figure 4.4 AFM images of (a) 3 ML InAs film, (b) 4.5 ML In islands, (d) 3 and (e) 4.8 ML InAs QDs grown on the As capped surface. The corresponding size distributions from image (b) [(d) and (e)] are shown in (c) [(f)].

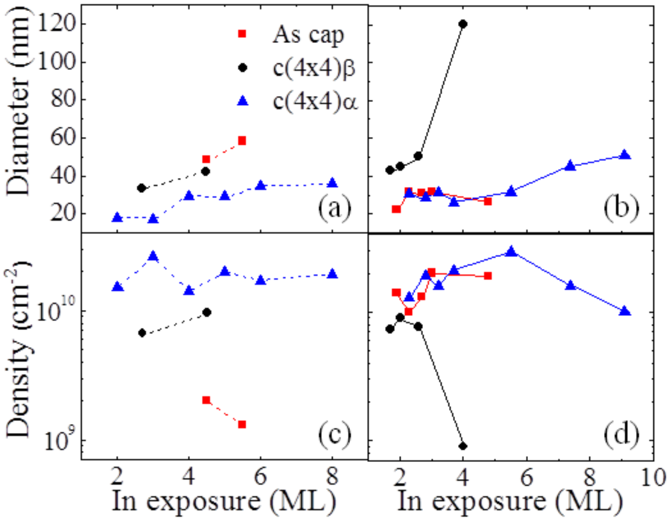

Figure 4.5 Plots of the mean diameter and the density of In islands [(a) and (c)] and InAs QDs [(b) and (d)] as a function of In exposure. Symbols connected by dashed (solid) lines represent In islands (InAs QDs).

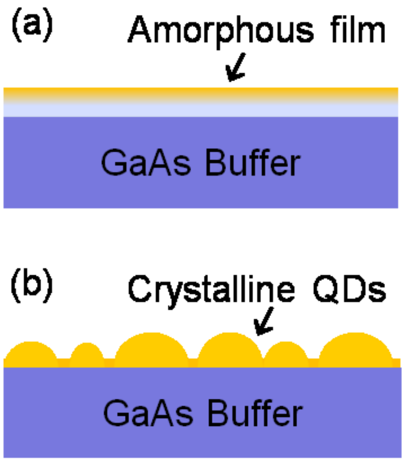

Figure 4.6 Schematic illustration for the solid phase epitaxy QD formation on an amorphous capped surface: (a) In deposition leads to the formation of an amorphous film, and (b) formation of the crystalline QDs driven by the misfit strain as the amorphous film crystallizes during annealing under an As flux.

4.8 References

---

[1] A. Marti, L. Cuadra, and A. Luque, in *Conference Record of the Twenty-Eighth Ieee Photovoltaic Specialists Conference - 2000* (IEEE, New York, 2000), pp. 940-943.

[2] A. Marti, E. Antolin, C. R. Stanley, C. D. Farmer, N. Lopez, P. Diaz, E. Canovas, P. G. Linares, and A. Luque, Phys. Rev. Lett. 97, 247701 (2006).

[3] S. Huang, A. V. Semichaevsky, L. Webster, H. T. Johnson, and R. S. Goldman, J. Appl. Phys. 110, 073105 (2011).

[4] A. Scaccabarozzi, S. Adorno, S. Bietti, M. Acciarri and S. Sanguinetti, Phys. Status Solidi RRL 7, 173 (2013).

[5] D. L. Huffaker, G. Park, Z. Zou, O. B. Shchekin, and D. G. Deppe, Appl. Phys. Lett. 73, 2564 (1998).

[6] J. Phillips, K. Kamath, and P. Bhattacharya, Appl. Phys. Lett. 72, 2020 (1998).

[7] N. M. Park, T. S. Kim, and S. J. Park, Appl. Phys. Lett. 78, 2575 (2001).

[8] J. X. Chen, A. Markus, A. Fiore, U. Oesterle, R. P. Stanley, J. F. Carlin, R. Houdre, M. Ilegems, L. Lazzarini, L. Nasi, M. T. Todaro, E. Piscopiello, R. Cingolani, M. Catalano, J. Katcki, and J. Ratajczak, J. Appl. Phys. 91, 6710 (2002).

[9] N. Koguchi, S. Takahashi, and T. Chikyow, J. Cryst. Growth 111, 688 (1991).

[10] J. S. Kim and N. Koguchi, Appl. Phys. Lett. 85, 5893 (2004).

[11] N. Koguchi and K. Ishige, Jpn. J. Appl. Phys. 32, 2052 (1993).

[12] E. Cohen, S. Yochelis, O. Westreich, S. Shusterman, D. P. Kumah, R. Clarke, Y. Yacoby, and Y. Paltiel, Appl. Phys. Lett. 98, 243115 (2011).

[13] T. Noda and T. Mano, Appl. Surf. Science 254, 7777 (2008).

---

[14] A. Urbanczyk and R. Notzel, J. Cryst. Growth 341, 24 (2012).

[15] C. Zhao, Y. H. Chen, B. Xu, P. Jin, and Z. G. Wang, Appl. Phys. Lett. 91, 033112 (2007).

[16] A. Ohtake, P. Kocán, J. Nakamura, A. Natori, and N. Koguchi, Phys. Rev. Lett. 92, 236105 (2004).

[17] A. Urbanczyk, G. J. Hamhuis, and R. Notzel, J. Appl. Phys. 107, 014312 (2010).

[18] T. Sugaya, T. Amano, and K. Komori, J. Appl. Phys. 100, 063107 (2006).

[19] T. Sugaya, T. Amano, and K. Komori, J. Appl. Phys. 104, 083106 (2008).

[20] K. Sumitomo, T. Nishioka and T. Ogino, J. Vac. Sci. Technol. B 13, 387 (1995).

[21] D. Z. Hu, D. T. Zhao, W. R. Jiang, B. Shi, Y. L. Fan, and Z. M. Jiang, J. Cryst. Growth 236, 557 (2002).

[22] Y. Shinoda, N. Shimizu, H. Hibino, T. Nishioka, C. Heimlich, Y. Kobayashi, S. Ishizawa, K. Sugii, and M. Seki, Appl. Surf. Science 60, 112 (1992).

Chapter 5

Origins of Interlayer Formation and Misfit Dislocation Displacement in The Vicinity of InAs/GaAs Quantum Dots

5.1 Overview

We have examined the origins of interlayer formation and misfit dislocation (MD) displacement in the vicinity of InAs/GaAs quantum dots (QDs). For QDs formed by the Stranski-Krastanov mode, regularly-spaced MDs nucleate at the interface between the QD and the GaAs buffer layer. In the droplet epitaxy case, both In island formation and In-induced "nano-drilling" of the GaAs buffer layer are observed during In deposition. For low In exposure, the In islands are converted to InAs QDs upon annealing under As flux, with an InGaAs interlayer at the QD/buffer interface. Meanwhile, MDs nucleate at the QD/interlayer interface. For high In exposure, an InAs interlayer forms at the island/buffer interface during the In deposition step. Annealing under As flux leads to the conversion of In islands to InAs QDs without the presence of an InGaAs layer, resulting in MDs at the QD/buffer interface.

This chapter opens with background information on earlier studies regarding interlayer formation and MD vertical displacement in various material systems. Next, the experimental details of these investigations are described. We then discuss the microstructures and compositions of both Stranski-Krastanov (SK) and droplet epitaxy (DE) QDs. Furthermore, we compare the microstructures of DE QDs with various In exposure and discuss the mechanism of QD microstructural evolution. Finally, we propose an In-exposure-dependent mechanism for the conversion of In islands to InAs QDs, which explains the origins of interlayer formation and MD vertical displacement. The chapter concludes with a summary.

5.2 Background

Strain relaxation in highly lattice-mismatched thin film systems typically occurs by a combination of elastic relaxation via island formation and plastic relaxation via misfit dislocation (MD) nucleation.[1,2] These strain-induced islands, often termed quantum dots (QDs), have shown significant promise for a wide range of solid state applications, including photovoltaics,[3,4,5] lasers,[6] photodetectors,[7] and light emitting diodes.[8,9] Although MDs are usually observed at the interface between the QD and the buffer layer,[10,11,12,13,14] vertical MD displacement has been reported in various material systems. For example, Kim *et al.* observed MD displacement above the GaSb QD/GaAs interface in regions which also contained an intermediate layer, as shown in Figure 5.1(a).[15] On the other hand, Chen *et al.* attributed InAs QD/GaAs MD displacement to a surface oxidation-induced downward shift of the crystalline GaAs buffer surface, as presented in Figure 5.1(b).[16] However, in many cases, interfacial MDs at QD/buffer interface are also observed following air exposure, as shown in Figure 5.2.[10,11,12,15] Therefore, the origins of the interlayer formation and MD displacement need to be further examined.

Here, we report on the influence of growth mode on MD displacement in the vicinity of InAs/GaAs QDs. For QDs formed by the Stranski-Krastanov (SK) mode, arrays of regularly-spaced MDs nucleate near the interface between QD and GaAs buffer layer, similar to previous reports for strain-relaxed QDs with interfacial MDs.[10,13] In the droplet epitaxy (DE) case, both In island formation and In-induced "nano-drilling" of the GaAs buffer layer are observed during In deposition. For low In exposure, the In islands are converted to InAs QDs upon annealing under an As flux, with an InGaAs interlayer at the QD/buffer interface. Meanwhile, MDs nucleate at the QD/interlayer interface. For high In exposure, an InAs interlayer forms at the island/buffer interface during the In deposition step. Annealing under an As flux converts the rest of the In island to InAs QDs. The misfit strain at the QD/buffer interface then drives the nucleation of interfacial MDs for strain relaxation. By varying the amount of In exposure during DE, we demonstrate the formation of InAs QDs with MDs either at or above the QD/buffer interface. Thus, the DE approach enables the control of MD vertical displacement during QD formation, which is promising for tailoring carrier confinement in the vicinity of QDs.

5.3 Experiments

For these investigations, The InAs QDs were grown on epiready GaAs (001) substrates by molecular beam epitaxy (MBE), using solid Ga, As_2 or As_4, and In sources.

The surface reconstruction was monitored *in situ* with an 18 keV reflection high-energy electron diffraction (RHEED) source. Each sample contained an initial 500 nm thick GaAs buffer layer grown at 500 °C with a growth rate of 1 μm/hr and a V/III beam-equivalent pressure (BEP) ratio of ~12 or ~20 for As_2 or As_4 sources, respectively. Next, various annealing steps were used to achieve a variety of buffer surface reconstructions, thus enabling QD formation by either the DE or SK mode. Details of the buffer layers preparation and their correlation with the QD formation mechanisms are described in Chapter 4. Subsequently, the substrate temperature (T_S) was decreased to 300 °C, at which point the As shutter was closed, and the growth chamber background pressure gradually dropped to $< 1.5\times10^{-9}$ Torr. Finally, the T_S was decreased to 100 °C, and 3.0 to 5.5 monolayer (ML) In was deposited at a rate of 0.1 ML/s. Some of the samples were subsequently exposed to the As_4 or As_2 flux for 2 minutes at 100 °C, followed by an additional 5 minutes of As annealing at 320 °C. The microstructures and compositional profiles of the In islands and InAs QDs were examined *ex situ* with high resolution transmission electron microscopy (HRTEM), scanning TEM (STEM), and X-ray energy dispersive spectroscopy (XEDS). Cross-sectional TEM specimens were prepared using conventional mechanical polishing, followed by argon ion milling. HRTEM imaging was carried out in a JEOL JEM3100F operating at 300 kV. High resolution XEDS and STEM imaging were performed in a spherical aberration-corrected JEOL JEM2100F operating at 200 kV.

5.4 SK QD: Strain Relaxation via Interfacial Misfit Dislocations

We first describe the microstructures, composition, and MD nucleation for QDs formed by the SK mode. Figure 5.3(a) shows HRTEM image of a crystalline InAs SK QD with 4 ML In exposure, revealing average lattice fringe spacings of 3.09 and 3.43 Å for the QD, within 2.0 % of the {200} and {111} interplanar spacings of InAs, suggesting that the QD consists primarily of InAs. Furthermore, as indicated by the arrows in Figure 5.3(a), an array of regularly-spaced MDs is located near the interface between QD and GaAs buffer layer, similar to previous reports for strain-relaxed QDs.[10,14] These MDs are predominantly 90˚ edge dislocations, consistent with literature reports for MD nucleation at large lattice mismatch (> ~2.3%).[17] The average spacing between each MD, estimated from several HRTEM images, is 6.4 ± 0.9 nm, which corresponds to the relaxation of 6.7 % misfit strain between the InAs QD and the GaAs buffer layer,[18] similar to the mismatch between bulk InAs and GaAs (7%).

To determine the local lattice distortion in the vicinity of SK QDs, we perform geometric phase analysis (GPA) of the HRTEM images.[19,20] For GPA, we first calculate the power spectrum of the fast Fourier transformation (FFT) of the HRTEM image, as shown in Figure 5.3(b). We then select spots corresponding to the 002 and $1\bar{1}1$ reciprocal lattice points for both GaAs and InAs. The spots selected in Figure 5.3(b) are consistent with the reciprocal lattice points on the simulated diffraction pattern from both InAs (red) and GaAs (blue), shown in Figure 5.3(c). We use GPA to quantify the lattice distortion with respect to the GaAs reference lattice. Figure 5.3(d) shows the resultant in-plane lattice distortion map, for the SK QD shown in Figure 5.3(a). The color scale represents the magnitude of the lattice distortion along the in-plane direction, revealing a misfit of ~7 % between the QD and the buffer layer. The arrows in Figure 5.3(d) indicate the positions of local maxima in the lattice distortion, which agree with the locations of interfacial MDs shown in Figure 5.3(a).

5.5 DE QD: Influence of In Exposure on QD Microstructure

For QDs formed by DE, Figure 5.4(a) shows a HRTEM image of a crystalline QD with 5.5 ML In exposure, revealing an array of 90˚ MDs ~3 nm above the interface between the QD and the GaAs buffer layer. For the portion of the QD above the MD array, Figure 5.4(a) reveals average lattice fringe spacings of 3.10 and 3.53 Å, within 2.0 % of the {200} and {111} interplanar spacings of InAs, suggesting the presence of nearly pure InAs. For the portion of the QD below the MD array, Figure 5.4(a) reveals average lattice fringe spacings of 2.87 and 3.31 Å, significantly smaller than the {200} and {111} interplanar spacings of InAs, suggesting the presence of an $In_{0.18}Ga_{0.82}As$ alloy layer. At the InAs/InGaAs interface, the average MD spacing, estimated from several HRTEM images, is 7.9 ± 0.9 nm, which corresponds to the relaxation of ~5.4% misfit strain between the InAs and the InGaAs layer.[18,21] In addition, at the InGaAs/GaAs interface, at least one MD is observed beneath each InGaAs layer, as shown in Figure 5.5. We examined several HRTEM images spanning >0.5 μm along the InGaAs/GaAs interface, revealing an average width of <34 nm for the regions containing InGaAs layer, resulting in an effective MD spacing of <34 nm, which corresponds to the relaxation of 1.2% misfit strain between the InGaAs and the GaAs buffer layer.

To confirm the presence of the InGaAs alloy layer at the QD/buffer interface, we measured the atomic percents of In, Ga, and As within the QD, both above and below the MD array, as well as within the buffer layer. Figure 5.6 shows (a) an HR-STEM image of a crystalline QD with 5.5 ML In exposure and (b) a plot of atomic percents obtained from XEDS at points A (above MD array), B (below MD array), and C (buffer layer) in Figure 5.6(a). The XEDS data in Figure 5.6(b) suggest the presence of InAs at A, $In_{0.18}Ga_{0.82}As$ at B, and GaAs at C, consistent with the composition suggested by the lattice fringe spacings.

For DE QDs with higher In exposure, Figure 5.4(e) shows a HRTEM image of a crystalline QD with 7.5 ML In exposure, revealing average lattice fringe spacings of 3.01 and 3.52 Å for the QD, within 0.7 % of the {200} and {111} interplanar spacings of InAs, suggesting that the QD consists primarily of InAs. Interestingly, as indicated by the vertical arrows in Figure 5.4(e), an array of MDs is located at the interface between the InAs QD and the GaAs buffer layer, without the presence of an InGaAs alloy layer. In addition, the average MD spacing, estimated from several HRTEM images, is 6.4 ± 0.3 nm, which corresponds to the relaxation of 6.7 % strain between the InAs QD and the GaAs buffer layer.[18]

To determine the local lattice distortion in the vicinity of the DE QDs, we perform GPA of the HRTEM images shown in Figure 5.4(a) and (e). Power spectrums of the FFT of Figure 5.4(a) and (e) are shown in Figure 5.4(b) and (f), respectively. The selected spots in the power spectrum correspond to the 002 and $1\bar{1}1$ reciprocal lattice points, consistent with the simulated diffraction pattern shown in Figure 5.4(c) and (g). Figure 5.4(d) and (h) shows the in-plane lattice distortion maps from GPA, where the arrows indicate the positions of local maxima in lattice distortion, matching the locations of MDs shown in Figure 5.4(a) and (e), respectively. In addition, Figure 5.4(d) [(h)] reveals a misfit of ~6 % (~7 %) between the InAs and the InGaAs layer (the GaAs buffer layer), consistent with the misfit estimated from the XEDS data (the lattice fringe spacings).[21]

For lattice-mismatched systems, the interfacial energy, γ^*, is related to the elastic strain energy, E_ε, as follows: $\gamma^* = \gamma + E_\varepsilon$, where γ is the chemical component of the γ^* (depends on the strength of the chemical bonding).[22] To extract the γ for the SK and DE QDs, we estimate the E_ε as follows: $E_\varepsilon = \varepsilon^2 Bh$, where ε is the in-plane strain, h is the layer thickness, and B is a constant depends on the shear modulus and Poisson's ratio of the layer.[23,24] The estimated E_ε is 0.46 and 0.60 J/m^2 for the 4 ML SK QDs and the 7.5 ML DE QDs, respectively. For the 5.5 ML DE QDs, the estimated E_ε is 0.37 (0.03) J/m^2 for the InAs (InGaAs) layer. The above analysis presents a first-order approximation of the QD elastic strain energies, which can be more accurately calculated with finite element analysis. On the other hand, from Young's equation, we can estimate γ^* using the QD contact angles, θ_c,[25] as shown in Figure 5.7. The relationship between the θ_c, the surface energies, and the γ^* is illustrated in Figure 5.7(d).[26] The average θ_c, estimated from several HRTEM images, are 43 ± 2° and 56 ± 4° for the 4 ML SK QDs and the 7.5 ML DE QDs, respectively. For the 5.5 ML DE QDs, the average θ_c is 37 ± 4° (11 ± 2°) between the InAs and the InGaAs alloy layer (the InGaAs and GaAs buffer layer), as shown in Figure 5.7(b). The γ^* estimated from Young's equation is 0.53 and 0.65 J/m^2 for the 4 ML SK QDs and the 7.5 ML DE QDs, respectively. For the 5.5 ML DE QDs, the estimated γ^* is 0.41 (0.04) J/m^2 between the InAs and the InGaAs layer (the InGaAs and GaAs buffer layer). Finally, the γ can be extracted as follows: $\gamma = \gamma^* - E_\varepsilon$. As shown in previous sections, both the 4 ML SK QDs and the 7.5 ML DE QDs consist primarily of InAs, leading to similar $\gamma_{\text{GaAs-InAs}}$ of 0.06 and 0.05 J/m^2, respectively. For the 5.5 ML DE QDs, the estimated $\gamma_{\text{InGaAs-InAs}}$ ($\gamma_{\text{GaAs-InGaAs}}$) is 0.04 (0.01) J/m^2 for the InAs/InGaAs (InGaAs/GaAs) interface. The extracted γ values are on the same order of magnitude as previous prediction for the $\gamma_{\text{Ge-Si}}$.[27] Apparently, larger compositional difference between the layers leads to larger γ, suggesting stronger chemical bonding between more similar materials. In addition, this is the first report for γ between the In$_x$Ga$_{1-x}$As/GaAs interface, which can be used in first principle calculations for more accurate and comprehensive consideration of crystal growth in the lattice mismatched systems.

5.6 In-induced Nano-drilling and InAs Interlayer Formation

To investigate the origin of the InGaAs alloy layer at the QD/buffer interface and the In-exposure-dependent evolution of the DE QD microstructure, we examine the microstructure in the vicinity of the In islands prior to their conversion to the InAs QDs. Figure 5.8 shows (a) an HR-STEM image of a polycrystalline island with 5 ML In exposure, with a higher magnification view of the island/buffer interface in (b). Figure 5.8(b) reveals average lattice fringe spacings of 5.03 and 3.51 Å for the island, within 1.7 % of the {002} and {220} interplanar spacings of In_2O_3. The oxygen partial pressure in our MBE is typically < 1.0×10^{-12} Torr, significantly lower than the typical oxygen pressure (~10^{-5} Torr) used for MBE growth of In_2O_3.[28] Therefore, it is unlikely that the In islands would oxidize in our MBE. On the other hand, formation of In_2O_3 films (up to >20 nm) from In oxidation in air has been reported for temperatures ranging from 25 to 400˚C.[29] Thus, oxidation of the In islands presumably occurred following sample removal from the MBE.

Interestingly, the HR-STEM images at the island/buffer interface reveal concave up regions near the island centers. The RMS roughness at the island/buffer interface, estimated from several XTEM images, is ~0.91 nm, which is significantly higher than that of the buffer surface (~0.21 nm). Thus, the concavities at the island/buffer interface are unlikely to be related to GaAs surface roughness.[30] Instead, it is likely that In-induced "nano-drilling" (a.k.a. droplet etching) occurs on the GaAs buffer layer, similar to previous reports of DE-induced quantum ring and core-shell QD formation.[31,32,33,34,35] In the case of In deposition on GaAs at 100˚C, the In-GaAs phase diagram predicts the presence of liquid Ga when <1 atomic % of In is added into GaAs, as shown in the inset of Figure 5.9.[36] During the In deposition step, the incorporation of In into GaAs melts the GaAs buffer layer at the island/buffer interface, leading to In-induced nano-drilling into the GaAs buffer layer. Furthermore, the diameter of the In_2O_3 island is slightly larger than that of the nano-drilled hole, which can be attributed to the oxidation-induced volume expansion of the In island.[37]

In addition to the In-induced nano-drilling, for some of the islands with 5ML In exposure, the initiation of the conversion of In to InAs is apparent at the island/buffer interface following the In deposition step. In particular, Figure 5.10 shows (a) a HR-

STEM image of an In_2O_3 island with 5 ML In exposure and (b) a higher magnification view of the island, revealing a MD at the island/buffer interface, as indicated by a vertical arrow. Right above the MD at the island/buffer interface, a small crystalline region with average lattice fringe spacings of 3.06 and 3.53 Å, within 1.0% of the {200} and {111} interplanar spacings of InAs, is revealed by Figure 5.10(b), suggesting that the crystalline region right above the MD consists primarily of InAs.

For islands with high In exposure, Figure 5.11 shows (a) a HR-STEM image of an In_2O_3 island with 8 ML In exposure and (b) a higher magnification view of the island at the island/buffer interface. Figure 5.11(b) reveals an interlayer at the island/buffer interface with MDs at the interlayer/buffer interface, as indicated by the vertical arrows. For the portion within the interlayer, Figure 5.11(b) reveals average lattice fringe spacings of 3.04 and 3.53 Å, within 0.9 % of the {200} and {111} interplanar spacings of InAs, suggesting that the interlayer consists primarily of InAs. At the interlayer/buffer interface, the MD spacing is ~6.2 nm, corresponding to the relaxation of ~6.9% misfit strain between the InAs interlayer and the GaAs buffer layer.[18]

5.7 Mechanism of In Islands to InAs QDs conversion

Based on the microstructural and compositional information presented above, we propose the following mechanism for the conversion of In islands to InAs QDs. As depicted in Figure 5.13(a), In deposition on the GaAs surface at 100˚C leads to the formation of In islands rather than a wetting layer, which is consistent with previous prediction where complete wetting of In on GaAs surface would only occur above 420˚C.[38] Meanwhile, In nano-drills into GaAs buffer layer at the island/buffer interface, resulting in a concave up region at the island/buffer interface with small portions of In island converted to InAs, as shown in Figure 5.13(b). During the In deposition step, the formation of InAs at island/buffer interface can be attributed to the dissolution of As atoms (from GaAs) in the In island. As shown in the In-As phase diagram presented in Figure 5.12,[39] point A represents pure In solid (In islands). The dissolution of As atoms in the In islands moves the In solid from point A to B, which is in the two phase region of In and InAs solid, leading to the formation of InAs between the In island and the GaAs buffer layer. Subsequently, during the As annealing step at 320˚C, high concentration of As atoms surrounding the In droplets drives As diffusion into the In droplets, as shown in Figure 5.13(c). The As diffusion then drives the In droplets from pure In liquid (point C in Figure 5.12) to a two phase region of In liquid and InAs solid (point D in Figure 5.12). Continuous As supply from the As flux leads to the precipitation of crystalline InAs from In liquid until the entire In droplet is converted to InAs. For the In droplets with low In exposure, the As annealing step leads to significant In-Ga intermixing near the In/GaAs interface, suggesting that the thermal energy provided in the annealing step overcomes the activation energy of In-Ga inter-diffusion.[40] The In-Ga intermixing results in an InGaAs alloy layer at the QD/buffer interface, as shown in Figure 5.13(d). Finally, the large lattice misfit between InAs and InGaAs drives the nucleation of MDs at the interface between the InAs QD and the InGaAs alloy layer.

For high In exposure, during the In deposition step, longer In exposure allows more As dissolution (from GaAs) in the In islands, leading to InAs formation to proceed towards the center of the nano-drilled region. Upon completion of In deposition, an InAs interlayer forms between the In island and the GaAs buffer layer with MDs at the interlayer/buffer interface, as shown in Figure 5.13(e). During the As annealing step, the conversion of In to InAs can be attributed to the diffusion of As atoms (from the As flux) into the In droplets, as described above. In addition, the intermixing of Ga (from GaAs) and In (from In droplet) is hindered by the InAs interlayer at the droplet/buffer interface, as shown in Figure 5.13(f). Consequently, the In droplets are converted to InAs QDs without the presence of an intermixed InGaAs layer at the QD/buffer interface. The lattice misfit between the QD and the buffer layer drives the nucleation of MDs at the QD/buffer interface, as shown in Figure 5.13(g).

5.8 Conclusions

In summary, we have studied the origins of interlayer formation and MD displacement in the vicinity of InAs/GaAs QDs. For SK QDs, regularly-spaced MDs nucleate near the interface between the QD and the GaAs buffer layer. For DE, during In deposition, both In island formation and In-induced nano-drilling of the GaAs buffer layer are observed. Subsequently, for low In exposure, In islands are converted to InAs QDs during the As annealing step; meanwhile, an InGaAs alloy layer forms at the QD/buffer interface. The lattice misfit drives the nucleation of MD array at the interface between the QD and the InGaAs layer. Interestingly, for high In exposure, an InAs interlayer forms at the island/buffer interface during the In deposition step. Annealing under an As flux leads to the conversion of In islands to InAs QDs without the presence of an InGaAs alloy layer. The lattice misfit at the QD/buffer interface drives the nucleation of interfacial MDs for strain relaxation. By varying the amount of In exposure during DE, we demonstrate the formation of InAs QDs with MDs either at or above the QD/buffer interface. Thus, the DE approach enables the control of MD vertical displacement during QD formation, which is promising for tailoring carrier confinement in the vicinity of QDs. A suggested future work includes the investigation of the influence of substrate temperatures on the In-induced nano-drilling and the nucleation of MDs during DE of InAs QDs.

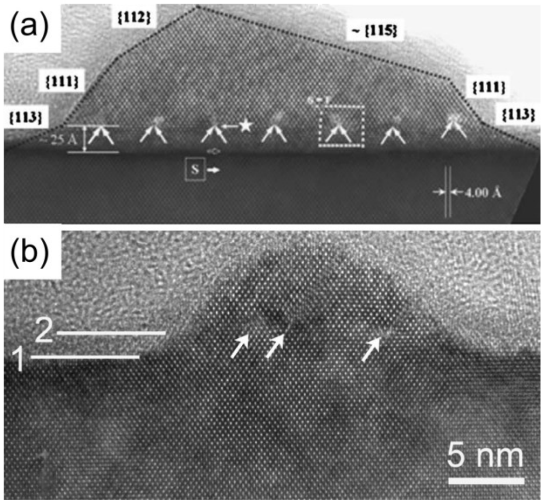

Figure 5.1 HRTEM images of (a) a GaSb/GaAs QD and (b) a InAs/GaAs QD with vertical displacement of misfit dislocations above the QD/buffer interface, as indicated by arrows. Horizontal lines in (b) indicate the top surface of 1-the crystalline GaAs buffer layer and 2-the oxide layer. Reprinted with permission from Ref. 15. (Copyright 2007, AIP Publishing LLC.) and Ref. 16 (Copyright 2012, Springer).

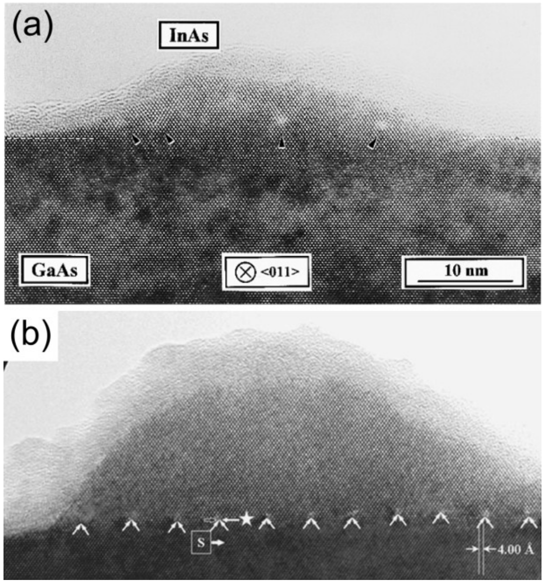

Figure 5.2 HRTEM images of (a) a InAs/GaAs QD and (b) a GaSb/GaAs QD with interfacial misfit dislocations at QD/buffer interface, as indicated by arrows. Reprinted with permission from Ref. 10 (Copyright 1995, AIP Publishing LLC.) and Ref. 15 (Copyright 2007, AIP Publishing LLC.)

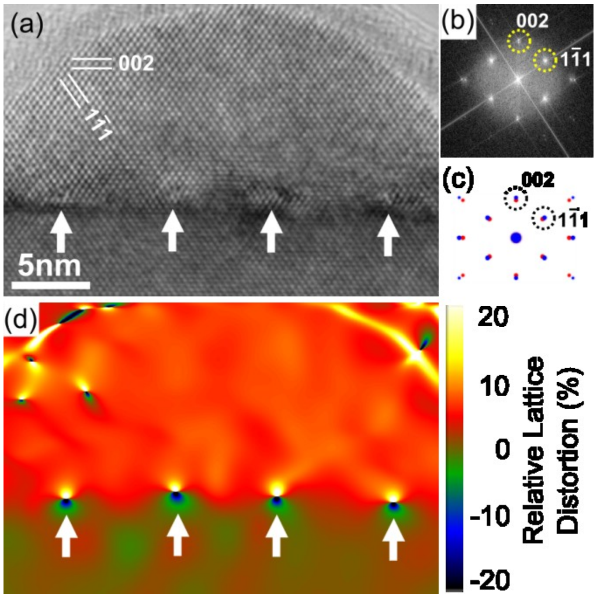

Figure 5.3 (a) HRTEM image of a crystalline InAs QD formed by Stranski-Krastanov mode (4ML In exposure), where misfit dislocations are indicated by vertical arrows. The corresponding fast Fourier transformation pattern is shown in (b), where the spots selected for geometric phase analysis (GPA) (circled with dashed lines) correspond to the 002 and $1\bar{1}1$ reflections, as indicated in the simulated diffraction pattern from both InAs (red) and GaAs (blue) shown in (c). The corresponding in-plane lattice distortion map from GPA of image (a) is shown in (d).

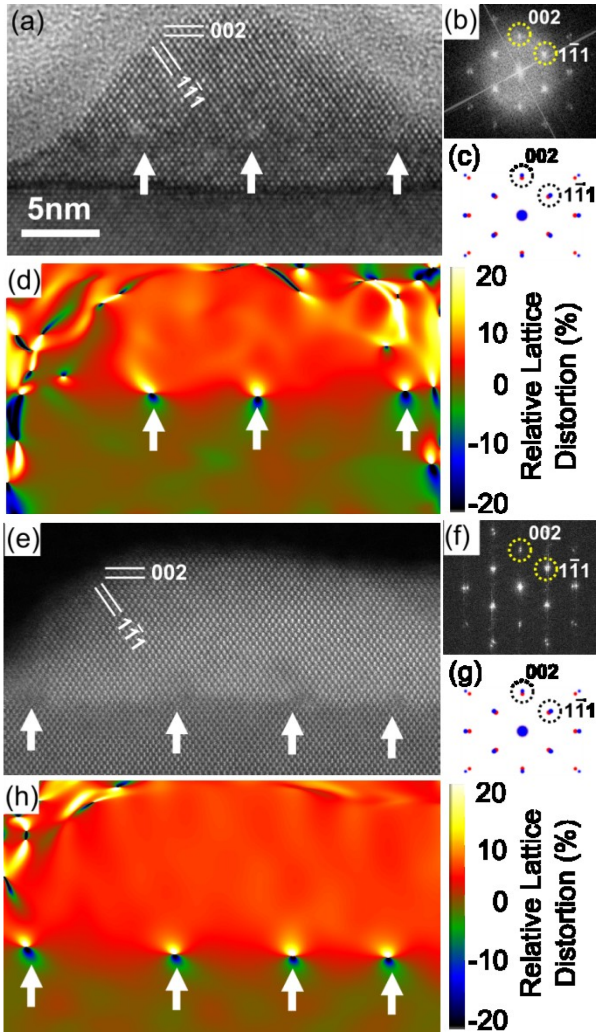

Figure 5.4 HRTEM images of crystalline InAs QDs formed by droplet epitaxy with (a) 5.5 ML In exposure and (e) 7.5 ML In exposure, where misfit dislocations are indicated by vertical arrows. The corresponding fast Fourier transformation patterns are shown in (b) and (f), where the spots selected for geometric phase analysis (GPA) (circled with dashed lines) correspond to the 002 and $1\bar{1}1$ reflections, as indicated in the simulated diffraction patterns from both InAs (red) and GaAs (blue) shown in (c) and (g). The corresponding in-plane lattice distortion maps from GPA of images (a) and (e) are shown in (d) and (h), respectively.

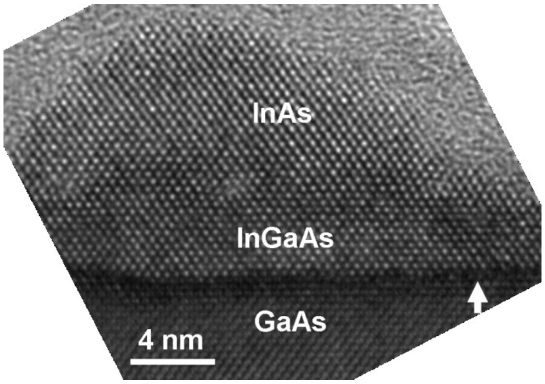

Figure 5.5 HRTEM image of a crystalline InAs QD (5.5 ML In exposure) formed by droplet epitaxy, where a misfit dislocation at the InGaAs/GaAs interface is indicated by a vertical arrow.

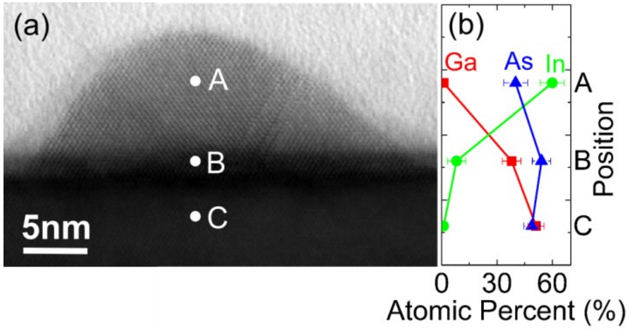

Figure 5.6 (a) High resolution scanning TEM image of a crystalline InAs QD formed by droplet epitaxy (5.5ML In exposure), with points A, B, and C denoting the locations where XEDS data were obtained. The corresponding atomic percents of In, Ga, and As obtained from XEDS are plotted in (b).

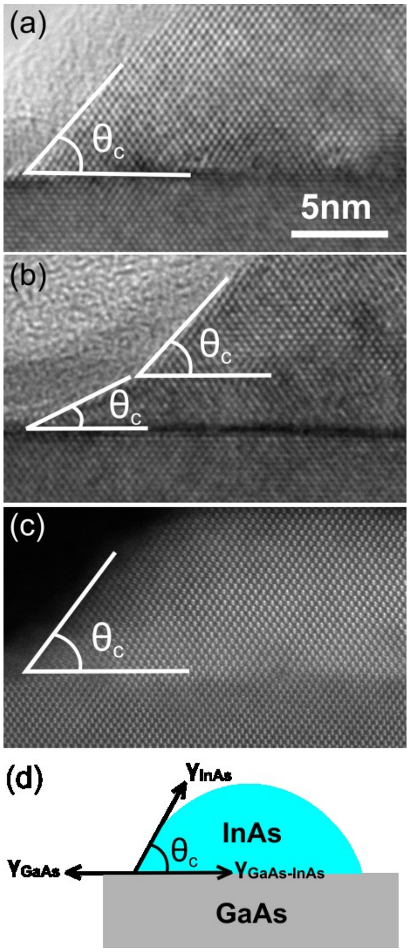

Figure 5.7 HRTEM images of crystalline InAs QDs formed by (a) SK growth mode, (b) DE with 5.5 ML In exposure, and (c) DE with 7.5 ML In exposure. θ_c indicate QD contact angles. (d) Schematic illustration of the contact angle of a QD showing the balance of the surface energies and the interfacial energy between the QD and the buffer layer.

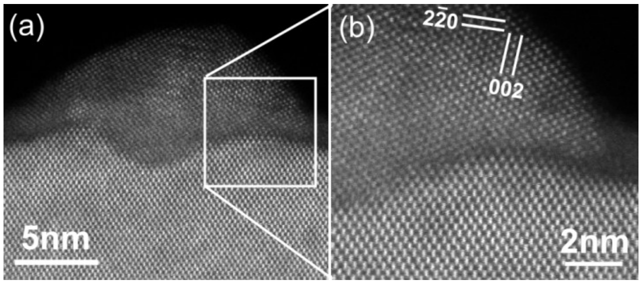

Figure 5.8 (a) High resolution scanning TEM image of a polycrystalline In_2O_3 island (5ML In exposure), with a higher magnification view of the island/buffer interface shown in (b).

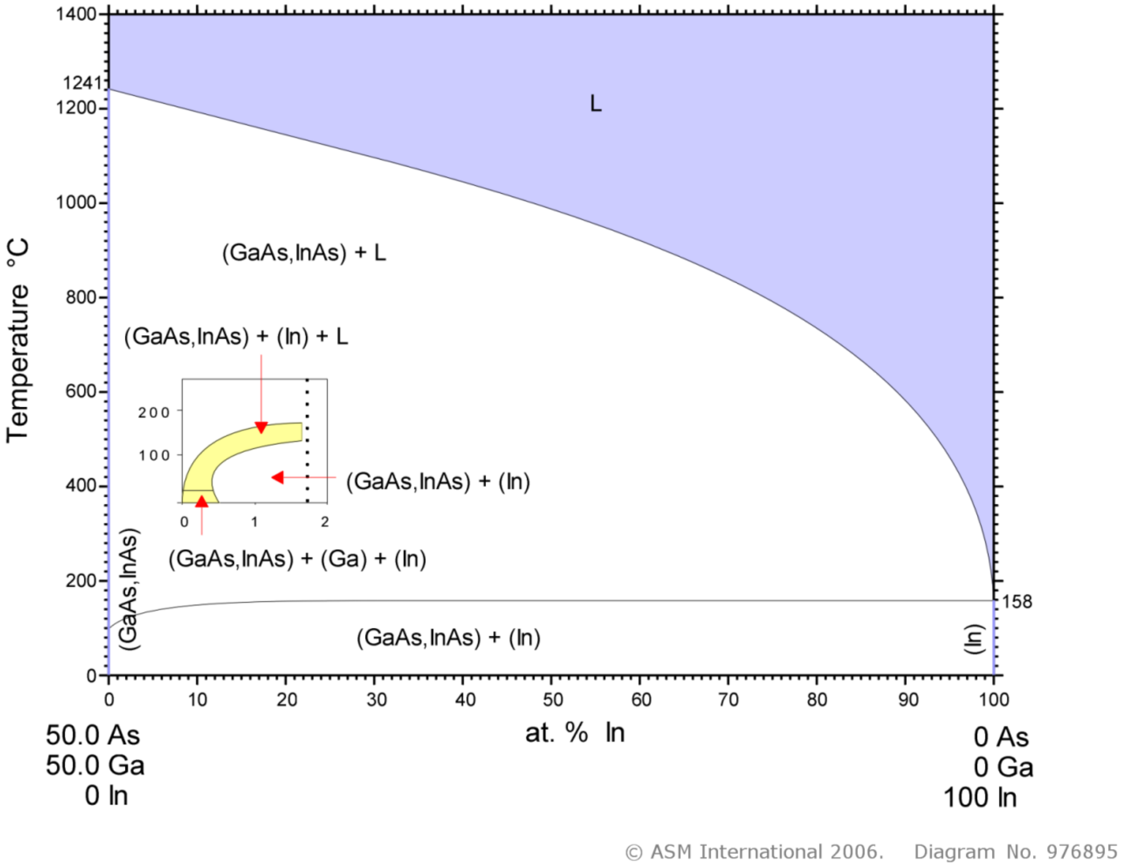

Figure 5.9 In-GaAs phase diagram. Inset shows a higher magnification view of the phase diagram in the range of 0-300˚C and 0-2 at. % In. Reprinted with permission from Ref. 36. (Copyright 2006, ASM International).

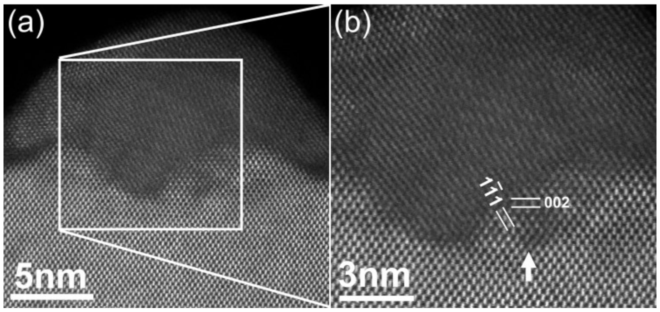

Figure 5.10 (a) High resolution scanning TEM image of a polycrystalline In_2O_3 island (5ML In exposure). (b) A higher magnification view of the In_2O_3 island at the island/buffer interface with a small portion of island converted to InAs. The vertical arrow indicates the misfit dislocation at the InAs/GaAs buffer interface.

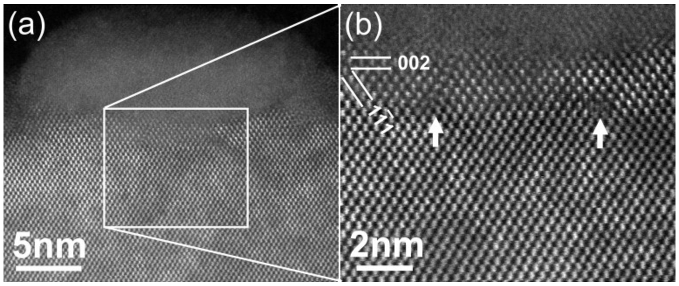

Figure 5.11 (a) High resolution scanning TEM image of a polycrystalline In_2O_3 island (8ML In exposure). (b) A higher magnification view of the In_2O_3 island with an InAs interlayer between the island/buffer interface. Vertical arrows indicate the misfit dislocations at the interlayer/buffer interface.

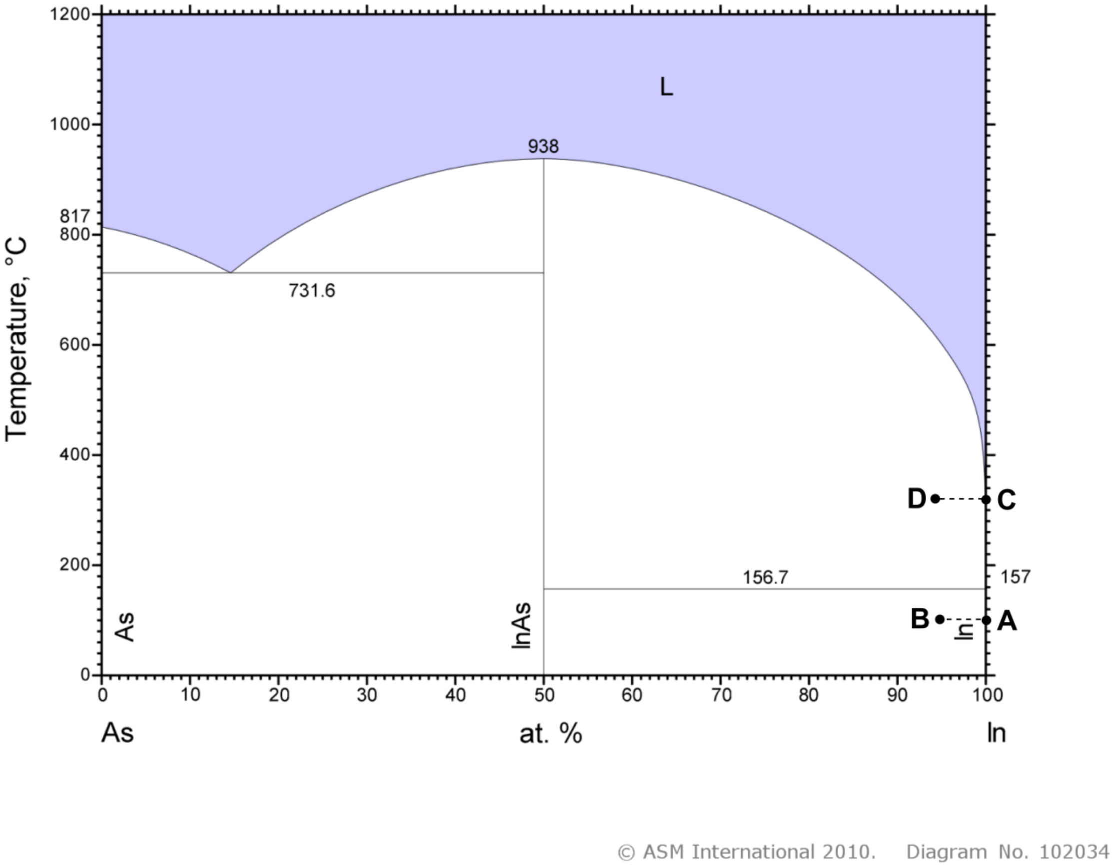

Figure 5.12 In-As phase diagram. Reprinted with permission from Ref. 39 (Copyright 2010, ASM International).

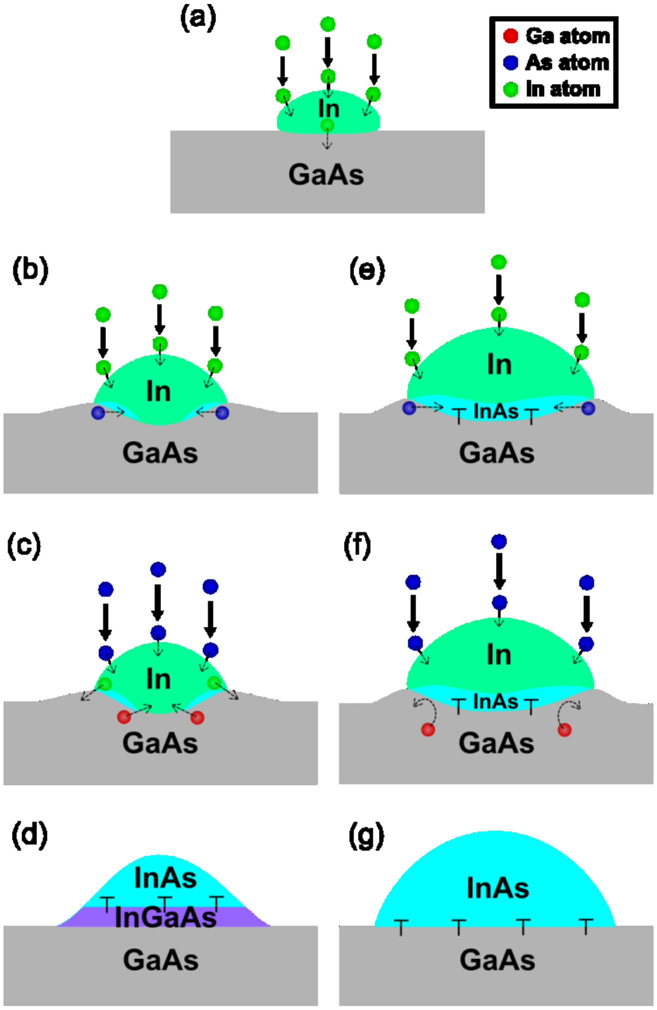

Figure 5.13 Schematic illustration for the conversion of a In island to a InAs QD via droplet epitaxy: (a) In deposition leads to island formation and In-induced nano-drilling into GaAs buffer layer. For low In exposure, (b) formation of In island with a concave up region at island/buffer interface, (c) As annealing leads to intermixing of In and Ga atoms, and diffusion of As atoms from the As flux into In island, and (d) formation of InAs QD with an intermixed InGaAs layer at the QD/buffer interface, leading to MD nucleation at the interface between the QD and the intermixed layer. For high In exposure, (e) formation of In island with an InAs interlayer at the island/buffer interface, (f) diffusion of As atoms into In island upon annealing under As flux, leading to (g) formation of InAs QDs with MDs at the QD/buffer interface.

5.9 References

---

[1] F. K. LeGoues, M. C. Reuter, J. Tersoff, M. Hammar, and R. M. Tromp, Phys. Rev. Lett. 73, 300 (1994).

[2] K. Tillmann, D. Gerthsen, P. Pfundstein, A. Förster, and K. Urban, J. Appl. Phys. 78, 3824 (1995).

[3] A. Marti, L. Cuadra, and A. Luque, in *Conference Record of the Twenty-Eighth Ieee Photovoltaic Specialists Conference - 2000* (IEEE, New York, 2000), pp. 940-943.

[4] A. Marti, E. Antolin, C. R. Stanley, C. D. Farmer, N. Lopez, P. Diaz, E. Canovas, P. G. Linares, and A. Luque, Phys. Rev. Lett. 97, 247701 (2006).

[5] S. Huang, A. V. Semichaevsky, L. Webster, H. T. Johnson, and R. S. Goldman, J. Appl. Phys. 110, 073105 (2011).

[6] D. L. Huffaker, G. Park, Z. Zou, O. B. Shchekin, and D. G. Deppe, Appl. Phys. Lett. 73, 2564 (1998).

[7] J. Phillips, K. Kamath, and P. Bhattacharya, Appl. Phys. Lett. 72, 2020 (1998).

[8] N. M. Park, T. S. Kim, and S. J. Park, Appl. Phys. Lett. 78, 2575 (2001).

[9] J. X. Chen, A. Markus, A. Fiore, U. Oesterle, R. P. Stanley, J. F. Carlin, R. Houdre, M. Ilegems, L. Lazzarini, L. Nasi, M. T. Todaro, E. Piscopiello, R. Cingolani, M. Catalano, J. Katcki, and J. Ratajczak, J. Appl. Phys. 91, 6710 (2002).

[10] A. Trampert, E. Tournié, and K. H. Ploog, Appl. Phys. Lett. 66, 2265 (1995).

[11] Y. Chen, X. W. Lin, Z. Liliental-Weber, J. Washburn, J. F. Klem, and J. Y. Tsao, Appl. Phys. Lett. 68, 111 (1996).

[12] K. Tillmann and A. Förster, Thin Solid Films 368, 93-104 (2000).

---

[13] S. Shusterman, A. Raizman, A. Sher, A. Schwarzman, O. Azriel, A. Boag, Y. Rosenwaks, P. L. Galindo, and Y. Paltiel, Europhys. Lett. 88, 66003 (2009).

[14] G. Balakrishnan, J. Tatebayashi, A. Khoshakhlagh, S. H. Huang, A. Jallipalli, L. R. Dawson, and D. L. Huffaker, Appl. Phys. Lett. 89, 161104 (2006).

[15] Y. H. Kim, J. Y. Lee, Y. G. Noh, M. D. Kim, and J. E. Oh, Appl. Phys. Lett. 90, 241915 (2007).

[16] Z. B. Chen, W. Lei, B. Chen, Y. B. Wang, X. Z. Liao, H. Tan, J. Zou, S. Ringer, and C. Jagadish, Nanoscale Res. Lett. 7, 486 (2012).

[17] K. H. Chang, P. K. Bhattacharya, and R. Gibala, J. Appl. Phys. 66, 2993 (1989).

[18] The plastic relaxation of misfit strain can be estimated from the MD spacing as follows: $f = d_{f,110} / S_{110}$, where S_{110} is the MD spacing along [110], $d_{f,110}$ is the {110} interplanar spacing for the film, and f is the film/substrate lattice misfit.

[19] M. J. Hytch, E. Snoeck, and R. Kilaas, Ultramicroscopy 74, 131-146 (1998).

[20] See Appendix A for detailed description of the geometric phase analysis.

[21] The lattice misfit between the InAs and InGaAs layers can be estimated as follows: $f = (a_{InAs} - a_{InGaAs})/a_{InGaAs}$, where a_{InAs} and a_{InGaAs} is the lattice constant of InAs and InGaAs layer, respectively.

[22] I. V. Markov, *Crystal Growth for Beginners: Fundamentals of Nucleation, Crystal Growth and Epitaxy*. (World Scientific, 2003).

[23] The constant B in the elastic strain approximation can be expressed as follows: $B = 2\mu_f \times (1 + \upsilon)/(1 - \upsilon)$, where μ_f is the shear modulus, and υ is the Poisson's ratio of the layer.

---

[24] K.-N. Tu, J. W. Mayer, and L. C. Feldman, *Electronic Thin Film Science: For Electrical Engineers and Materials Scientists*. (Macmillan, 1992).

[25] The interfacial energy between the InAs QD and the GaAs buffer layer, $\gamma^{*}_{\text{GaAs-InAs}}$, can be estimated using Young's equation as follows: $\gamma_{\text{GaAs}} = \gamma^{*}_{\text{GaAs-InAs}} + \gamma_{\text{InAs}}\times\cos\theta_c$, where γ_{GaAs} and γ_{InAs} are the surface energies of GaAs and InAs, respectively, and θ_c is the QD contact angle.

[26] E. Placidi, F. Arciprete, R. Magri, M. Rosini, A. Vinattieri, L. Cavigli, M. Gurioli, E. Giovine, L. Persichetti, M. Fanfoni, F. Patella, and A. Balzarotti, in *Self-Assembly of Nanostructures*, edited by S. Bellucci (Springer New York, 2012), Vol. 12, pp. 73-125.

[27] M. J. Beck, A. van de Walle, and M. Asta, Phys. Rev. B 70, 205337 (2004)

[28] O. Bierwagen, and J. S. Speck, Phys. Status Solidi A 211, 48-53 (2014).

[29] J. Kim, H. Schoeller, J. Cho, and S. Park, J. Electron. Mater. 37, 483-489 (2008).

[30] W. Ye, S. Hanson, M. Reason, X. Weng, and R. S. Goldman, J. Vac. Sci. Technol. B 23, 1736-1740 (2005).

[31] Z. M. Wang, B. L. Liang, K. A. Sablon, and G. J. Salamo, Appl. Phys. Lett. 90, 113120 (2007).

[32] A. Stemmann, C. Heyn, T. Koeppen, T. Kipp, and W. Hansen, Appl. Phys. Lett. 93 123108 (2008).

[33] D. P. Kumah, S. Shusterman, Y. Paltiel, Y. Yacoby, and R. Clarke, Nature Nanotech. 4, 835-838 (2009).

---

[34] C. Somaschini, S. Bietti, N. Koguchi, and S. Sanguinetti, Nano Letters 9, 3419-3424 (2009).

[35] T. Noda, T. Mano, M. Jo, T. Kawazu, and H. Sakaki, J. Appl. Phys. 112, 063510 (2012).

[36] G.M. Kuznetsov, V.N. Fedorov, D.U. Smagulov, S.K. Kuznetsova, A.L. Rodnyanskaya, and S.M. Banova, In-GaAs Phase Diagram, ASM Alloy Phase Diagrams Database, P. Villars, editor-in-chief; H. Okamoto and K. Cenzual, section editors; http://www1.asminternational.org.proxy.lib.umich.edu/AsmEnterprise/APD, ASM International, Materials Park, OH, 2006.

[37] The molar volume of In (In_2O_3) equals to 15.7 (38.0) cm^3, which leads to ~21 % volume expansion following the oxidation of the In islands.

[38] R. K. Akchurin, I. A. Boginskaya, A. A. Marmalyuk, M. A. Ladugin, and M. A. Surnina, Russ. Microelectron. 41, 453-458 (2012).

[39] I. Ansara, C. Chatillon Colinet, H.L. Lukas, T. Nishizawa, H. Ohtani, K. Ishida, M. Hillert, B. Sundman, B.B. Argent, A. Watson, T.G. Chart, and T.A. Anderson, In-As Phase Diagram, ASM Alloy Phase Diagrams Database, P. Villars, editor-in-chief; H. Okamoto and K. Cenzual, section editors; http://www1.asminternational.org.proxy.lib.umich.edu/AsmEnterprise/APD, ASM International, Materials Park, OH, 2010.

[40] N. A. Bert, V. V. Chaldyshev, Y. G. Musikhin, A. A. Suvorova, V. V. Preobrazhenskii, M. A. Putyato, B. R. Semyagin, and P. Werner, Appl. Phys. Lett. 74, 1442 (1999).

Chapter 6

Summary and Suggestions for Future Work

6.1 Summary

In this thesis, the photovoltaic properties of solar cells based on the conventional SK QDs and the formation mechanisms and microstructures of InAs QDs formed by annealing In islands in an As flux were studied. We investigated the influence of WLs and QD size variation on the sub-bandgap EQE of QD solar cells. We examined the role of As surface coverage on the mechanism of QD formation. The origins of MD displacement and interlayer formation in the vicinity of QDs were also investigated. This thesis reveals new insights into the design of QD heterostructures for various optoelectronic applications. Based on these results, it is suggested that DE approach is promising for tuning QD size and density, as well as tailoring carrier confinement in the vicinity of QDs.

In Chapter 3, we present our investigation of the influence of WLs and QD size distribution on the sub-bandgap EQE of QD solar cells. We use a finite-element Schrödinger-Poisson model that considers QD and WL shapes, sizes, and spacings from XSTM and AFM. A comparison between experiment and theory reveals a broadening of sub-bandgap EQE induced by QD size vertical variation and a weak EQE contribution from the WLs. The unique combination of experiment and computation may be used as a guide for designing QD SLs for various optoelectronic device applications.

In Chapter 4, we report on our investigations of the formation mechanisms of In islands and their conversion to InAs QDs via annealing in an As flux. The QD formation follows either the DE or SPE mechanism, depending on As surface coverage. On c(4x4) GaAs surfaces, QDs form by DE, in which case one-to-one conversion from In islands to InAs QDs occurs on c(4x4)α. For c(4x4)β, enhanced In surface diffusion leads to lower densities of larger QDs. For the As capped surface, QDs nucleate by SPE during annealing of an amorphous film in an As flux. These mechanisms are likely to be applicable to a wide variety of compound semiconductors.

In Chapter 5, we consider the influence of growth mode on MD displacement and interlayer formation in the vicinity of InAs/GaAs QDs. For SK QDs, regularly-spaced MDs nucleate at the QD/buffer interface. For DE, during In deposition, both In island formation and In-induced "nano-drilling" of the GaAs buffer layer are observed. For low In exposure, the In islands are converted to InAs QDs upon annealing under As flux, with an InGaAs interlayer at the QD/buffer interface. Meanwhile, MDs nucleate at the QD/interlayer interface. For high In exposure, an InAs interlayer forms at the island/buffer interface during the In deposition step. Annealing in an As flux leads to the conversion of In islands to InAs QDs, resulting in MDs at the QD/buffer interface. By varying the amount of In exposure during DE, we demonstrate the formation of InAs QDs with MDs either at or above the QD/buffer interface. The DE approach enables the control of MD vertical displacement during QD formation, which is promising for tailoring carrier confinement in the vicinity of QDs.

6.2 Suggestions for Future Work

6.2.1 Overview

In Chapters 3-5, we presented our investigations of the photovoltaic properties of solar cells based on the conventional SK QDs, and we also discussed the formation mechanisms and microstructures of InAs QDs formed by annealing In islands under an As flux. The new insights revealed by these studies have motivated further investigations into new methods for enabling more flexible tuning of QD sizes, densities, materials combinations, and electronic structures. In the following sections, we will discuss the preliminary results and specific suggestions for these new topics. First, we will discuss photoluminescence of the InAs/GaAs QDs formed by the SK and DE growth modes. Subsequently, we will discuss a new approach extending DE of InAs QDs to the AlGaAs surface. Then, we will present a unique process of focused-ion-beam assisted DE of QDs. Finally, we will present a combined experimental-computational approach for studying the influence of surface nanopatterning on QD formation.

6.2.2 Photoluminescence of InAs/GaAs Quantum Dots

In Chapter 5, HRTEM was used to study the microstructure of QDs, revealing interlayer formation and MD vertical displacement, which is promising for tailoring carrier confinement in the vicinity of QDs. To investigate the QD electronic structure, an experimental technique capable of accessing the QD energy levels is essential. For example, a photoluminescence (PL) measurement involves the use of an external light source to excite charge carriers to higher energy states, followed by the observation of light emission from radiative recombination of carriers. The energies of the emitted light are associated with the optical transitions between the available energy states, providing a way to probe the energy levels associated with the QDs.

For the PL studies of the InAs QDs, we fabricated the QD samples as follows: The InAs QDs were grown on epiready GaAs (001) substrates by MBE, using solid Ga, As_2, and In sources. Details of the QD and GaAs buffer layer growth are described in Chapter 4. Following the formation of the InAs QDs, 100 nm of GaAs capping layer was grown at 400 °C, with a growth rate of 0.1 μm/hr. For PL measurements, the QD samples were mounted in a helium flow cryostat operating at 10 K and optically excited with a 633 nm continuous wave (CW) Helium-Neon laser. Pump powers varied from 0.06 to 645 μW. The incident laser beam was focused to a 10 μm diameter spot on the sample. PL was recorded using a 150 G/mm reflection grating in a 0.75 m spectrometer and a liquid nitrogen cooled Si CCD detector. Figure 6.1 shows power-dependent PL spectra of InAs/GaAs QDs formed by (a) DE and (b) SK growth mode. In both cases, peaks from GaAs band-to-band and donor-acceptor recombination are observed at ~1.51 and 1.49 eV, respectively. In addition, the peak observed at ~1.46 eV can be attributed to the WL. Both PL spectra exhibit a broad peak at ~1.3 – 1.4 eV, presumably associated with emissions from the QDs with broad size distributions. The QD peak blue-shifts as the excitation power increases, which can be attributed to emissions from QD excited states.[1] Furthermore, stronger QD emissions (relative to the GaAs emissions) are observed in

Figure 6.1(b), presumably due to a higher density of the SK QDs compared to that of the DE QDs.

From these PL measurements, the QD peaks are too broad to show any distinct difference between the SK and DE QDs. To date, several groups have also investigated into the PL response of DE QDs. In particular, Kim *et al.* observed room temperature PL peaked at 1.14 eV from InAs QDs formed by DE.[2] Sanguinetti *et al.* studied the temperature dependent PL of InGaAs DE QDs and observed a less significant temperature-induced red-shift of the PL peak energy than that of the SK QDs.[3] In addition, Cohen *et al.* examined the PL response of InAs DE QDs grown by metallorganic vapor phase epitaxy (MOVPE) and observed a broad PL peak associated with the QDs, centered at ~1 eV. So far, a direct comparison between the structural and optical properties of the DE and SK QDs is still lacking. Therefore, for future work, minimizing any peak broadening effects associated with QD size and density variations is necessary for a fair comparison between the PL responses from the DE and SK QDs. One suggestion is to develop growth of DE and SK QDs with similar sizes and densities for the PL measurements. Another suggestion is to fabricate ultra-low density QDs for enabling PL measurements of individual QDs. That way, a direct comparison between the PL responses from individual QDs can be achieved.

6.2.3 Droplet Epitaxy of InAs QDs on AlGaAs

As discussed in Chapter 1, semiconductor QDs have been proposed to introduce the intermediate bands needed for the IBSC concept.[4,5,6] To date, InAs/GaAs QD SLs have been widely considered for IBSC devices.[7,8,9,10,11,12,13,14,15] However, the relatively small conduction band offset in the InAs/GaAs system enables significant carrier escape, leading to a reduced effective bandgap and lower V_{OC}. To increase the carrier lifetimes and reduce thermal escape rates, an alternative matrix material with higher bandgap and larger band offset is desired. AlGaAs, which has a ~50% larger bandgap than that of GaAs, has been proposed as a promising matrix material for IBSC based on InAs QDs. Indeed, a high photocurrent with voltage preservation has been predicted for IBSC devices consisting of InAs/AlGaAs QD SLs.[16,17] Furthermore, suppression of the carrier escape has also been demonstrated in the InAs/AlGaAs QD solar cells.[18] As we described in Chapter 4, the DE approach allows the fabrication of InAs QDs with a broad range of sizes and densities. Therefore, DE of InAs/AlGaAs QDs is promising for achieving high densities of ultra-small QDs for IBSC devices with longer carrier lifetimes and lower thermal escape rates.

To date, we have identified suitable conditions for growing In islands on AlGaAs buffer layers as follows: The In islands and the AlGaAs buffer layer were grown on epiready GaAs (001) substrates by Riber Compact 21 MBE, using solid Ga, Al, As_2, and In sources. Each sample contained an initial 300 nm thick GaAs buffer layer grown at 580 °C with a growth rate of 1 μm/hr and a V/III BEP ratio of ~16. Next, 50 nm of AlGaAs layer was grown at 620 °C, with a growth rate of 1 μm/hr and a V/III BEP ratio of ~16. For the In islands, the T_S was then decreased to 300 °C, at which point the As shutter was closed, and the growth chamber background pressure gradually dropped to < 2.5×10^{-9} Torr. Finally, the T_S was decreased to 80 °C, and 5.4 ML In was deposited with a rate of 0.1 ML/s. Figure 6.2 shows AFM images of (a) AlGaAs buffer layer with RMS roughness of 0.4 nm and (b) In islands with density (diameter) of $\sim 1.2 \times 10^{10}$ cm^{-2} (~37 nm) on the AlGaAs buffer surface. Suggested future work includes the development of proper annealing conditions for the conversion of In islands to InAs QDs, where the influence of annealing temperature and As flux needs to be carefully considered to inhibit QD coarsening during the annealing step. In addition, further investigation into the effects of substrate temperature, growth rate, and V-III ratio of the AlGaAs capping/spacer layers is necessary to avoid the disintegration of QDs during multi-layer growth of the InAs/AlGaAs QD SLs.

6.2.4 Focused-ion-beam Assisted Droplet Epitaxy of QDs

In Chapter 1, we discussed several self-assembled QD fabrication approaches, including the misfit-driven SK growth and the DE approach. In Chapter 4 and Chapter 5, we demonstrated that the DE approach is promising for tuning QD size and density, as well as tailoring carrier confinement in the vicinity of QDs. However, these self-assembled approaches typically result in randomly distributed QDs with size variations. Recently, various approaches have been developed for enhancing the size uniformity and ordering of the self-assembled QDs. For example, Akahane *et al.* demonstrated ordered array of $In_{0.4}Ga_{0.6}As$ QDs using GaAs (311)B substrates.[19] In addition, Guimard *et al.* reported suppressed coalescence of InAs QDs with density exceeding 4×10^{10} cm^{-2} using antimony as a surfactant during GaAs buffer layer growth.[20] Besides, Kim *et al.* showed an improved QD size homogeneity with an In-stabilized (rather than As-stabilized) GaAs buffer surface.[21]

To further improve the ordering, density, and uniformity of QDs for higher efficiency energy conversion devices, we propose a unique nanofabrication approach, focused-ion-beam (FIB) assisted DE. In this approach, In nanodroplets formed via FIB scanning are subsequently converted to InAs QDs via exposure to an arsenic flux in MBE. In particular, a thin layer of InAs will be grown on the GaAs surface, as depicted in Figure 6.3(a). Subsequently, off-normal FIB irradiation over the entire area then leads to the formation of ordered In nanodroplets, as shown in Figure 6.3(b). Off-normal FIB irradiation at various angles and ion doses will be used to tailor the sizes, spacings, and arrangements of nanodroplets. Figure 6.4 shows AFM images of ordered In nanodroplets fabricated via 52° off-normal FIB irradiation on InAs substrate. As the ion dose is increased from 8.8×10^{17} to 3.5×10^{18} cm^{-2}, the nanodroplet density increases from 1.6×10^{10} to 2.6×10^{10} cm^{-2}, revealing a positive ion dose dependence of the nanodroplet density. Finally, exposure to an arsenic flux enables the conversion of In nanodroplets to InAs QDs, as shown in Figure 6.3(c). The film growth, FIB irradiation, and arsenic exposure sequence will then be repeated to achieve multi-stacks of InAs/GaAs QD superlattices, as depicted in Figure 6.3(d). Since the DE method is not strain driven, high densities of ultra-small spherical-like QDs are achievable, independent of the misfit strain between film and substrate. The ultra-small spherical-like QDs will reduce the number of confined energy levels in the band offset to ensure more efficient carrier extraction.

6.2.5 Influence of Surface Nanopatterning on InAs/GaAs Quantum Dot Formation

The control of lateral ordering of self-assembled QDs is challenging to achieve; however, it is highly desirable for various solid-state applications, including solar cells lasers, and telecom devices.[22,23,24,25] To date, lateral alignment of QDs has been demonstrated for multilayer of QDs.[26,27,28] In these cases, the first layer of QDs are distributed isotropically; subsequently, the lateral alignment of QDs develops during growth of QD stacks, which has been attributed to anisotropic strain field accumulated during QD stacking.[26,27,28] However, the correlation between the buffer layer surface morphology and the nucleation of QDs is still unclear. In this work, we use a combined experimental-computational method to directly examine the correlation between GaAs buffer surface morphology and InAs QD nucleation, revealing preferential nucleation of QDs at "mound" edges and early onset of QD nucleation induced by mounds.

The InAs QDs and GaAs buffer layers were grown on epiready GaAs (001) substrates by MBE, using solid Ga, As_4, and In sources. Details of the QD and GaAs buffer layer growth are described in Ref. 27. The surface morphology of the GaAs buffer layers and the InAs QDs was examined *ex-situ* with tapping mode AFM, using etched Si probes. The nucleation of InAs QDs on GaAs surface is simulated using a phase-field model (simulation done by Larry Aagesen in Thornton group at University of Michigan), which is described in detail in Appendix C.

We first describe the surface morphology of the GaAs buffer layers and InAs/GaAs QDs. Figure 6.5 shows AFM images of (a) flat GaAs buffer surface with bilayer height step-terrace arrays (buffer HL) and (b) rough GaAs buffer surface with "mound" features above the step-terrace array background (buffer L). Figure 6.5 (c) and (d) show AFM images of InAs QDs grown on buffer HL and L, respectively. For QDs grown on buffer HL (buffer L), the QD density and mean diameter are ~3.8×10^{10} cm^{-2} and 20 nm (~6.0×10^{10} cm^{-2} and 18 nm), respectively. Apparently, the density of the QDs on buffer L is significantly higher than that of the QDs on buffer HL, indicating a positive correlation between the presence of mounds and the nucleation of QDs.

To investigate the influence of the mounds on QD nucleation, we simulate QD growth using the line-cut profiles from the AFM images of buffer HL and L as initial conditions. Figure 6.6 shows the AFM images of (a) buffer HL and (b) buffer L with the height profile of each red line extracted as the plots of height vs. distance, shown beneath each image. The simulated QD growths on buffer HL and L are shown below each line-cut profile. For the QD simulation on buffer HL, the QD nucleation sites do not appear to be correlated with the surface topography. For the QD simulation on buffer L, preferential QD nucleation at the edge of the mounds is apparent, as indicated by the vertical dashed lines in Figure 6.6 (b). The comparison between the simulated QD growths on these two buffers reveals essentially isotropic QD nucleation on buffer HL and preferential QD nucleation at mound edges on buffer L.

To quantify whether InAs prefers to nucleate on buffer surface with a positive (concave-up) or negative (concave-down) curvature, we plot the local InAs layer height as a function of local GaAs surface curvature, as shown in Figure 6.7(a) and Figure 6.8(a) for buffer HL and L, respectively. In both Figure 6.7(a) and Figure 6.8(a), a positive slope is identified, suggesting preferential InAs nucleation at positive curvature regions. To quantify the time evolution of local InAs height at different curvature ranges, we plot the local InAs height as a function of time for four (eight) curvature ranges from -0.01 to 0.01 (-0.02 to 0.02) nm^{-1} for buffer HL and L, as shown in Figure 6.7 (b) and Figure 6.8 (b), respectively. For both buffer HL and L, InAs transferring from negative curvature regions (hills) to positive curvature regions (valleys) following onset of QD nucleation is apparent. Furthermore, the comparison between Figure 6.7 (b) and Figure 6.8 (b) reveals an earlier (later) onset of QD nucleation on buffer L (buffer HL) at simulation time ~50 (~58) [arb. time unit], suggesting that the presence of mounds induce the nucleation of QDs.

This unique combination of experiments and simulation provides new insight into the correlation between buffer surface morphology and formation of semiconductor nanostructures. A suggested future work is to apply this combined experimental-computational approach to different buffer materials, such as AlGaAs or GaN. Furthermore, the phase field model might be extended to consider selective nucleation of QDs, which is promising for achieving high density of linear QD chains on one side of the mounds.[29]

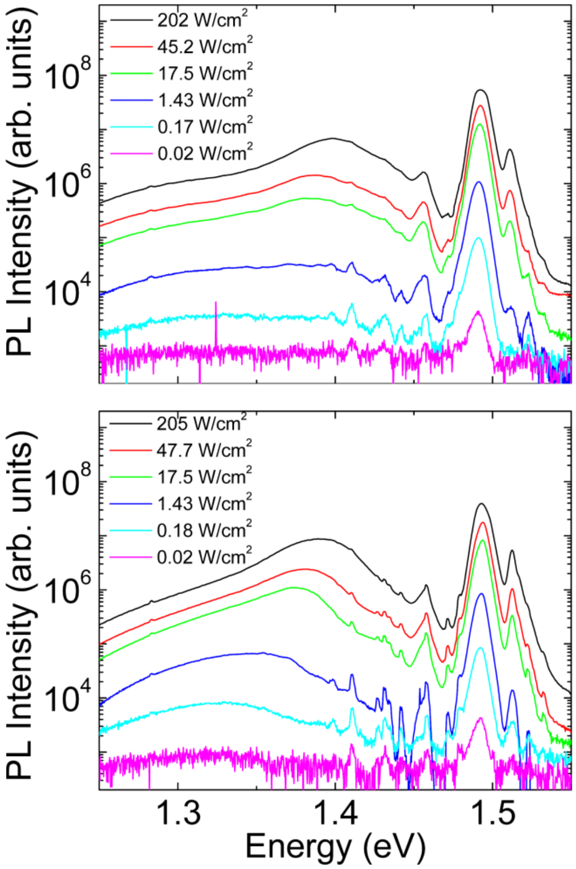

Figure 6.1 PL spectra taken at excitation power densities of 0.02 to 205 W/cm^2 from InAs/GaAs QDs formed by (a) DE and (b) SK growth mode.

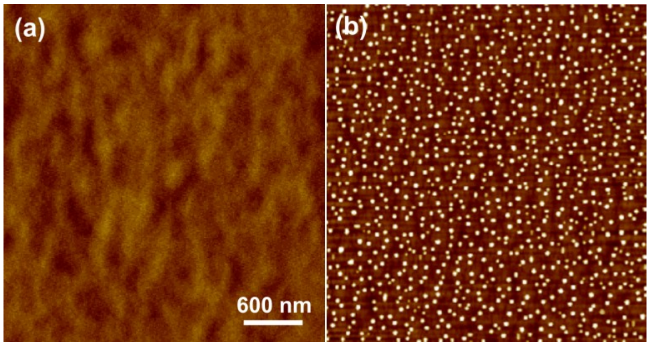

Figure 6.2 AFM images of (a) AlGaAs buffer layer with RMS roughness of 0.4 nm and (b) In islands with density (diameter) of ~1.2×10^{10} cm^{-2} (~37 nm) on the AlGaAs buffer surface.

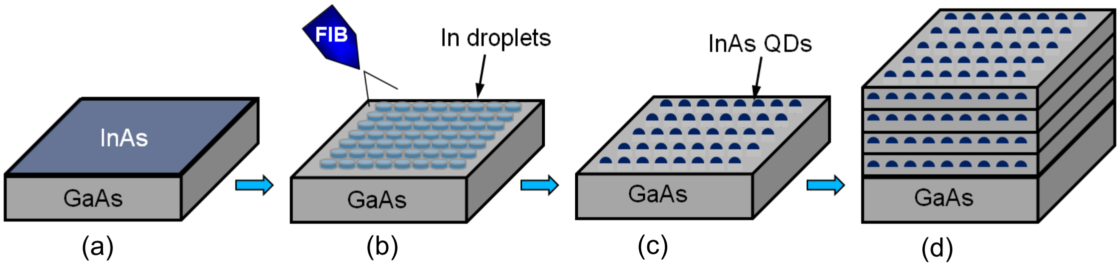

Figure 6.3 Schematic illustration of (a) Thin layer of InAs grown on GaAs. (b) Ordered nanometer-scale In droplets produced on the surface of a GaAs substrate using off-normal focused-ion-beam irradiation. (c) InAs QDs formed via exposure to an arsenic flux. (d) Multi-stacks of InAs/GaAs QD superlattices.

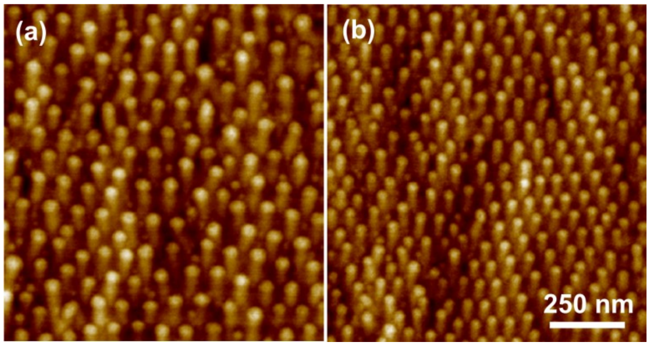

Figure 6.4 AFM images of ordered In nanodroplets fabricated via 52˚ off-normal FIB irradiation on InAs with ion dose of (a) 8.8 × 10^{17} and (b) 3.5 × 10^{18} cm^{-2}.

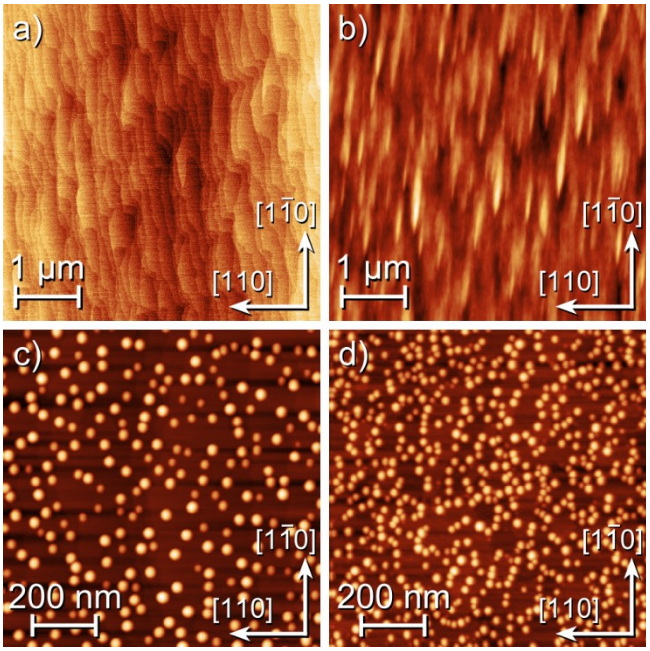

Figure 6.5 AFM images of GaAs buffers: (a) buffer HL (flat surface), (b) buffer L (surface with mounds). (c) and (d) show AFM images of InAs QDs grown on buffer HL and buffer L, respectively.

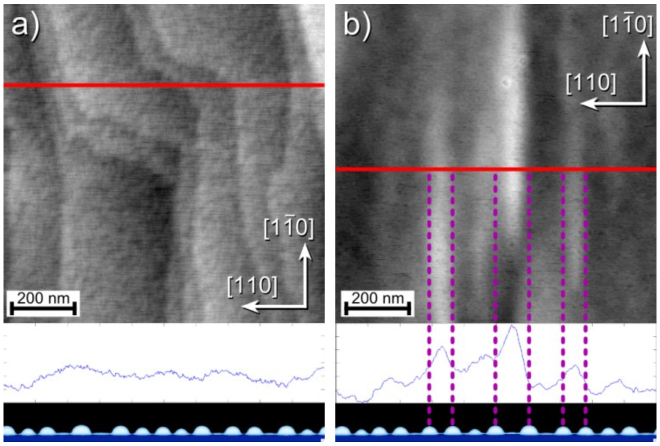

Figure 6.6 AFM images of GaAs buffers with the corresponding line-cut profiles for (a) buffer HL and (b) buffer L. The phase field simulation of InAs QDs grown on each buffer surface is shown below each line-cut profile.

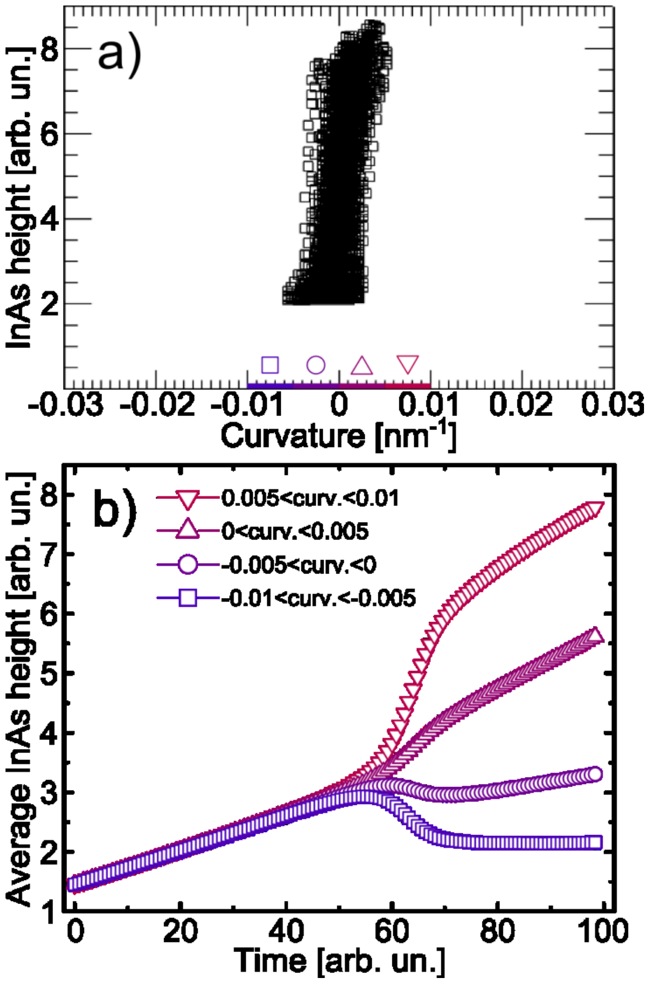

Figure 6.7 Plots of (a) the local InAs layer height as a function of local GaAs surface curvature and (b) the local InAs layer height as a function of time for four curvature ranges from -0.01 to 0.01 nm^{-1}, for InAs growth simulation on buffer HL.

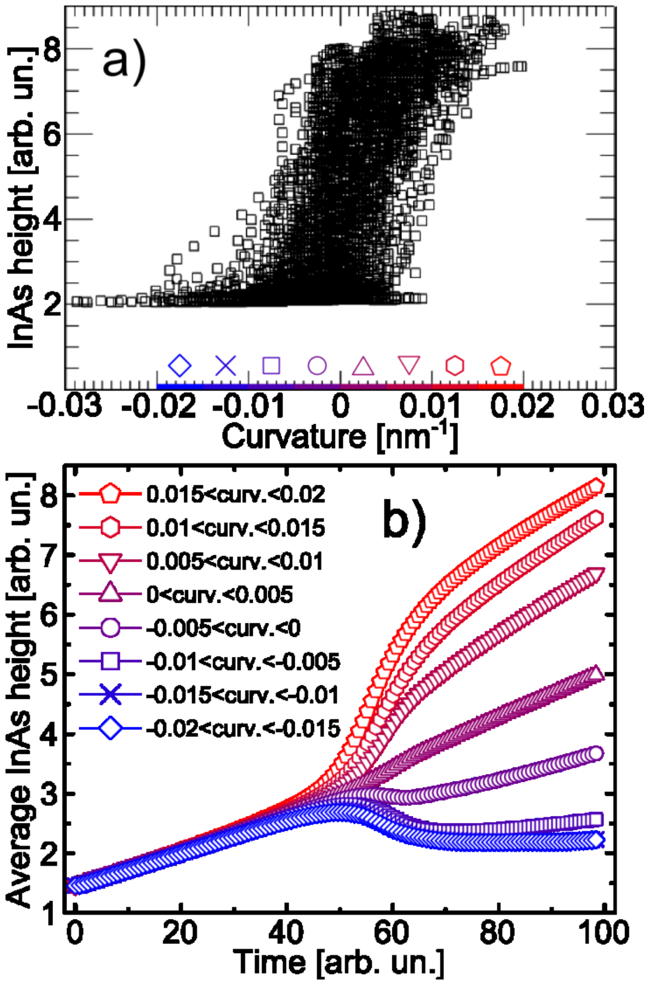

Figure 6.8 Plots of (a) the local InAs layer height as a function of local GaAs surface curvature and (b) the local InAs layer height as a function of time for eight curvature ranges from -0.02 to 0.02 nm^{-1}, for InAs growth simulation on buffer L.

6.3 References

---

[1] S. Sanguinetti, T. Mano, M. Oshima, T. Tateno, M. Wakaki, and N. Koguchi, Appl. Phys. Lett. **81**, 3067 (2002).

[2] J. S. Kim and N. Koguchi, Appl. Phys. Lett. 85, 5893 (2004).

[3] S. Sanguinetti, T. Mano, M. Oshima, T. Tateno, M. Wakaki, and N. Koguchi, Appl. Phys. Lett. **81**, 3067 (2002).

[4] R. P. Raffaelle, S. L. Castro, A. F. Hepp, and S. G. Bailey, Progress in Photovoltaics: Research and Applications **10**, 433 (2002).

[5] M. A. Green, Materials Science and Engineering: B **74**, 118 (2000).

[6] A. Marti, L. Cuadra, and A. Luque, Electron Devices, IEEE Transactions on **48**, 2394 (2001).

[7] A.J. Grenko, I. Kimukin, J. Walker, and E. Towe, *Solar Energy: New Materials and Nanostructured Devices for High Efficiency (Solar)* (Stanford University, California, 2008), p. SWA4.

[8] A. Luque, A. Martí, N. López, E. Antolín, E. Cánovas, C. Stanley and C. Farmer, L. J. Caballero, L. Cuadra, J. L. Balenzategui, Appl. Phys. Lett. **87**, 083505 (2005).

[9] S.A. Blokhin, A.V. Sakharov, A.M. Nadtochy, A S. Pauysov, M.V. Maximov, N.N. Ledentsov, A.R. Kovsh, S.S. Mikhrin, V.M. Lantratov, S.A. Mintairov, N.A. Kaluzhniy, and M.Z. Shvarts, Semiconductors **43**, 514 (2009).

[10] A.G. Norman, M.C. Hanna, P. Dippo, D.H. Levi, R.C. Reedy, J.S. Ward, and M.M. Al-Jassim, *Proceedings of the 31st IEEE Photovoltaic Specialists Conference*, Lake Buena Vista, Florida, 2005, pp.43-48.

---

[11] C.O. McPheeters, C.J. Hill, S.H. Lim, D. Derkacs, D.Z. Ting, and E.T. Yu, J. Appl. Phys. **106**, 056101 (2009).

[12] D. Alonso-Álvarez, B. Alén, J. M. García, and J. M. Ripalda, Appl. Phys. Lett. **91**, 263103 (2007).

[13] D. Zhou, G. Sharma, S. F. Thomassen, T. W. Reenaas, B. O. Fimland, Appl. Phys. Lett. **96**, 061913 (2010).

[14] R B. Laghumavarapu, A. Moscho, A. Khoshakhlagh, M. El-Emawy, L.F. Lester, D.L. Huffaker, Appl. Phys. Lett. **90**, 173125 (2007).

[15] S.M. Hubbard, C .P. Cress, C. G. Bailey, R. P. Rafaelle, S. G. Bailey, and D. M. Witt, Appl. Phys. Lett. **92**, 123512 (2008).

[16] G. Wei and S. R. Forrest, Nano Letters **7**, 218-222, (2007).

[17] P. G. Linares, A. Martí, E. Antolín, and A. Luque, J. Appl. Phys. **109**, 014313 (2011).

[18] I. Ramiro, E. Antolin, M. J. Steer, P. G. Linares, E. Hernandez, I. Artacho, E. Lopez, T. Ben, J. M. Ripalda, S. I. Molina, F. Briones, C. R. Stanley, A. Marti, and A. Luque, in 38th IEEE Photovoltaic Specialists Conference (PVSC), Texas (2012).

[19] Kouichi Akahane, Takahiro Kawamura, Kenji Okino, Hiromichi Koyama, Shen Lan, Yoshitaka Okada, Mitsuo Kawabe, and Masahiro Tosa, Appl. Phys. Lett. **73**, 3411 (1998).

[20] Denis Guimard, Masao Nishioka, Shiro Tsukamoto, and Yasuhiko Arakawa, Appl. Phys. Lett. **89**, 183124 (2006).

[21] Jungsub Kim, Changjae Yang, Uk Sim, Gun-Do Lee, Jinsub Park, Youngsoo Lee, and Euijoon Yoon, J. Appl. Phys. **110**, 044302 (2011).

---

[22] A. Luque, A. Martí, E. Antolín, and C. Tablero, Physica B: Condensed Matter **382**, 320 (2006).

[23] N. N. Ledentsov, N. Kirstaedter, M. Grundmann, D. Bimberg, V. M. Ustinov, I. V. Kochnev, P. S. Kop'ev, and Z. I. Alferov, Microelectronics Journal 28, 915 (1997).

[24] N. Sritirawisarn, F. W. M. van Otten, and R. Notzel, Journal of Physics: Conference Series **245**, 012004 (2010).

[25] D. Bimberg, M. Grundmann, N.N. Ledentsov, *Quantum Dot Heterostructures*, (Wiley, Chichester, 1998).

[26] Z. M. Wang, K. Holmes, Y. I. Mazur, and G. J. Salamo, Appl. Phys. Lett. **84**, 1931 (2004).

[27] T. Mano, R. Nötzel, G. J. Hamhuis, T. J. Eijkemans, and J. H. Wolter, J. Appl. Phys. **95**, 109 (2004).

[28] W. Ye, S. Hanson, M. Reason, X. Weng, and R. S. Goldman, J. Vac. Sci. Technol. B 23, 1736-1740 (2005).

[29] F. Arciprete, E. Placidi, R. Magri, M. Fanfoni, A. Balzarotti, and F. Patella, ACS Nano **7**, 3868 (2013).

Appendices

Appendix A

Geometric Phase Analysis of HRTEM Images

To determine the local lattice distortion in the vicinity of quantum dots (QDs), we perform geometric phase analysis (GPA) of the high resolution transmission electron microscopy (HRTEM) image, as shown in Figure A.1(a).[1] First, we calculate the power spectrum of the fast Fourier transformation (FFT) of the HRTEM image, as shown in Figure A.1(b). For both GaAs and InAs, we select the spots corresponding to the 002 and $1\bar{1}1$ reciprocal lattice points, g_{002} and $g_{1\bar{1}1}$, choosing GaAs as the reference lattice. Inverse FFTs are then performed to produce the intensity and phase components of the 002 and $1\bar{1}1$ Fourier filtered images, shown in Figure A.2(a) – (d). In Figure A.2(a) and (b), the intensities of the 002 and $1\bar{1}1$ inverse FFTs, lattice fringes along the [002] and $[1\bar{1}1]$ direction are evident. In Figure A.2(c) and (d), the phase images of the 002 and $1\bar{1}1$ inverse FFTs, the 002 and $1\bar{1}1$ lattice distortions with respect to the reference GaAs lattice are evident. To determine the in-plane, $[1\bar{1}0]$, and out-of-plane, [001], components of the displacement field, the appropriate linear combinations of the phase images are computed as follows.[1] From the relationship between the phase, P_g, and the displacement field, u,

$$P_g = -2\pi g \cdot u, \tag{A.1}$$

we can write the following equations for $g_1 = g_{1\bar{1}1}$ and $g_2 = g_{002}$:

$$P_{g_1} = -2\pi\left[g_{1_x}u_x + g_{1_z}u_z\right], \tag{A.2}$$

$$P_{g_2} = -2\pi\left[g_{2_x}u_x + g_{2_z}u_z\right], \tag{A.3}$$

where u_x and u_z are the in-plane, $[1\bar{1}0]$, and out-of-plane, [001], components of the displacement field. Similarly, g_{1_x} and g_{1_z} are the in-plane and out-of-plane components of g_1 (same for g_2). Solving Eqns. (A.2) and (A.3), we obtain the following expressions for u_x and u_z:

$$u_x = -\frac{1}{4\sqrt{2}\pi}\left(2P_{g_1} - P_{g_2}\right), \tag{A.4}$$

$$u_z = -\frac{1}{4\pi}P_{g_2} \; . \tag{A.5}$$

The resulting u_x and u_z are shown in Figure A.3(a) and (b). We then calculate the in-plane (out-of-plane) lattice distortions as the derivatives of the in-plane (out-of-plane) components of the displacement field, shown in Figure A.4(a) [(b)]. Both the in-plane and out-of-plane lattice distortion maps reveal ~7 % distortion within the InAs QD, consistent with the larger lattice spacings of fully relaxed InAs (~7 %) compared to that of the GaAs. In addition, the in-plane lattice distortion map reveals local maxima at the QD/buffer interface, which correspond to the locations of the interfacial misfit dislocations (MDs). The MD-induced local maxima are not evident in the out-of-plane lattice distortion map, since the InAs (GaAs) lattices are stretched (compressed) only in the in-plane direction.

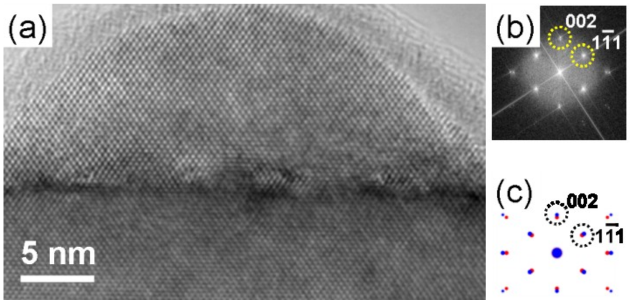

Figure A.1 High resolution transmission electron microscopy (HRTEM) image of (a) a crystalline InAs quantum dot (QD) formed by Stranski-Krastanov (SK) mode. The corresponding power spectrum of the fast Fourier transformation (FFT) is shown in (b), where the spots selected for geometric phase analysis (GPA) (circled with dashed lines) correspond to the 002 and $1\bar{1}1$ reflections, as indicated in the simulated diffraction patterns from both InAs (red) and GaAs (blue) shown in (c).

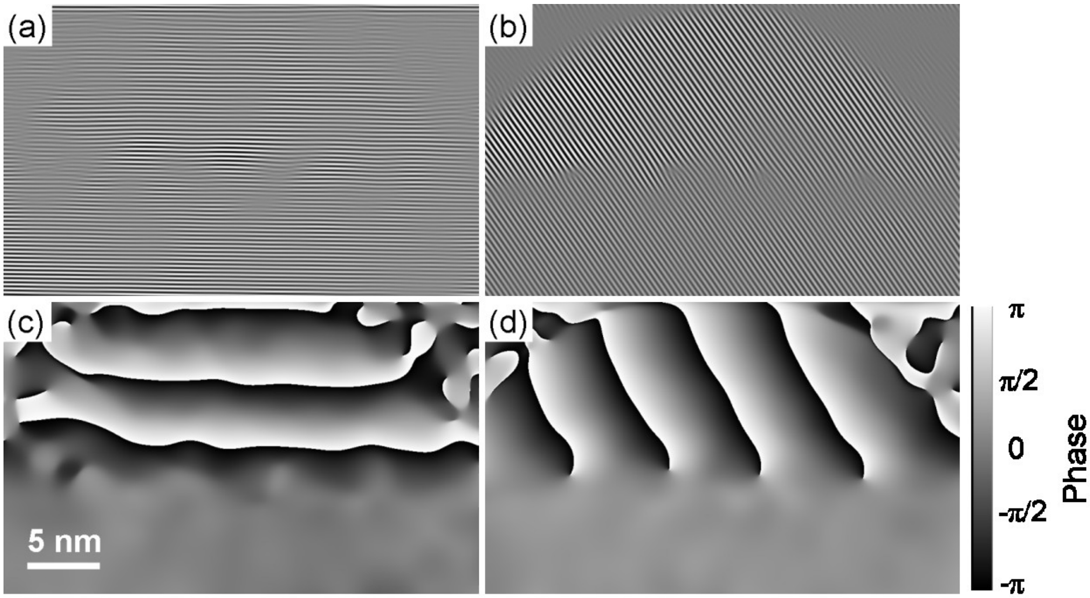

Figure A.2 Intensity of the (a) 002 and (b) $1\bar{1}1$ inverse FFTs of Supplemental Fig. 1(a). Phase images of the (a) 002 and (b) $1\bar{1}1$ inverse FFTs of Supplemental Fig. 1(a).

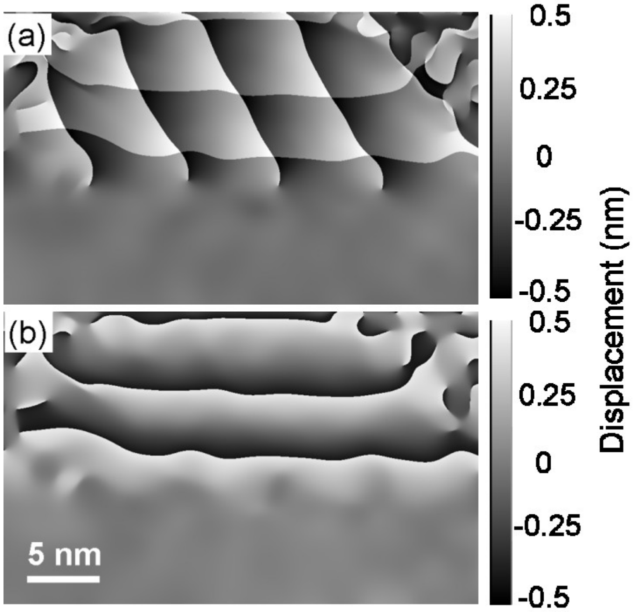

Figure A.3 (a) In-plane, $[1\bar{1}0]$, and (b) out-of-plane, [001], components of the displacement field computed from the linear combinations of the phase images shown in Supplemental Fig. 2(a) and (b), as described by Eqns. (A.4) and (A.5).

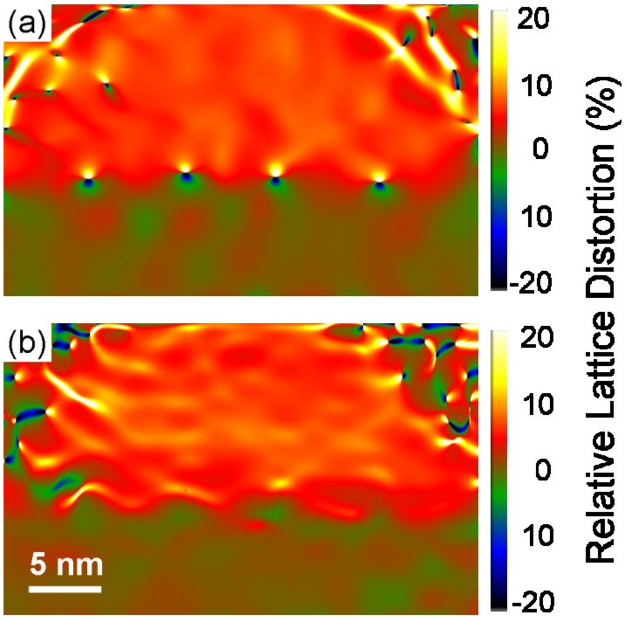

Figure A.4 (a) In-plane, [1$\bar{1}$0], and (b) out-of-plane, [001], lattice distortion maps obtained from GPA of Supplemental Fig. 1(a).

References

---

[1] M. J. Hytch, E. Snoeck, and R. Kilaas, Ultramicroscopy 74, 131-146 (1998).

Appendix B

Size Analysis of Quantum Dots

Here, we describe the procedures for the identification and size quantification of the MBE-grown metal islands and semiconductor QDs based on AFM and XSTM images. Scanning Probe Image Processor (SPIP) and Park Scientific Instruments' (PSI) Image Processing Software were used to perform the analyses. We also describe how the QD size distributions are determined using Origin software.

To quantify the QD size from AFM images, we used the Particle and Pore Analysis module in SPIP. In particular, AFM images consisting of 1024 × 1024 pixels were loaded in SPIP. The "Advanced Threshold" detection method was used for QD identification. Based on the root mean square (RMS) of the height values within the image, we defined a height threshold level by adding 5 × RMS to the substrate background level. Regions above the defined threshold level were identified as QDs. Finally, the QD sizes (i.e. diameters, heights, and etc.) were exported from SPIP in a spreadsheet.

To quantify the QD size from XSTM images, we used the Line Analysis tool of the PSI Image Processing Software. Detailed descriptions of the Line Analysis tool are included in Dr. B. Lita's Ph.D. Thesis.[1] To differentiate the GaAs and InAs QDs within the XSTM images, we estimated the tip height criterion as follows. Bright regions protruding at least 4.2 Å above the GaAs background were assessed as possible QDs. Within the bright regions, pixels with tip heights of at least 1.8 Å above the GaAs background were considered to be part of the QD.[2]

With the QD sizes obtained from AFM and XSTM images, we calculated the mean and standard deviation of the QD sizes and plotted the size distributions as described below. We first plotted the QD frequency (%) as a function of QD diameter (or height) and then fitted the histogram with a Gaussian distribution in Origin. The fitted QD size distributions from XSTM images are shown in Figure 3.2, while the size distributions from AFM images are shown in Figure 4.2, Figure 4.3, and Figure 4.4.

References

---

[1] B. Lita, Ph.D. Thesis, University of Michigan, 2001.

[2] V. D. Dasika, R.S. Goldman, J.D. Song, W.J. Choi, I.K. Han, J.I. Lee, J. Appl. Phys. **106**, 014315 (2009).

Appendix C

Determination of Arsenic Species Produced by As Cracking Cell

In this appendix, we describe the details regarding the method we used to determine the As species produced by the As cracker in our MBE system, as mentioned in Chapter 2. In particular, the As cracker is able to generate either As_4 or As_2, depending on the cracking zone temperature. Typically, As_4 and As_2 can be produced with a crack zone temperature of ~600 and ~1000˚C, respectively. However, an experimental method has not been developed to directly measure the As species produced by the As cracker. Therefore, the following method was used in this thesis study to identify the predominant As species produced by the As cracker. Figure C.1 shows a plot of As beam equivalent pressure (BEP) as a function of the cracking zone temperature. A graduate decrease in As BEP with increasing cracking zone temperature is apparent, consistent with the fact that As_4 can be ionized more easily than As_2. Furthermore, the As BEP begins to saturate at $\sim 7.0\times10^{-6}$ ($\sim 1.5\times10^{-5}$) torr at temperatures above 1000˚C (below 600˚C), suggesting that the As species is predominantly As_2 (As_4) for cracking zone temperatures above 1000˚C (below 600˚C). Although the predominant As species can be identified using the method described above, an accurate percentage of how much each As species is contained in the beam flux is however not achievable with this simple method.

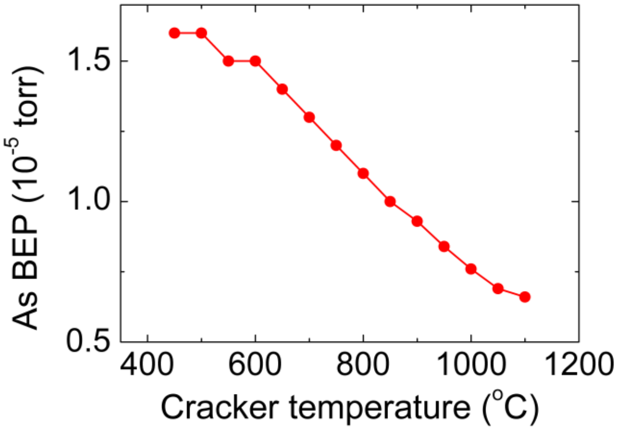

Figure C.1 A plot of the As beam equivalent pressure (BEP) as a function of As cracking zone temperature.

Appendix D

I-V Measurement of *p-i-n* Structures

As mentioned in Chapter 2, we examined the current-voltage (I-V) characteristic of the InAs SK QD cell and the GaAs control cell at various illumination intensities. Figure D.1 shows the short-circuit current densities (J_{SC}), open-circuit voltage (V_{OC}), fill factors (*FF*), and power conversion efficiencies (η) as a function of the logarithm of the solar illumination intensities. At all intensities, J_{SC} of the QD cell is similar to that of the control cell. On the other hand, at low illumination intensities, the V_{OC}, *FF* and η of the control cell are lower than that of the QD cell, presumably due to a larger leakage current of the control cell. As the illumination intensity increases, the J_{SC} and V_{OC} of both the QD and control cells increase monotonically. In addition, for the control cell, the *FF* and η increase with increasing illumination intensity, reaching saturation at ~100 mW/cm^2. However, for the QD cell, both *FF* and η decrease at high illumination intensity, which is likely due to a significant series resistance of the QD cell. For future work, the improvement of the solar cell metallization design is essential to minimize the series resistance for I-V measurements at high illumination intensities.

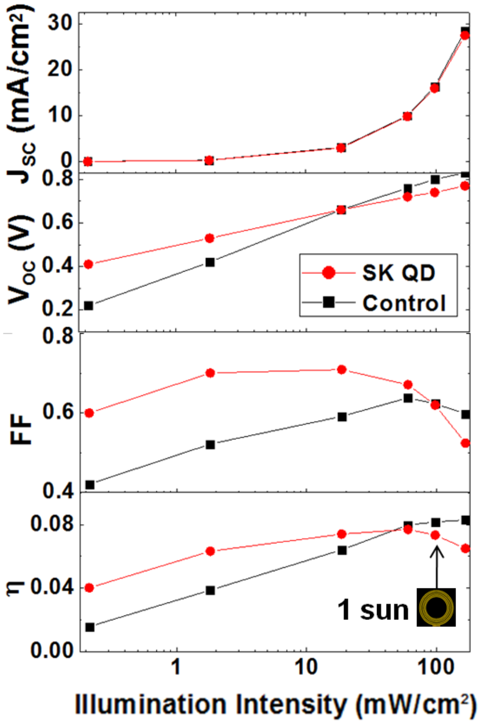

Figure D.1 The short-circuit current densities (J_{SC}), open-circuit voltage (V_{OC}), fill factors (FF), and power conversion efficiencies (η) as a function of the logarithm of the solar illumination intensities for both the InAs SK QD cell and the GaAs control cell.

Appendix E

Phase-Field Model of InAs Quantum Dot Nucleation

To simulate the evolution of the film structure, we use a phase-field model with three conserved order parameters[1] (simulation done by Larry Aagesen in Thornton group at University of Michigan). Order parameters, ϕ_1, ϕ_2, and ϕ_3, represent the vapor, InAs, and GaAs phases, respectively, and are constrained such that $\phi_1+\phi_2+\phi_3=1$ throughout the simulation domain. The order parameter ϕ_3 for the GaAs substrate is assumed to remain constant. Using the constraint of $\phi_1+\phi_2+\phi_3=1$ to eliminate ϕ_1, the system is evolved using a Cahn-Hilliard equation for ϕ_2 (InAs):

$$\frac{\partial\phi_2}{\partial t} = \nabla\cdot\left[M(\phi_1)\,\nabla\left(\frac{\delta F}{\delta\phi_2}\right)\right] + S \tag{1}$$

$$\frac{\delta F}{\delta\phi_2} = 2W_{12}\phi_1\phi_2(\phi_1-\phi_2) - 2W_{13}\phi_1\phi_3^2 + 2W_{23}\phi_2\phi_3^2 - \alpha_{12}^2\nabla^2\phi_2 + \frac{1}{2}\left[-\alpha_{12}^2\nabla^2\phi_3 + \alpha_{23}^2\nabla^2\phi_3 - \alpha_{13}^2\nabla^2\phi_3\right] + \frac{\partial f_{el}}{\partial\phi_2}$$

(2)

where the mobility function $M(\phi_1)=16M_s\phi_1^2(1-\phi_1)^2$ limits diffusion to the vapor/InAs interface, $S = dn_y\phi_1(1-\phi_1)$ is a source term that preserves the equilibrium solution of the order parameters at the interface, d is the deposition rate (perturbed with 10% random variation), n_y corrects for the orientation of the substrate relative to the InAs deposition incident from the $+y$ direction, and W_{ij} and α_{ij} are the potential barrier height and gradient energy coefficient, respectively, for an *i-j* interface. The elastic energy density f_{el} can be expressed as follows:

$$f_{el}=\frac{Z\alpha_{12}}{2}\sum_{i,j=1}^{2}\sigma_{ij}\left[\epsilon_{ij}-\eta\left(\phi_2\right)\delta_{ij}\right] \tag{3}$$

where δ_{ij} is the stress tensor, ϵ_{ij} is the strain tensor, $\eta\left(\phi_2\right)=3\phi_2^2-2\phi_2^3$ is the non-dimensionalized misfit strain of InAs relative to GaAs, δ_{ij} is the Kronecker delta function, and *Z* is a dimensionless measure of the relative strengths of the elastic and interfacial energies. The stress tensor is obtained by solving for mechanical equilibrium at each time step as below:

$$\nabla\cdot\sigma_{ij}=\nabla\cdot\left(\sum_{k,l=1}^{2}C_{ijkl}\left(\phi_1,\phi_2,\phi_3\right)[\epsilon_{\{kl\}}-\eta\left(\phi_2\right)\delta_{kl}]\right)=0 \tag{4}$$

where assume isotropic elasticity, and the stiffness coefficients are a function of the order parameters as follows:

$$C_{ijkl}(\phi_1,\phi_2,\phi_3) = C_{ijkl}^{(1)} + Q_1(\phi_2)(C_{ijkl}^{(2)}-C_{ijkl}^{(1)})+Q_1(\phi_3)(C_{ijkl}^{(3)}-C_{ijkl}^{(1)}) \tag{5}$$

$$Q_1(\phi) = 3\phi^2-2\phi^3 \tag{6}$$

The interfacial thickness δ_{ij} and interfacial energy γ_{ij} between phases *i* and *j* can be related to phase-field model parameters as below:

$$\delta_{ij}=\frac{\sqrt{2}\alpha_{ij}}{\sqrt{W_{ij}}} \tag{7}$$

$$\gamma_{ij}=\frac{\alpha_{ij}\sqrt{W_{ij}}}{3} \tag{8}$$

We choose $\delta_{12}=\delta_{13}=\delta_{23}$ and set W_{ij} and α_{ij} such that $\gamma_{12}=0.704\ J/m^2$, $\gamma_{13}=1.04\ J/m^2$, and $\gamma_{23}=0.1\ J/m^2$. The dimensionless parameter $Z=\frac{\eta_0^2\,C_{44}^{(2)}\,L\sqrt{2}}{12\,\gamma_{12}}=0.233$ sets the relative strength of the elastic and interfacial energies, where $\eta_0 = 7.166\%$ is the misfit strain between

InAs and GaAs,[2] $C_{44}^{(2)} = 39.6$ GPa is a reference elastic constant for ϕ_2 (InAs), and $L = 6.54$ nm is the characteristic length scale of the problem.[3] The vapor is treated as a highly compliant elastic solid in Equation 4. We chose non-dimensionalized values $M_s = 1$, $d = 2.5\times10^{-2}$. The simulation grid spacing, $\Delta x = 2.5\times10^{-2}$ (corresponding to physical dimension of 0.1635 nm) and time step, $\Delta t = 4\times10^{-3}$. With these parameters, wetting layer thickness of 1.6 monolayers was resolved in the phase-field model. Using 4096 grid points in the x-direction, we simulated 0.67 μm of the 1 μm line-cut from AFM image of GaAs buffer surfaces. Furthermore, the Cahn-Hilliard equation is solved using a Crank-Nicolson scheme in which the fourth-order evolution equation for ϕ_2 is split into two second-order equations for ϕ_2 and μ. The discretized equation for each time step is solved using a multi-grid method with Gauss-Seidel iterations. No-flux boundary conditions are imposed in both x and y directions. Mechanical equilibrium is also solved iteratively using a multi-grid method with Gauss-Seidel smoothing, with zero-displacement boundary conditions at the bottom, left and right sides of the computational domain, and a traction-free boundary condition at the top of the domain.

References

---

[1] D. J. Seol, S. Y. Hu, Z. K. Liu, L. Q. Chen, S. G. Kim, and K. H. Oh, J. Appl. Phys. **98**, 044910 (2005).

[2] K.-H. Hellwege, Landolt-Bornstein, *Semiconductors. Physics of Group IV Elements and III-V Compounds*. (Springer-Verlag GmbH, 1982).

[3] M. E. Thompson, C. S. Su, and P. W. Voorhees, Acta Metall. Mater. **42**, 2107 (1994).

Appendix F

Finite-element Schrödinger-Poisson Calculations of EQE of *p-i-n* Structures

To calculate the EQE enhancement due to the presence of the QDs, we use a finite-element solution of the Poisson (1) and Schrödinger (2) equations (calculation done by Andrey V. Semichaevsky in Johnson group at University of Illinois). The Schrödinger equation includes a confining potential that accounts for the influence of misfit strain V_0 and the electric potential Φ.

$$\nabla^2\Phi = -\frac{\rho}{\varepsilon_0\varepsilon} \tag{1}$$

$$-\frac{\hbar^2}{2m^*}\nabla^2\Psi + (e\Phi + V_0)\Psi = \Lambda\Psi \tag{2}$$

,

where ρ is the charge density, ε is the permittivity, V_0 is the confinement potential due to strain and composition, Ψ are the wave functions, Λ are the eigenstates, m^* is the carrier effective mass, and e is the electron charge. The Poisson equation, coupled to the diffusion equations for the electrons and holes, is first solved on the scale of the whole *p-i-n* structure, and thus, the position-dependent built-in potential can be determined. The value of the built-in electric field in the heterostructure region is found to be ~7.5×10^5 V/m. The charge density in (1) is calculated for the assumed dopant concentrations, *p-i-n* structure geometry, and carrier mobilities. The electric potential Φ, referenced to the bottom layer of the QD SL is used in eq. (2).

We consider In-Ga interdiffusion in the WLs based upon an analysis of XSTM data from Ref. 15. Thus, the position-dependent In concentration in the wetting layer, x_{In}, is approximated by a Gaussian profile, $x_{In}= 0.32\exp(-(z-z_{0i})^2/\sigma^2)$. z_{0i} corresponds to the middle of the *i-th* QD layer along the z- (growth) axis, and the standard deviation, σ, equals to 1.25 nm. We take the inhomogeneous In concentration into account via the linear combination of carrier effective masses, so that the effective mass of the alloy is position-dependent, $m^*(z)$ in equation (2), given by

$$m^*(z) = x_{In}(z)m^*_{In} + (1 - x_{In}(z))m^*_{Ga}, \tag{3}$$

where $x_{In}(z)$ is the In atomistic fraction in the WL. The mechanical strain field is found numerically using a finite-element continuum elasticity model. The lattice constants in the inhomogeneous WLs are then determined using Vegard's law, as follows:

$$a(z) = x_{In}(z)a_{In} + (1 - x_{In}(z))a_{Ga}, \tag{4}$$

The confining potential profile for the QD heterostructure is determined by adjusting the bulk bandgaps and electron affinities to account for the effects of strain. Strain fields in QDs are also calculated from a continuum elasticity model, with QD dimensions and WL In concentration gradients from XSTM data. Strain-modified band offsets are then determined using deformation potentials from the literature.[1] Since the InAs QDs are compressively strained, the valence (conduction) band-edge shifts down (up), leading to a substantial widening of the QD effective band gap.

Using the valence and (conduction) band wave functions Ψ_n (Ψ_k), and energy levels E_n (E_k), at photon momentum q=0, the optical absorption spectrum of a QD becomes:

$$\alpha_{QD}(\omega) = \frac{2}{\sqrt{2\pi\sigma}}\sqrt{\frac{\mu}{\varepsilon}}\frac{\hbar^2\pi}{V}(\frac{e}{m_0})^2 A^2 \int \sum_{n,k}\frac{\hbar}{E_k - E_n}\{|\int_V \Psi_k^*(0,\vec{r})(\frac{\partial}{\partial x}\Psi_n(0,\vec{r}))d^3\vec{r}\,|^2 +$$
$$|\int_V \Psi_k^*(0,\vec{r})(\frac{\partial}{\partial y}\Psi_n(0,\vec{r}))d^3\vec{r}\,|^2\}(f(E_n)\text{-}f(E_k))\exp\{\text{-}(E\text{-}\hbar\omega)^2)/2\sigma^2\}dE, \tag{5}$$

where μ and ε are material permeability and permittivity, respectively; n and k are the indices of the initial and final confined states, *f(E)* is the electronic occupancy given by the Fermi distribution, assuming that the Fermi level is in the middle of the bulk GaAs bandgap, σ is thermal broadening (0.026 eV at room temperature), V is the unit cell volume, and A=1 (1/3) for heavy (light) holes. The net effective absorption of a unit cell containing QDs is then determined using the volumetric average of the combined heavy and light hole absorption in the QDs and the absorption in the GaAs barrier.[2]

The absorption coefficients, refractive indices, carrier effective masses, and carrier diffusion lengths of GaAs are taken from literature reports,[3] and are listed in Appendix G. For the typical QD densities in our samples, the lateral spacing between QDs is on the order of 40-90 nm. Based on the solution of the Schrödinger equation, at such a large lateral separation between the dots, it is reasonable to assume that the overlap integrals between the wave functions of electrons in these dots are negligibly small, and the lateral coupling between QDs will not contribute significantly to the miniband broadening. The tunneling transmission coefficient between states in vertically stacked QDs for the confined electrons at the top of the potential well is

$T \approx 16\exp(-2a\sqrt{\frac{2m^{*}V_0}{\hbar^{\wedge}}}) < 10^{-4}$, where a is the spacing between the QDs in adjacent layers. The heterostructures that we consider in the calculations consist of QDs infinitely periodic in x and y, arranged in three period SLs along the z-(growth) axis.

The EQE of the device is calculated from the short-circuit photocurrent density at the *i-p* interface. Figure F.1 shows the *p-i-n* device structures of (a) GaAs control cell (b) InAs/GaAs QD cell, and (c) a schematic energy band diagram of the QD cell. The steady-state photogeneration-drift-diffusion equations,[3] as shown below, are solved for the electron current density on the *p*-side of the *i-p* interface, neglecting the dark current:

$$\frac{\partial n}{\partial t} = G_n - R_n + \frac{1}{q}\nabla\cdot\left(-q\mu_n n\nabla\varphi + qD_n\nabla n\right), \tag{6}$$

$$\frac{\partial p}{\partial t} = G_p - R_p + \frac{1}{q}\nabla\cdot\left(-q\mu_p p\nabla\varphi - qD_p\nabla p\right), \tag{7}$$

$$\nabla\cdot(\varepsilon\nabla\varphi) = -q\left(p - n + C_0\right), \tag{8}$$

where n and p are the electron and hole concentrations, D_n and D_p are the electron and hole diffusion coeifficients, φ is the electrostatic potential, μ_n and μ_p are the electron and hole mobilities. ε is the permittivity, q is the fundamental electron charge, G_n and G_p are the electron and hole photogeneration rates, and R_n and R_p are the electron and hole recombination rates. The photocurrent density is normalized to the incident solar photon flux $\Phi_{inc}(\lambda)$, according to:

$$EQE(\lambda) = \frac{1}{F_{inc}(\lambda)}\{\int_{-W_n}^{W_i} F(\lambda,z)\alpha(\lambda,z)dz + F(\lambda,W_i)\frac{\alpha(\lambda,W_i)L_n}{1+\alpha(\lambda,W_i)L_n}\}, \tag{9}$$

where L_n is the electron diffusion length in the *p*-region, $F(\lambda,z)$ is the photon flux traversing the plane at position z in the intrinsic region, $\alpha(\lambda,z)$ is the absorption coefficient of either the bulk or the QD-doped semiconductor, W_i and W_n are the thicknesses of the intrinsic and *n*-type layers, respectively, and $F_{inc}(\lambda)$ is the incident (solar) photon flux. The position $z=0$ corresponds to the position of the *n*-*i* interface. A transfer matrix approach is used to calculate the propagation of randomly-polarized solar illumination normally incident on the *p*-*i*-*n* structure.

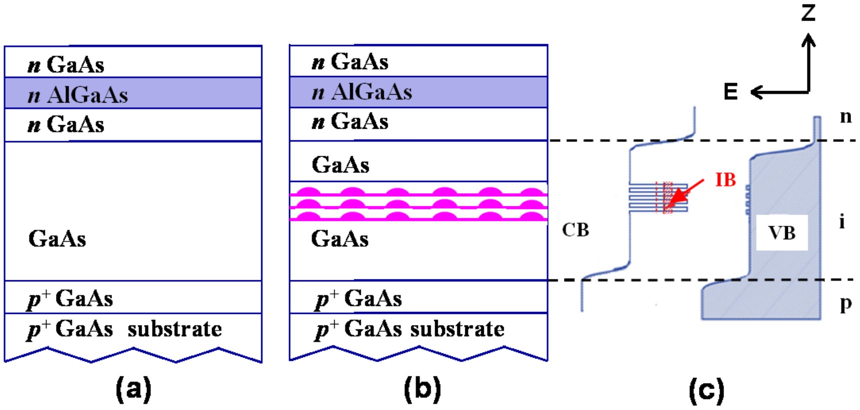

Figure F.1 *p-i-n* device structures of (a) GaAs control cell (b) InAs/GaAs QD cell, and (c) a schematic of energy band diagram of the QD cell.

References

---

[1] C.G.Van de Walle, Phys. Rev. B **39**, 1871 (1989).

[2] V. Aroutiounian, S. Petrosyan, A. Khachatryan, J. Appl. Phys. **89**, 2268 (2001).

[3] S.L. Chuang, *Physics of Photonic Devices* (Wiley, New York, 2009).

Appendix G

Materials Parameters

In this appendix, materials parameters used in the finite-element Schrödinger-Poisson calculations, phase field model, and elastic strain energy approximation are summarized in Table 2 and Table 3, respectively:

Table 2 Materials parameters[1] used in the finite-element Schrödinger-Poisson calculations described in Appendix F.

Parameter	GaAs	InAs
Absorption coefficient (cm^{-1})	10^4	N/A
Refractive index	3.4	N/A
Electron effective mass (m_0)	0.067	0.023
Heavy hole effective mass (m_0)	0.5	0.4
Light hole effective mass (m_0)	0.087	0.026
Electron diffusion coefficient (cm^2/s)	220	N/A
Hole diffusion coefficient (cm^2/s)	10	N/A

Table 3 Stiffness tensor components[2], surface energies[3,4], shear moduli,[5,6] and Poisson's ratios[5,6] used in the phase field model described in Appendix E and the elastic strain energy approximation in Chapter 5.[7]

Parameter		GaAs	InAs	$In_{0.2}Ga_{0.8}As$
Stiffness tensor component (GPa)	C_{11}	119	83.3	111.9
	C_{12}	53.8	45.3	52.1
	C_{44}	59.4	39.6	55.4
Surface energy (J/m^2)		1.04	0.704	0.97
Shear modulus (10^{10} N/m^2)		3.3	1.9	3.0
Poisson's ratio		0.31	0.35	0.32

Reference

---

[1] S.L. Chuang, *Physics of Photonic Devices* (Wiley, New York, 2009).

[2] K.-H. Hellwege, Landolt-Bornstein, *Semiconductors. Physics of Group IV Elements and III-V Compounds*. (Springer-Verlag GmbH, 1982).

[3] E. Pehlke, N. Moll, A. Kley, and M. Scheffler, Appl. Phys. A 65, 525 (1997).

[4] N. Moll, A. Kley, E. Pehlke, and M. Scheffler, Phys. Rev. B 54, 8844 (1996).

[5] Burenkov, Yu. A., Yu. M. Burdukov, S. Yu. Davidov, and S. P. Nikanorov, Sov. Phys. Solid State 15, 1175-1177 (1973).

[6] Burenkov, Yu. A., S. Yu. Davydov, and S. P. Nikanorov, Sov. Phys. Solid State 17, 1446-1447 (1975).

[7] The stiffness tensor components, surface energy, shear modulus, and Poisson's ratio of $In_{0.2}Ga_{0.8}As$ is obtained from linear interpolation of those of InAs and GaAs.